Clathrate I Compounds of Barium with Transition Metal, Silicon and Germanium Framework and Contributions to TaNiSi

by

Umut Aydemir

A Thesis Submitted to the
Graduate School of Sciences and Engineering
in Partial Fulfillment of the Requirements for
the Degree of
Master of Science
in
Materials Science and Engineering
Koç University

June 2006

Koç University

Graduate School of Sciences and Engineering

This is to certify that I have examined this copy of a master's thesis by

Umut Aydemir

and have found that it is complete and satisfactory in all respects,
and that any and all revisions required by the final
examining committee have been made.

Committee Members:

_____

Mehmet Suat Somer, Ph. D. (Advisor)

_____

A. Levent Demirel, Ph. D.

_____

Michael Baitinger, Ph. D.

Date: _____

Ailem ve Sinem için ...

ABSTRACT

Throughout recent years, clathrate compounds attracted significant attention due to their unique transport properties. These compounds are reported to have potential superconducting, thermoelectric, electro-optic, and super-hard materials applications. Among these applications high thermoelectric efficiency has been the most challenging property to be obtained. Since the thermoelectric efficiency of clathrates is still low, towards for an application the compounds and their exact compositions have to be investigated and optimized. Here, we report on investigations of type I clathrate compounds with the composition $Ba_8(T_x(Ge,Si)_y\square_z)(Ge,Si)_{40}$ (T = Ni, Pd, Pt; □ = defect; x+y+z = 6). The crystal structure and homogeneity phase range of Ni containing Ge clathrates were determined and physical properties were discussed in context with the Si clathrates and clathrates with other transition metals. Single crystals with different compositions were obtained, their structures and site occupancies were determined from single crystal X-ray analysis. Investigations of electrical-transport properties of compounds revealed a semiconductor–metal transition and a bad metallic behavior for Ge and Si clathrates, respectively. The case for Ge was justified also by theoretical calculations. No superconductivity was observed for temperatures down to 2 K. Magnetic susceptibility measurements showed a large diamagnetic response for all compounds. The low thermal conductivity observed for these compounds can be explained via strong scattering of phonons introduced by the dynamic rattling motion of the guest atoms inside the 24-atom polyhedra, deduced from the relatively high atomic displacement parameters obtained from low temperature single crystal X-ray analysis. TaNiSi compound has been found as a by product material during the preparation of Si clathrate compounds. In this work, a new low temperature route for the synthesis of TaNiSi was developed which enables the access to single phase materials and well-shaped single crystals. Crystal structure of the compound

has been determined using single crystal X-ray diffraction method. The physical properties have also been studied by resistivity, specific heat capacity and magnetic susceptibility measurements. The investigated compound behaves as Pauli paramagnet and shows bad metallic conductivity. Calculated Debye temperature (434 K) indicates relatively high stiffness of the compound. DTA analysis shows that it melts at 1852 °C which enables it as a candidate for high temperature processing. Additionally, a method of single-crystalline coating on metal wires was successfully developed.

Özet

Son zamanlarda kafes bileşikleri (clathrate compounds) etkin iletim özelliklerinden dolayı yoğun bir ilgi çekmekteler. Bu bileşikler süper iletkenlik, termoelektrik, elektro-optik ve süper sert madde olma nitelikleri göstermektedir. Bunlar arasında deneysel realizasyonu en zor olan termoelektrik verimlilik özelliğidir. Termoelektrik verimliliği istenilen düzeye getirebilmek için bu bileşiklerin kompozisyonları tam olarak belirlenmeli ve optimize edilmelidir. Bu tez araştırmasında I-tipte (type I) kafes bileşiklerinin "$Ba_8(T_x(Ge,Si)_y\square_z)(Ge,Si)_{40}$ (T = Ni, Pd, Pt; □ = boşluk; x+y+z = 6)" kompozisyonları incelendi. Nikel içeren germanyumlu kafes bileşiklerinin kristal yapıları ve homojen faz aralıkları araştırıldı; fiziksel özellikleri diğer geçiş elementleri ve silikon içeren bileşiklerle karşılaştırıldı. Farklı başlangıç kompozisyonlarıdan tek kristaller seçilip, bunların yapı ve gerçek kompozisyonları tek kristal X-ışını kırınımı analizi ile belirlendi. Bu malzemelerin elektrik iletkenliği üzerine yapılan incelemeler sonucunda germanyumlu bileşiklerin yarıiletken-metal geçiş özelliği, silikonlu bileşiğin ise metalik özellik gösterdiği anlaşıldı. Germanyumlu bileşikler üzerine yapılan teorik hesaplamalar bu bulguları doğrulamaktadır. Süper illetken özelliği ise 2 K' e inildiği halde hiç bir bileşikte gözlemlenmedi. Gene, yapılan ölçümler tüm bileşiklerin diyamanyetik özelliğe sahip olduğunu ortaya çıkardı. Bu bileşiklerde gözlemlenen düşük termal iletkenlik, Ba2 atomlarının 24-atomlu kafeslerin içerisinde yaptıkları titreşimler (rattling) sonucu ısı taşıyan fononların dağılmasıyla açıklanabilir. Ba2 atomlarının titreşim genliklerinin fazlalığı düşük sıcaklıklarda yapılan tek kristal X-ışını kırınımı analizi sonucunda belirgin bir şekilde görüldü. Silikon kafesli bileşikler sentezlenirken yan ürün olarak TaNiSi üçlü fazı bulundu. Buna paralel, tantal nikel silikon bileşiğinin düşük sıcaklıkta sentezini sağlayacak yeni bir yöntem geliştirildi ve başarı ile uygulandı. TaNiSi bileşiğin kristal yapısı tek kristal X-ışını kırınımı metodu ile belirlendi. Özdirenç, özgül ısı kapasitesi ve manyetik ölçümler yardımıyla TaNiSi' nin

fiziksel özellikleri saptandı. Yapılan ölçümler TaNiSi' nin kötü bir metal ve Pauli paramanyetik özelliği olduğunu ortaya çıkardı. Hesaplanan Debye sıcaklığı (434K) bu bileşiğin yüksek mekanik dayanıklılığa sahip olduğunu göstermektedir. DTA analizi ile bulunan 1852 °C lik ergime noktası, bu maddenin yüksek sıcaklık gerektiren uygulamalarda kullanılabileceğini gösterdi. Buna ek olarak metal tellerinin üzerine tek kristal kaplamaların yapılabileceği bir yöntem geliştirildi.

ACKNOWLEDGEMENTS

I would like to express my sincere appreciate to Prof. Mehmet Suat Somer for his invaluable supervision and constant support through my undergraduate and M.S. studies. Here, I would also like to thank both Prof. Yu. Grin and Dr. M. Baitinger for their continuous support, thoughtful guidance and providing me the opportunity to do part of my M.S. research at the laboratories of Max Planck Institute for Chemical Physics of Solids (MPI-CPfS) in Dresden, Germany.

I am grateful to all my professors and instructors at Koç University for the essential and important concepts they provided me through my stay at Koç, and Ms. D. Haciu for her help also in writing my M.S. thesis work.

Thanks are also to the people at MPI-CPfS who have helped me towards the completion of my M.S thesis work. I would like to thank Dr. H. Borrmann, Dr. R. Cordoso, Dr. Y. Prots and Mr. S. Hückmann for providing me X-ray diffraction measurements and many fruitful discussions about crystallography. Thanks to Dr. U. Burkhardt, and Ms. K. Schultze for their help in EDXRF and WDXRF measurements and interpretation of them. Thanks to Dr. W. Schnelle and Mr. R. Koban for the physical property measurements. Thanks to Dr. R. Niewa and Ms. S. Müller for their help in thermal analyses. I am very grateful to Dr. A. Örmeci and Dr. S. Leoni for the theoretical calculations and discussions on them.

My sincere thanks to the administration department at MPI-CPfS especially to Mrs. K. Demian and Mrs. C. Strochbach for making my stay comfortable and helping me in all matters I need. Also thanks to I. Wanschura for providing me many references for my M.S. thesis work.

As my friends, many thanks go to Ahmets, Hüseyin, Yavuz, Ümits, Turgut, rest of the colleagues in the MASE program, and undergraduate students in the Department of Chemistry for making those long years as enjoyable as they were.

I also want to thank my parents and sisters for their unconditional support and encouragement to pursue my studies. Without their persistent confidence and understanding I would never have completed my present work.

I am very grateful to Sinem for the inspiration she provided me throughout the times we spent together.

Finally, I would like to thank all whose direct and indirect support helped me completing my thesis in time as well as expressing my apology that I could not mention personally one by one.

TABLE OF CONTENTS

LIST OF TABLES

LIST OF FIGURES

NOMENCLATURE

B	:	Magnetic induction
c	:	Speed of light
C	:	Curie constant
C	:	Curie-Weiss constant
C_p	:	Specific heat capacity at constant pressure
C_v	:	Heat capacity at constant volume
E_F	:	Fermi energy level
E_g	:	Band gap energy
f	:	Frequency of vibration
|Fc|	:	Calculated structure amplitude
$\|F_0\|$	:	Observed structure amplitude
h	:	Planck constant
H	:	External magnetic field
J_Q	:	Thermal flux
K	:	Thermal conductivity coefficient
k_B	:	Boltzmann constant
l	:	Mean free path
L	:	Distance between two points
m	:	Magnetic moment per atom
m	:	Mass of atoms
m_e	:	Mass of electron
M	:	Magnetization
M_s	:	Saturation magnetization
M_s	:	Spontaneous magnetization

n	:	Number of reflections
$N(E_F)$	:	Density of states at Fermi energy level.
N	:	Number of atoms per formula unit
N	:	Total number of conduction electrons per unit volume
N_0	:	Avagadro's number
N_V	:	Number of atoms per unit volume
p	:	Total number of parameters refined
P_{eff}	:	Effective magnetic moment
R_m	:	Resistance of material
R	:	Residual or agreement index
S	:	Seebeck coefficient
T_c	:	Critical temperature for superconductivity
U_{eq}	:	Isotropic mean-square displacement parameter
ν	:	Average particle velocity
V	:	Electron-excitation coupling strength.
v_s	:	Velocity of sound
ω	:	Oscillation frequency
Z	:	The number of electrons
Z	:	Number of formula units
λ	:	Coupling constant.
β	:	Phononic term
σ	:	Electrical conductivity
κ	:	Thermal conductivity
ρ	:	Resistivity
ρ_0	:	Constant pre factor
ρ_r	:	Residual resistivity

θ_D	:	Debye temperature
θ_E	:	Einstein temperature
γ	:	Electronic Sommerfeld term
κ_L	:	Lattice thermal conductivity
κ_e	:	Electronic thermal conductivity
μ	:	Magnetic permeability
μ_0	:	Permeability of free space
μ_r	:	Relative permeability of material
θ	:	Critical temperature for magnetic materials
χ	:	Magnetic susceptibility
χ_0	:	Temperature independent magnetic susceptibility

Chapter 1

INTRODUCTION

1.1 Overview on Clathrates

According to the Encyclopedia Britannica, the word clathrate originates from a latin word ‘clathratus’ meaning that a compound formed by the inclusion of molecules of one kind in the cavities of the crystal lattice of another. With this general definition, a variety of compounds can be considered as clathrates such as skutterudites, zeolites, borides and so on.

The history of clathrates dates back to the discovery of gas hydrates with chlorine molecules by Davy in 1811 [1]. In 1823, Faraday proposed the formula of this gas hydrate as $Cl_2(H_2O)_{10}$ [2]. However, the correct structure was first determined in 1947 by Von Stackelberg et al. as $(Cl_2)_8(H_2O)_{46}$ [3]. There are mainly two types of ice clathrates with general formulas $M_8(H_2O)_{46}$ and $M_{24}(H_2O)_{46}$ referred to as type I and Type II clathrates, respectively. Here, M stands for the guest atom or molecule which can be a noble gas, a halogen molecule, etc.

Almost a decade later, in 1965, Cross and coworkers reported the existence of the first clathrate compounds of Si with the following compositions Na_8Si_{46} and Na_xSi_{136}, synthesized by controlled thermal decomposition of the Zintl phase NaSi [4, 5]. The latter compound was reported to be a nonstoichiometric phase with metal content varying between 3 and 11 [6]. The discovery of the silicon clathrates stimulated more interest in

compounds of other group 14 elements (C, Ge, Sn, and Pb) by modifying the guest atoms. Efforts in this direction resulted in the discovery of the first germanium and tin clathrates of type I, K_8Ge_{46} and K_8Sn_{46}, synthesized by direct fusion from pure elements [7]. Following the above discovery, experimental and theoretical works have been done to investigate the clathrates of group 14 elements (E14) with alkali metals, alkaline earth metals and rare earth metals. Among the mentioned clathrates, nine different structure types exist. The main difference between these structure types are that there are large asymmetric cavities between the building polyhedra and the threefold bonded cage species may be present [8]. Today, more than 50 phases with different structures are known in which type I structure is by far the most common structure among these phases. Our investigations are mainly focused on the type-I clahrates with the di-valent cation Ba which could be replaced by rare-earth elements. Table 1.1 gives a list of all the clathrates with di-valent cations that have been reported in literature.

Table 1.1 Table of known clathrates with divalent cations and corresponding references.

Compound	Structure type	References
Ba_6Ge_{25}	IX	[9-11]
Ba_6Si_{25}	VIII	[12]
$Sr_8Ga_{16}Ge_{30}$	I	[13-18]
$Sr_4Eu_4Ga_{16}Ge_{30}$	I	[19]
$Sr_8Al_{16}Si_{30}$	I	[15]
$Sr_8Ga_{16}Si_{30}$	I	[15]
α-$Eu_8Ga_{16}Ge_{30}$,	VIII	[20]
β-$Eu_8Ga_{16}Ge_{30}$	I	[20], [14], [19]
$Eu_2Ba_6Al_8Si_{36}$	I	[21]
$Ba_8Ga_{16}Ge_{30}$	I	[13], [15], [17], [22-24]
$Ba_8Ga_{16}Sn_{30}$	VIII	[15], [17], [25]
$Ba_8Al_{16}Ge_{30}$	I	[15], [21]
$Ba_8Al_{16}Si_{30}$	I	[15]
$Ba_8Ga_{16}Si_{30}$	I	[15], [17], [21], [26-27]
$Ba_8Cu_{16}P_{30}$	I	[28-29]
$Ba_8In_{16}Ge_{30}$	I	[21-30]
$Ba_8Cd_8Ge_{38}$	I	[28-30]
$Ba_8Zn_8Ge_{38}$	I	[27], [31]
$Ba_8Ag_6Si_{40}$	I	[31-32]
$Ba_8Au_6Ge_{40}$	I	[31-32]
$Ba_8Au_6Si_{40}$	I	[21], [31]
$Ba_8Cu_6Si_{40}$	I	[32]
Ba_8Si_{46}	I	[33]
Ba_8Ge_{43}	I	[34]
$Ba_8Mn_2Ge_{44}$	I	[35]
$Ba_8(T,Ge)_6Ge_{40}$	I	[31]
$Ba_8(T,Si)_6Si_{40}$	I	[31]
$Ba_8Au_6Ge_{20}Si_2$	I	[32]
$Eu_2Ba_6Cu_4Si_{42}$	I	[21]
$Ba_{16}Ga_{32}Sn_{104}$	II	[36]

The prototypes of the clathrate-I structure are the gas hydrates with stoichiometry $G_8(H_2O)_{46}$, where G = Ar, Kr, Xe, H_2S, Cl_2, CH_4, etc [6] (Figure 1.1(a)). Type-I clathrate compounds crystallize in a simple cubic lattice with space group $Pm\bar{3}n$ (No. 223). The 46 cage atoms (oxygens in water case) are all tetrahedrally coordinated and they arrange in the unit cell in two polyhedra of different sizes with 20-atom pentagonal dodecahedron and 24-atom tetrakaidecahedron (Figure 1.1(b)). The guest atoms or molecules are encapsulated in the cages if their sizes are comparable with the available space in the cages.

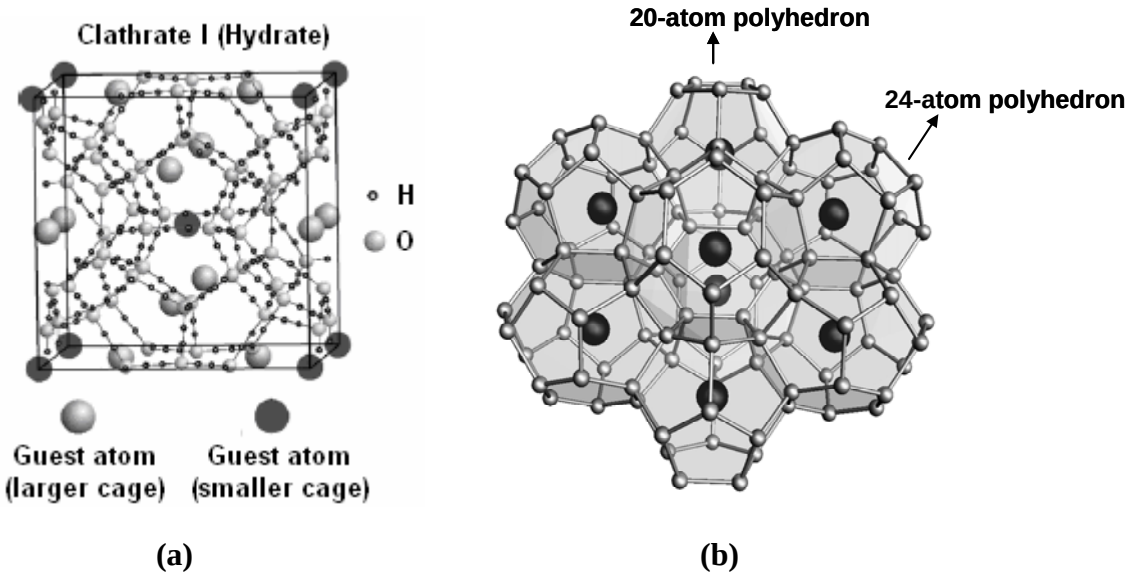

Figure 1.1 a) Type-I hydrate ($Xe_8(H_2O)_{46}$ structure [37], **b)** Polyhedral representation of the clathrate-I unit cell.

There are eight cages per formula unit. While guest atoms or molecules are in Wyckhoff 2a and 6d sites, atoms forming the cage structure are located in 6c, 16i and 24k sites. The 6c position bridging the pentagonal dodecahedra has special importance in the structure because E14 atoms at this sites were found to have defects and can readily be replaced by transition metals such as Mn, Zn, Fe, Ni, Pd, Pt, Cu, Ag and Au [31, 32, 35,

38-41]. Vacancies in some type-I clathrate compounds like K_8Ge_{44} [42], Rb_8Sn_{44} [43] and Cs_8Sn_{44} [44] are reported to occupy this site randomly and those in Ba_8Ge_{43} [34] make an ordered arrangement. Cordier and Woll already synthesized Ge and Si clathrates with Ni, Pd and Pt but neither precise crystal structure data nor metallographic and physical property measurements were reported in their article [31].

The formal electronic structure of clathrate compounds can be explained by the Zintl-Klemm-Busmann concept in which guest atoms in the cages behave as electron donors, transferring their valence electrons to the more electronegative host atoms forming weekly ionic bond to the cage framework. On the other hand, each atom in the cage is covalently bonded to four other atoms and completes their valence requirement with the electrons gained from the guest atoms. Hence, the clathrate-I phase with ideal stoichiometry 8:46 should be a conductor because of the eight or sixteen extra electrons per formula unit transferred from the mono-valent or di-valent cations, respectively. However, property measurements suggest that the clathrate-I phases can be diamagnetic and semiconducting instead of metallic [6]. The explanation for these observed properties is based on the vacancies found in the structure. For example, a missing cage atom can cause an incomplete valence shell for the four neighboring atoms. In this case, extra electrons transferred from the guest atom are used to complete their octet configuration. If all valence electrons are used in covalent bonds, the compound is expected to exhibit semiconducting behaviour.

Physical properties of clathrate compounds are strongly dependent on the structural features. Hence, composition is very important for physical properties and for materials optimization. For example, the conductivity for Si_{46} clathrates varies from semiconducting to metallic behavior depending on the composition [45]. In addition, vacancies in the structure can alter from an n-type conductor to a p-type conductor and thus change the thermoelectric properties [16, 22, 46]. The electron counting for these materials can be

adjusted via controlling the concentration of the electron donor like large barium atoms within the cages with that of the electron acceptor atoms substituted for E14 atoms in the cage framework. Different types of transition and rare-earth elements are used as dopands to control and manipulate the physical properties [47-50] .

During the last decade, clathrates attracted significant attention because of the discovery of novel physical properties and potential applications in these compounds. One highlight is the Ba-doped type I silicon clathrates $(Ba,Na)_xSi_{46}$ and Ba_8Si_{46} which exhibit superconducting properties, the former being the first clathrate superconductor ever obtained in bulk phase with a T_c of ≈ 4 K [51]. Utilizing a high pressure technique, Yamanaka et al. successfully synthesized the latter compound possessing $T_c \approx 8$ K [33]. Superconductivity observed for these clathrates is based on the degree of the hybridization of Ba 5d and Si 3p states. Consequently, T_c in superconducting phases decreases or increases as a result of the degree of hybridization [33, 52-55]. Theoretical band structure calculations revealed high density of states (DOS) at the Fermi level (E_F) for these compounds [52]. It is known that T_c is a function of DOS at E_F in normal state $N(E_F)$ through the coupling constant,

$$\lambda = N(E_F)V \qquad (1.1)$$

where V is electron-excitation coupling strength [47]. It is considered that superconductivity is an intrinsic property of the standard silicon sp^3 environment provided that efficient doping could be achieved [50].

Clathrates are also expected to be potential thermoelectric materials. Thermoelectric solids are promising materials due to their use in energy saving, like recovering heat for electricity production and for advanced refrigeration devices. Slack et al. discussed in detail the optimized conditions for obtaining good thermoelectric materials. The discussion led to

the concept of phonon - glass - electron- crystal (PGEC) materials [56]. In this approach, the best thermoelectric material would be 'engineered' to have thermal properties similar to those of an amorphous material, 'a phonon-glass', and electronic properties similar to that of an ordered, highly covalent single crystal, 'an electron single crystal' [57]. So, they suggest selecting solids having structures with large and weakly bounded ions that can 'rattle' inside oversized cages of the host network independently of its own phonon modes. The efficiency of a thermoelectric material is determined with respect to its value of dimensionless figure of merit ZT defined as,

$$ZT = \frac{S^2 \sigma T}{\kappa} \tag{1.2}$$

where S, σ and κ are standing for the Seebeck coefficient, electrical conductivity and thermal conductivity, respectively [58]. The rattling motion of guest atoms in cages of clathrate structure lowers the lattice thermal conductivity via scattering the heat-carrying phonons. Although thermal conductivity decreases, electrical conductivity remains relatively high since electronic conduction occurs through the sp^3 hybridized cage framework. Consequently, they have relatively high dimensionless figure of merit ZT [59]. Among different types of clathrate compounds, type-I clathrates have been considered as promising thermoelectric materials [15, 17, 24, 60, 61].

The relatively small and indirect energy gap in pure silicon with diamond structure makes it inappropriate for any application as an optoelectronic device. Recently, calculations demonstrated that the Si and Ge clathrates without any guest atom have larger band gaps than corresponding diamond structures [62]. These calculations indicate that Si and Ge clathrate compounds having low binding energies and large band gaps are candidates for optical applications.

In addition, the X-ray powder diffraction investigation with a synchrotron source revealed that the empty structure of Si_{46} preserves its stability up to 11 GPa [63]. The bulk modulus of the same compound was found to be 90 GPa that is only 8% smaller than that of the diamond phase of Si. Intercalating Ba and iodine in Si_{46} prevents a collapse of the cage structure up until 35 GPa [64]. So, clathrates may be considered as potential superhard materials.

1.2 Overview on Tantalum Nickel Silicide

The compound TaNiSi belongs to the TiNiSi structure type, which members are often entitled as "E-Phases" composed of two different transition metals T and T', and Si or Ge as the third component [65]. T is usually a transition element with relatively large atomic size (Ti, Zr, Ta, W, etc.) while T' represents a transition metal from the groups E8-E10 (Fe, Co, Ni, Cu, etc.). The TiNiSi type is a special branch of the $PbCl_2$ (or Co_2P) structure type, which contains several hundred phases and a variety of members of completely different character like Co_2Si, Ba_2Ge, TiNiSi, PbFCl and $PbCl_2$. The structure of these compounds is characterized by the a / c ratio in relation to the short b-axis. Jeitschko suggested a structure field diagram, in which all $PbCl_2$-types are plotted according to their a / c and (a + c) / b ratios (Figure 1.2) [66]. In this diagram, different types of the $PbCl_2$ families are divided in several branches. Within each branch, the structure and the coordination of the atoms of the compounds are similar.

Figure 1.2 Grouping of $PbCl_2$ type compounds according to Jeitschko.

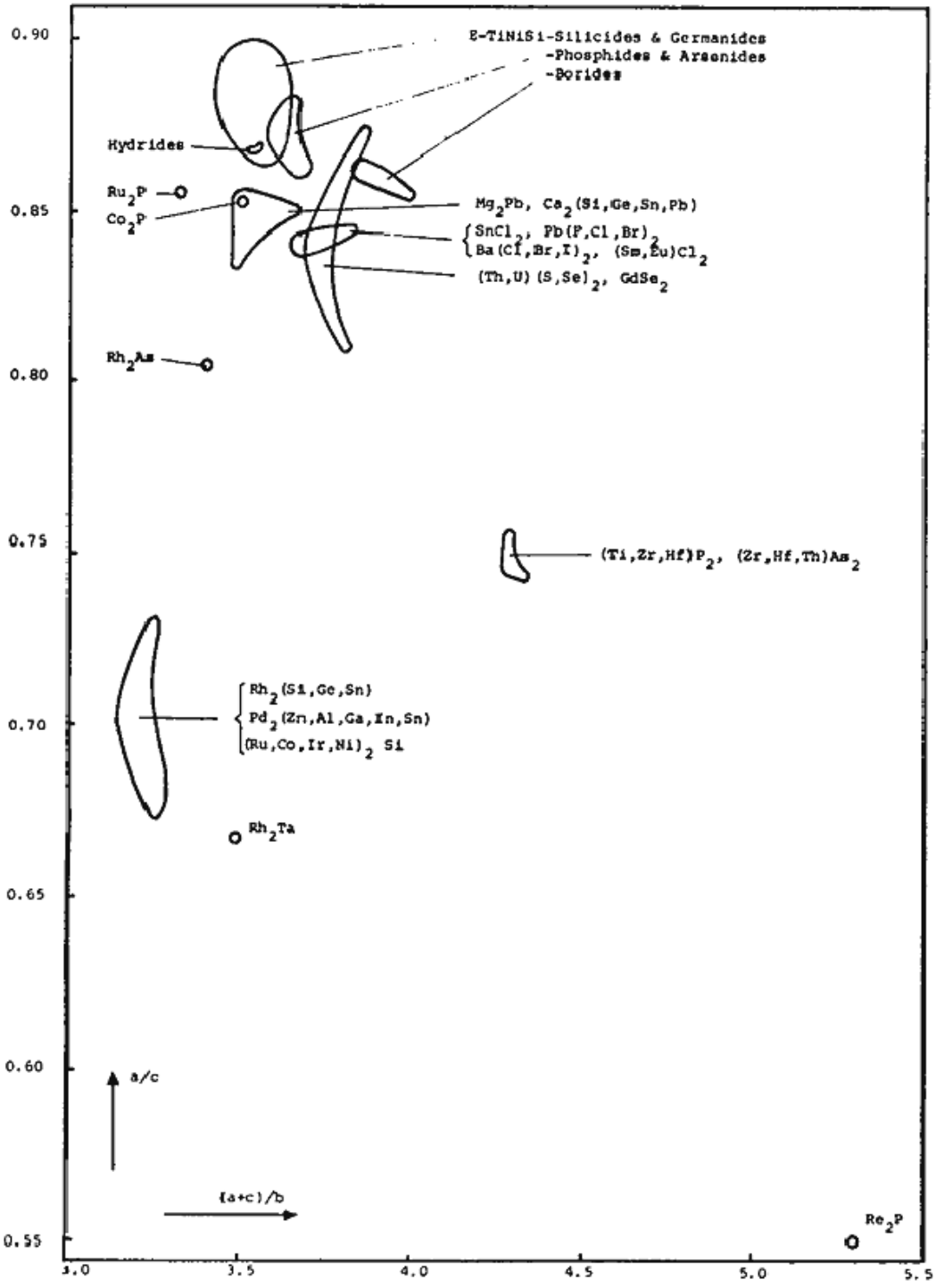

The ternary compound TaNiSi with composition 1 : 1 : 1 was already mentioned by Jeitschko et al., who made also the fundamental work to classify the different branches of the $PbCl_2$ type compounds [65]. The existence of TaNiSi was proved by comparison of the X-ray powder patterns with isotopic compounds, from which also the lattice parameters were refined. The synthesis of mono-phase TaNiSi and the related E phases has not been reported yet. This kind of high temperature materials are usually synthesized using a light arc furnace which is hardly suitable for preparation of the single phase compounds such as TaNiSi, since it does not represent the compound with the highest melting point in the ternary Ta/Ni/Si system.

Chapter 2

EXPERIMENTAL METHODS AND THEORETICAL CONCEPTS

2.1 Introductory Remarks

Due to the high purity and exact composition required, especially for the clathrate samples, any oxygen or moisture contact or contamination had to be minimized. Therefore, all sample manipulations, storage and syntheses were carried out in an argon filled glove box. Furthermore, all containers, preparatory apparatus, etc, were dried in a heating cabinet at 343 K for several hours, prior to transferring into the box. The conditions in the dry box were controlled by monitoring the oxygen and water level in parts per million with the minimum threshold set at less than 1 ppm for O_2 and H_2O.

2.2 Materials and Chemicals Used, Sources, and Quality

All educts were highly pure chemicals purchased from ChemPur. For the preparation of clathrates, Ba has been used in the dendritic solid form that was then cut into smaller pieces inside the glove box prior to use. Ge and Si lumps were finely powdered down to sizes around 80 μm using a tungsten carbide mortar. Pd and Pt were used as granules, Ni as foil and then cut into the required pieces. For the preparation of TaNiSi, a piece of tube and wire of Ta has been used of 8 mm and 0.8 mm diameter, respectively. For the coatings of

the Ta wires, 0.8 mm in diameter wires were used. Table 2.1 gives an overview of the chemicals utilized in the thesis, including the sources and purity grades.

Table 2.1 Elements [67] used, their sources and certified purities[68].

Elements	**Atomic Weight**	**Melting Points (° C)**	**Physical State**	**Company**	**Quality Description (%)**
Barium (Ba)	137.327	725	Crystalline dendritic solid	ChemPur	99.9
Nickel (Ni)	58.693	1453	Metal basis foil	ChemPur	99.9
Germanium (Ge)	72.61	937.4	Pieces	ChemPur	99.9999
Silicone (Si)	28.0855	1410	Pieces	ChemPur	99.999
Palladium (Pd)	106.42	1554	Granule	ChemPur	99.99
Platinum (Pt)	195.08	1772	Granule	ChemPur	99.99
Tantalum (Ta)	180.948	2996	Dark gray Ampoule (8mm ϕ) Wire (0.8mm ϕ)	Plansee ChemPur	99.9 99.9

2.3 Experimental Methods

2.3.1 Glove Box

The present research project required a consistent and reliable inert atmosphere that can provide proper results. In our laboratories, MBRAUN glove boxes are used (Figure 2.1). Standard MBRAUN inert gas systems are operated in accordance with the principle of gas circulation. The inert gas (Ar) continuously circulates between the glove box(es) and the gas purification system(s). Standard values reported for both oxygen and moisture are < 1 ppm. To achieve that purity, the box (es) are vacuum-tighted to evacuate the system and reduce the box pressure [69]. To have a better understanding, it might be helpful to know that in free air at 283K, the concentration of oxygen and moisture are 209000 and 12100 ppm, respectively.

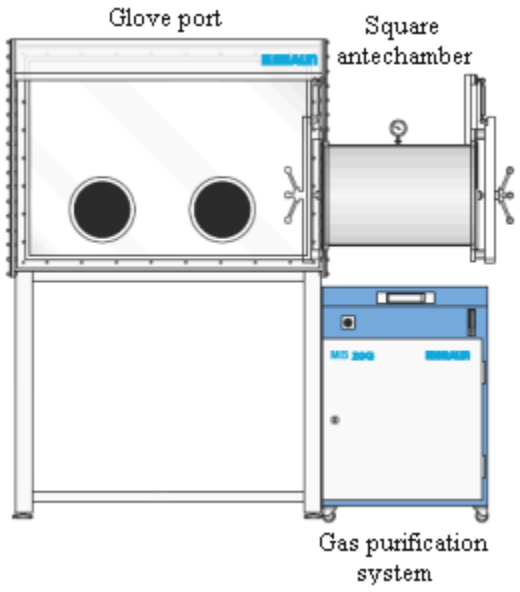

Figure 2.1 Glove box components [69].

2.3.2 High Frequency Furnace

The high frequency furnace (HF) was used in clathrate synthesis for melting the reactants sealed in Ta ampoules, as well as for coating of Ta wires with NiSi. The greatest advantage of an induction furnace is the targeted zonal heating of the samples. Unlike other heating methods, almost no energy is lost to the environment since high temperatures can be achieved very quickly and directly within the material itself. Induction heating is based on a simple well-known physical principle. When a high frequency electromagnetic field is applied to an electrically conductive material, a current is "induced" on its surface, which in turn produces heat based on Joule effect (or $R\ I^2$ losses).

HF used was TIG 5/300 from Hüttinger company, having a girth-diameter of the copper coil of 40 mm, 6 spiral turns and a height of 30 mm [70]. To obtain a homogeneous temperature distribution under an inert atmosphere, the furnace was integrated inside the glove box providing optimal reaction conditions. The *in-situ* temperature measurement was accomplished at the ampoule surface via using an IR pyrometer from the company Dr. George Maurer GmbH Optoelectronik with a detectable temperature range between 973 and 1873 K. In this arrangement, the pyrometer was placed at an optimal measuring distance pointing out to the ampoule surface. The apparatuses for HF setup and a sealed Ta ampoule can be seen in Figure 2.2.

(a)

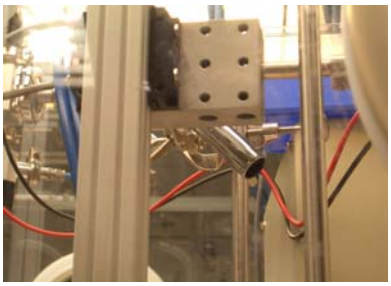

(b)

(c)

(d)

Figure 2.2 (a): HF, (b): IR pyrometer, (c): temperature displayer, (d): A sealed Ta ampoule for melting of starting materials for clahrate synthesis.

2.3.3 Arc Melting

Arc melting furnace was used for sealing of Ta ampoules as well as for the synthesis of binary NiSi (required for TaNiSi synthesis and wire coatings). The arc melting furnace (company: Centorr vacuum industries 5SA/38042-A, [71]) was placed inside the glove box together with the cooling system, copper hearts of various sizes and tungsten electrodes (Figure 2.3). The furnace chamber can be evacuated and filled with argon gas while operating. The operating temperature may exceed 3773 K.

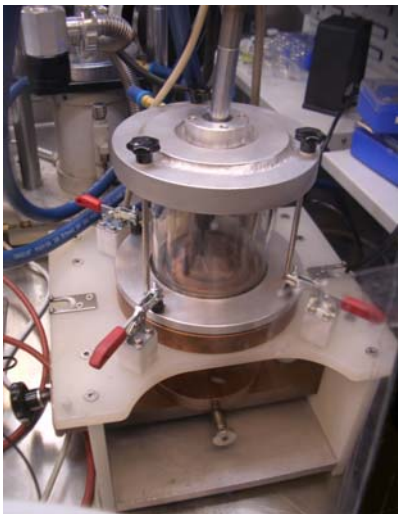

Figure 2.3 Arc furnace in glovebox.

2.4 Materials Characterization Techniques

2.4.1 X-ray Diffraction Techniques

2.4.1.1 X-ray Powder Diffraction Technique

2.4.1.1.1 Theory

X-ray diffraction geometry is based on Bragg equation given as:

$$2d_{hkl}\sin\theta=n\lambda \qquad (2.1)$$

where d refers to interplanar spacing , hkl's are called as Miller indices specifying plane orientation with respect to the unit cell edges, θ is the incident / scattering angle or called as

Bragg angle, n is the order of diffraction and the λ is the wavelength of X-ray beam (Figure 2.4).

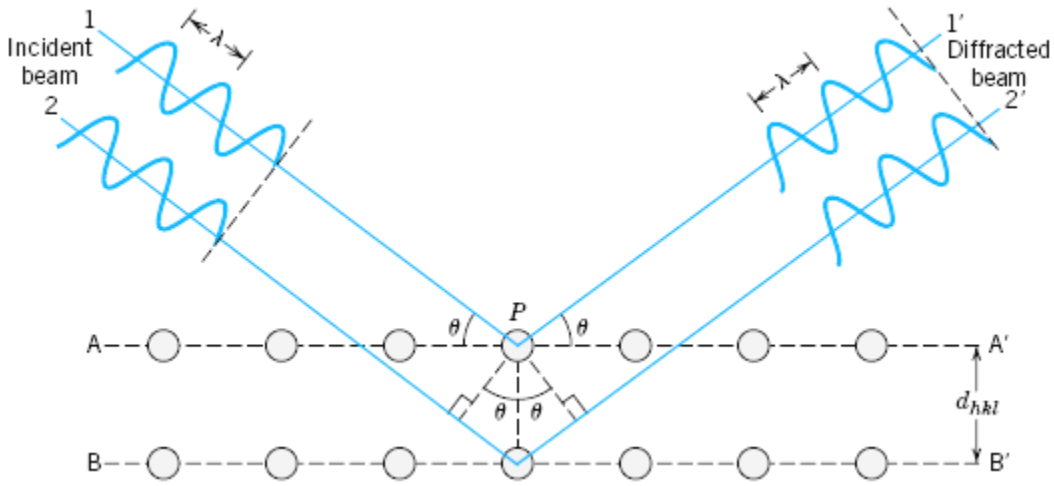

Figure 2.4 The Bragg construction for diffraction of X-rays on lattice planes [72].

According to equation (2.1), a single crystal gives a diffraction pattern with discrete diffraction beams, each in a definite direction relative to the orientation of the crystal and the incident beam [73]. Since the diffraction conditions are severe, a stationary single crystal gives very few reflections. Therefore, to generate the complete diffraction pattern, it is necessary to rotate the crystal in the X-ray beam. If several crystals from the same sample are exposed to X-rays, each of them gives its own diffraction pattern which will then superimpose. Assuming that the crystals have equal sizes and undergo a rotation, any particular reflection generated by each of the individual crystals is expected to satisfy the Bragg equation. Here, the direction of the diffracted beam varies while always being inclined at 2θ to the straight through direction. On a flat detector perpendicular to the incident beam, and on the opposite side of the sample, these sets of corresponding reflections from the multiple crystals appear as identical spots on a circle [73]. Since a

microcrystalline powder consist of infinite number of tiny crystals, this result in a complete circle for a particular reflection. Nowadays, diffraction patterns are measured by electronic detectors placed in powder diffractometers. In this measurement, intensity is measured as a function of angle and so a Bragg angle and intensity is obtained for each reflection. In this way, the full 3D diffraction pattern is transferred to 1D pattern with only geometrical variable as θ by using microcrystalline powder instead of single crystals[73].

The complete powder diffraction profile can be described in terms of four components. The first one is the peak positions which depend on the unit-cell dimensions. The second one is the peak intensities depending on the positions of atoms in the unit cell, and also atomic-displacement parameters. The third component is peak shapes and peak widths which may be described using 2θ-dependent analytical functions. The most common peak shape for X-ray powder diffraction is the pseudo-Voigt function which represents a hybrid of Gaussian and Lorentzian character [74]. The last component is the background intensity distribution which can be produced from a number of sources like fluorescent radiation emitted by the specimen, diffraction of a continuous spectrum of wavelengths, diffraction scattering from materials other than the specimen including soller slits, specimen binder, sample mount and air [75].

X-ray powder patterns are extensively used as one of the primary tools for determination of the educts and reaction products and also to assign the purity of the product formed. This characterization can be done via comparing experimentally obtained powder patterns with the ones in databases like Inorganic Crystal Structure Database (ICSD), Cambridge Structural Database (CSD), Protein Data Bank (PDB) ,etc. or with a theoretically simulated powder patterns from the single crystal structure data of the compound [76].

Another main area of application of powder diffraction is the structural characterization of microcrystalline materials that are unsuitable for investigation by single-crystal

diffraction techniques due to crystal twinning, other types of defects, lack of appropriate size and quality, etc. [75]. Accurate lattice parameters and structure determination of a crystalline sample can be done by powder XRD experiments with using an internal standard (Figure 2.5).

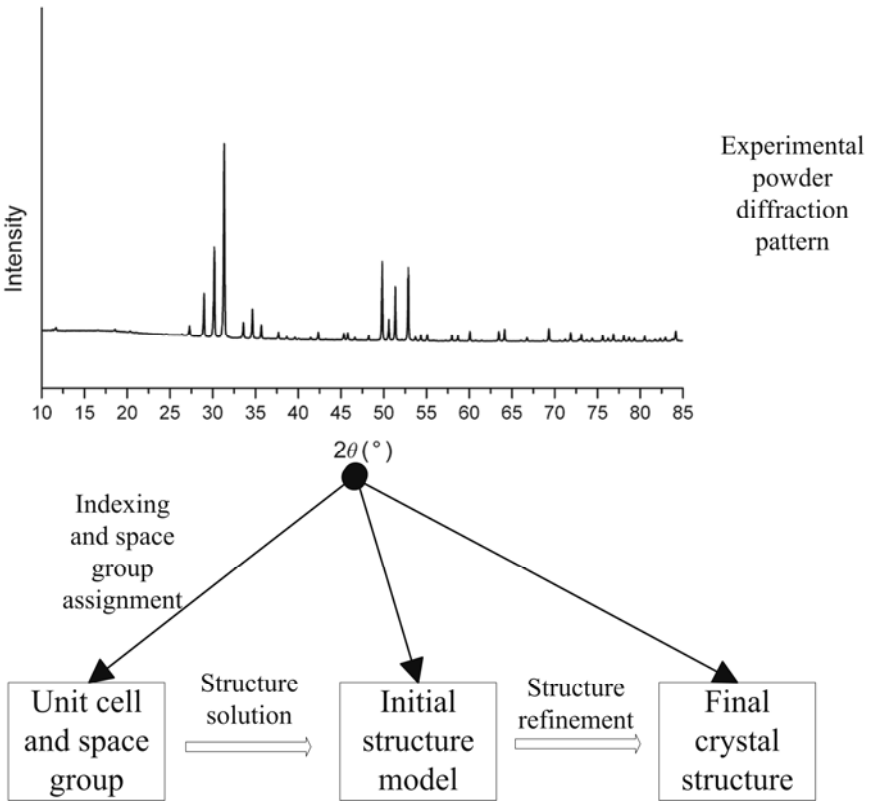

Figure 2.5 Schematic diagram illustrating the different stages involved in determination of unit cell parameters and complete structure from powder diffraction data [75] .

2.4.1.1.2 Experimental

To perform powder XRD experiments in air and moisture sensitive solids, the samples were finely ground and sandwiched between two Polyimide (Kapton) films. For this purpose special film holders made of aluminum were used. In detail, the first film was placed on the holder ring and few drops of vaseline in hexane solution were added. Having spread the powdered sample on the liquid, a thick layer of silicon fat was smeared on the periphery of the film to ensure air-tight sealing. Finally, the second protecting film was placed on top of the first one and the films were stretched and fixed by a second ring. All these procedures were done inside the glove box. For air-stable samples, only one layer of film made of Mylar was used .It is considerably cheaper but less air-tight than that of polyimide.

X-ray powder diffraction analysis was employed on a HUBER image plate Guinier-camera (Huber G670) equipped with a germanium monochromator and $CuK_{\alpha 1}$ radiation. The data collections were made in the range of $3° \leq 2\theta \leq 100°$ with a step size of 0.005° 2θ.

All X-ray powder diagrams were analyzed by using WinXPOW software package[77] . The unit cell parameters were refined with WinCSD Cell program by least-squares fitting of lattice parameters to the observed diffraction line positions by using LaB_6 as internal standard.

2.4.1.2 Single Crystal X-ray Analysis

2.4.1.2.1 Theory

Single crystal X-ray diffraction is the most important and powerful technique for elucidation of crystals and molecular structures. In order to implement the diffraction

experiment, a single crystal must be selected in which all the unit cells are identical and aligned in the same orientation. Under this condition, it will scatter cooperatively to give a clear diffraction pattern consisting of individual X-ray beams each in definite direction. The intensities of X-rays diffracted by a crystal are proportional to its volume - or more precisely - to the number of electrons of the atoms. The more electrons there are, the higher will be the scattering. On the other hand, X-rays are also absorbed by crystals and this effect exponentially increases with crystal dimensions. The extend of the absorption depends on the wavelength of the X-ray source and on chemical composition and can be very large if heavier elements are present [73]. A typical crystal size suitable for measurements is around a few tenths of millimeter. If heavier elements are present, a smaller size and uniform dimensions are preferred. In order to determine the quality of the crystal to be measured, diffracted X-rays are recorded on photographic film (Figure 2.6).

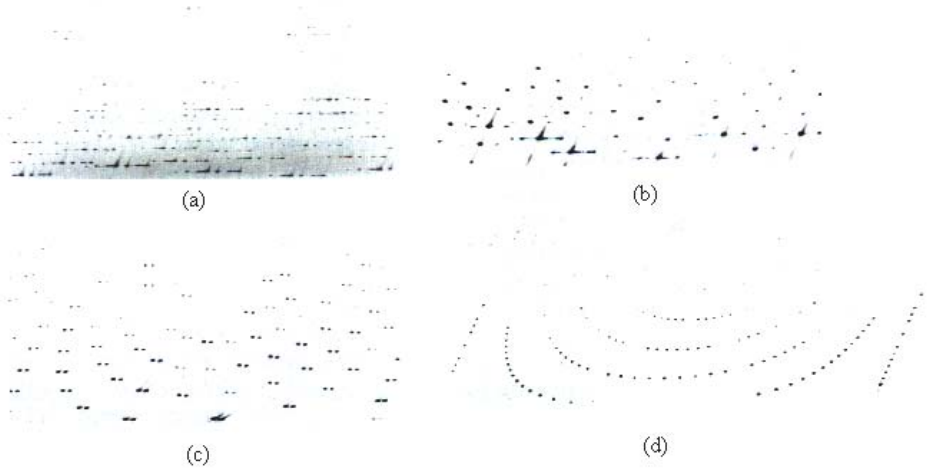

Figure 2.6 (a-c) Weissenberg exposures of crystals of minor quality for various reasons; (d) exposure of a good single crystal [78].

The crystal shown in 2.6 (a) consists of several fragments attached to each other. An overlap of neighboring reflections can easily be recognized. 2.6 (b) depicts additional reflections due to some randomly distributed crystalline satellites. Figure 2.6 (c) represents

a twinned crystal. Finally 2.6 (d) shows the Weissenberg photograph of a perfectly aligned single crystal with, sharp, undistorted reflection spots.

In the single crystal case, the Bragg equation is satisfied for only very few reflections unless the crystal is rotated. The interpretation of the recorded film is greatly assisted if the crystal is rotated about a direction of a unit cell axis. Then the next step is the assignment of Miller indices to the individual reflections which is the matter of counting along obvious rows of spots. Several types of X-ray camera have been developed over many years to achieve such effects. Since new diffractometers with area detectors have became available more recently, the use of film methods declined. After the quality of crystal is verified, the next step is to find the unit cell geometry and symmetry. With the help of obtained diffraction pattern, it is possible to assign the correct space group by comparison of intensities which are equivalent by symmetry and by noting that certain special subsets of reflections have zero intensity. With an area detector, a high degree of redundancy of symmetry-equivalent data can be provided. Data collection typically takes only a few hours regardless of the size of the structure. The result of this process is given by a file consisting of a list of reflections each with Miller indices and a measured intensity associated with standard uncertainty (s.u.) which is a measure of the precision or reliability of the measurement. After the measurement of the intensities, a data reduction or correction is necessary. Some corrections are associated with the data collection processes which are instrument dependent. The others are due to partially polarization of reflected radiation and changes in the incident X-ray beam intensity or in the scattering power of the crystal during experiment [73]. The reduction process includes the merging and averaging of repeated and symmetry equivalent measurements in order to produce a unique, corrected and scaled set of data. Having measured and appropriately corrected the diffraction data, the next step is to solve the structure in which we obtain atomic positions in the unit cell from the data. Here the objective is to recombine the individual diffracted beams to give a

picture of an electron density distribution in the unit cell. The mathematical expression of the process is,

$$\rho(xyz)=\frac{1}{V}\sum_{h,k,l}|F(hkl)|\exp[i\varphi(hkl)]\exp[-2\pi i(hx+ky+lz)] \qquad (2.2)$$

where |F(hkl)| is the amplitude and Φ corresponds to phase of a wave [73].

The amplitudes can be measured and final exponential term can be calculated for the contribution of each reflection *hkl*, to each position xyz, but the phases of the reflections are unfortunately unknown. There are several methods like Patterson, Direct methods, etc. which help us to overcome this difficulty. With the help of 'Direct methods', we can obtain approximate reflection phases from the measured intensities. Direct methods involve selecting the most important reflections, working out the probable relationships among their phases, and then trying different possible phases to see how well the probability relationships are satisfied. For the most promising combinations, Fourier transforms are calculated from the observed amplitudes and trial phases are examined for recognizable molecular features [73]. It should be known that the electron density is the Fourier transform of the diffraction pattern. Completion of the basic structure ends with the structure refinement since only a partial structure has generally been obtained by the structure solutions. While doing structure refinement, the accuracy of the present model is examined with calculation of so-called 'residual or agreement index'. It is designated by the capital letter R and called as R value. The R value is the relative average difference between the calculated structure amplitudes |Fc| and the observed structure amplitudes $|F_0|$ given by,

$$R=\frac{\sum_h |F_0(h)| - |F_c(h)|}{\sum_h |F_0(h)|} \tag{2.3}$$

Since the $|F_0|$'s are derived directly from the experiment and the |Fc|'s are calculated from the structural model, the R value can be regarded as indication of how well the model fits the real structure [78].

Variations on this definition include using F^2 values instead of |F| values, squaring the differences, and incorporating different weighting factors multiplying different reflections and hence incorporating information on the relative reliability of different measurements. One of such residual factors generally used is wR2 given by,

$$wR2=\sqrt{\frac{\sum_h w(F_0^2(h)-F_c^2(h))^2}{\sum_h w(F_0^2(h))^2}} \tag{2.4}$$

where w indicates that weights are included and 2 indicates that F^2 values are used rather than F values [73].

Goodness of fit (GooF) is another parameter for the evaluation of the quality of crystal structure refinement which is also based on F^2. Goof is given by,

$$GooF=S=\sqrt{\frac{\sum_h w(F_0^2(h)-F_c^2(h))^2}{n-p}} \tag{2.5}$$

where n and p are the number of reflections and total number of parameters refined, respectively. A correct structure model is expected to give S = 1. All these steps are shown on Figure 2.7.

Operation	**Information Obtained**
I Select a suitable crystal and mount it in / on a capillary	
II Obtain unit cell geometry and preliminary symmetry information	Unit cell parameters: a, b, c, α, β, γ crystal system, space group, molecular symmetry
III Measure intensity data	List of h, k, l, I, σ (I)
IV Data reduction (various corrections applied to data)	List of h, k, l, F, σ (F) or h, k, l, F^2, σ (F^2)
V Solve the structure with Direct methods	Some of atom positions
VI Complete the structure	All of atom positions
VII Refine the structure model	Atom positions and displacement parameters
VIII Interpret the results	Molecular geometry, packing arrangement, etc.

Figure 2.7 Flowchart for the steps involved in a single crystal structure determination [73].

2.4.1.2.2 Experimental

For single crystal X-ray analysis, a suitably sized crystal with well-formed edges and faces were picked and mounted properly on top of the sharpened end of a glass capillary. After checking the crystal quality with either Weissenberg or Laue photographs, they were mounted on a Rigaku AFC7 diffractometer equipped with a Mercury CCD detector with MoKα radiation or by a STOE IPDS diffractometer with AgKα radiation. For the low temperature single crystal measurement, the STOE IPDS automatic diffractometer was used with an open nitrogen gas stream as coolant. The structure solutions and refinements were done with the SHELXS-97 and SHELXL-97 programs found in WinGX software [79].

2.4.2 Energy / Wavelength Dispersive X-ray Fluorescence Analysis

2.4.2.1 Theory

X-ray fluorescence spectrometry (XRF) is one of the most widely used methods in element analysis. In qualitative analysis, it has unrivaled selectivity for all elements between beryllium and uranium and also for transuranium elements and an extremely wide dynamic range in quantitative analysis [80]. With XRF, the detection limits at the ppm level at great precision and accuracy can be obtained. Although other spectrometry techniques (Direct Current Plasma (DCP), atomic absorption spectrometry (AAS), neutron activation analysis (NAA), different kinds of mass spectrometry (MS), etc.) may have much lower detection limits, the wide dynamic range remains a unique feature for XRF. Two fluorescence techniques widely used for the chemical analysis of samples are energy dispersive and wavelength dispersive X-ray spectroscopy (EDXS, WDXS).

The EDXS analysis system works as an integrated feature of a scanning electron microscope (SEM)T. During the operation of SEM, the surface of the specimen is scanned with a beam of electrons. When electrons in the primary beam bombard the surface atoms, some inner shell electrons can be knocked off. In this case, higher-energy electrons from an outer shell are transferred to the inner shells causing the emission of photons in the x-ray range. The amount of released energy due to that process depends on which shells the transfers take place (Figure 2.8).

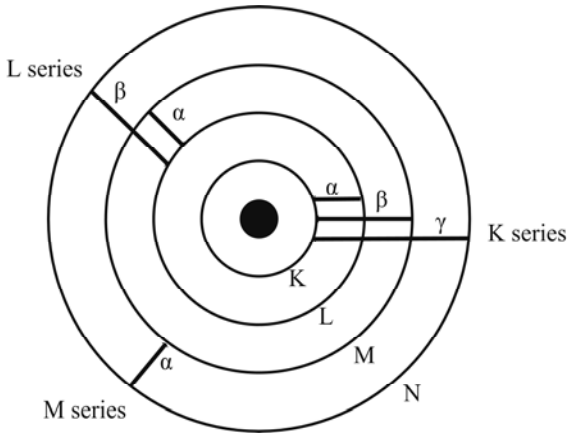

Figure 2.8 Transfer of electrons from a higher-energy to a lower-energy shell.

Since unique amount of energy is released for every element, if the photon energies of the x-rays given off by electron bombardment can be accurately measured, the atoms from which the X-ray was emitted can be identified. The energy dispersive spectrometer consists of the excitation source and the detection system (Figure 2.9a). The detector is generally so-called lithium-drifted silicon detector (Si(Li)) that resolves the energies of the x-ray photons and in conjunction with a computer-based multi-channel analyzer, provides a spectral distribution of intensities versus energy [81]. So, the result of EDXS analysis is

given on a spectrum displaying peaks corresponding to the energy levels for which the most X-rays had been received. The intense a peak in a spectrum, the more concentrated the element is in the sample.

EDXS analysis can also quantify the elements it detects. A quantitative investigation can be performed either by standards or standardless analysis. A standardless analysis quantifies the elements by calculating the area under the peak of each identified element and performs calculations to create sensitivity factors that will convert the area under the peak into weight or atomic percent. An algorithm or correction procedure mostly used is ZAF in which Z, A and F standing for atomic number, absorbance and fluorescence values [82]. From this, the atomic and weight percent are calculated. Standards quantifications are performed in a similar way except that instead of performing ZAF calculations on the areas under the elemental peaks, the areas are compared to standards files which are spectra of the elements to be quantified acquired under the exact conditions of the unknown spectrum.

WDXS analysis works in pretty much the same way as EDXS analysis, except that its detector classifies and counts the impinging X-rays in terms of its characteristic wavelengths. In WDXS, polychromatic x-ray photons are dispersed by using a single crystal or multilayered synthetic. Once the X-ray photons are dispersed, their intensities are measured using proportional and / or scintillation detector (Figure 2.9b) [81]. A wavelength dispersive spectrometer may be a single channel instrument in which a single crystal and a single detector are used for the measurement of series of wavelengths; or a multichannel spectrometer in which many crystal and detector sets are used to measure elements simultaneously [83].

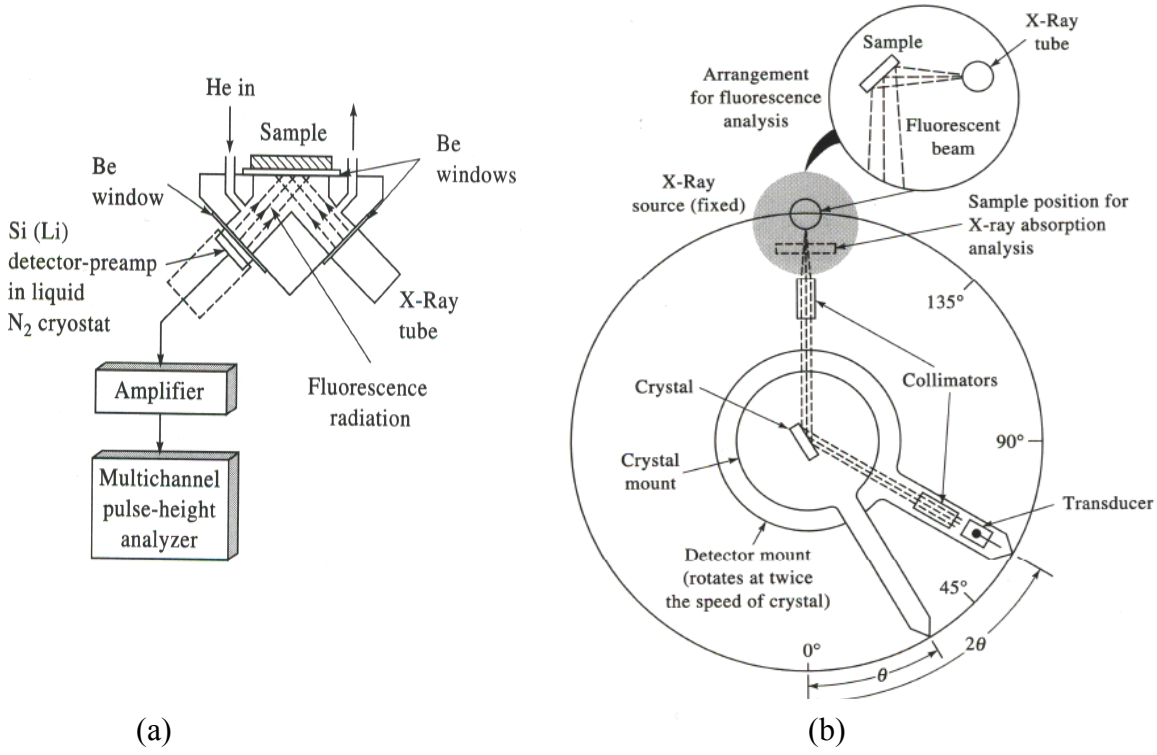

Figure 2.9 (a) EDX and (b) WDX spectrometers [84].

The limit of detection (LOD) in XRF is the concentration of analyte equivalent to two standard deviations of the background counting rate. In WDXS, it is at low ppm level with some elements especially lighter ones around tenths of a ppm. Using layered synthetic microstructures as dispersing device enables the determination of elements down to Boron. LOD for EDXS using primary excitation is generally a factor of 10 higher than WDXS primarily due to count rate limitations and lower resolution of EDXS [81]. The accuracy of detection of light elements is also much less in EDXS because the absorption of low-energy characteristic X-rays by the beryllium window on the Si(Li) detector. Recently a

polymer window detector has been commercialized providing the limit of detection down to oxygen and improving the sensitivity for most light elements [81].

2.4.2.2 Experimental

For the microstructure analysis by EDXS and WDXS, a chunk of sample was embedded in epoxy resin substrate containing carbon fibers to increase the surface conductivity (Figure 2.10).

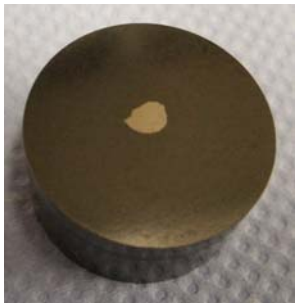

Figure 2.10 A chunk of sample embedded in epoxy resin substrate.

Grinding was performed using fixed abrasive papers mainly silicon carbide and either alcohol including lubricant or water. Polishing was done in steps by using slurry with different micron sized diamond powders (6, 3, ¼) in paraffin. After each step the specimens were cleaned with ethanol to remove all remaining particles. The measurements were carried out using Philips XL 30 SEM with integrated EDX spectrometer and Cameca SX 100 WDX spectrometers, respectively. In the former case, the data handling and the standartless quantification (ZAF) were carried out by EDAX software package. For the latter case, BaGe4, NiSi, and Ta were selected as standards and Cameca Peak Sight software was used for quantitative analysis and imaging. The optical microscope images were obtained by Light Optical Polarization Microscope (Zeiss Axio Plan 2).

2.4.3 Differential Scanning Calorimetry (DSC), Differential Thermal Analysis (DTA) and Simultaneous Thermogravimetry - Differential Thermal Analysis (DTA/TG)

2.4.3.1 Theory

Two types of differential thermal instruments are commercially available namely differential thermal analyzers (DTA) and differential scanning calorimeters (DSC). These instruments give quantitative information about endothermic, exothermic and heat capacity changes as a function of temperature. Hence, melting temperature, glass transition temperature, purity, etc. can be determined precisely with these two methods. Both techniques are based on a two-pan configuration which are sample and reference. The main difference between DTA and DSC is that the former measures temperature differences between the sample and reference pan whereas DSC measures energy differences [85].

In DTA, the difference in temperature between a sample and a reference material is measured as a function of a pre-programmed temperature cycle. Beneath the pans in an electrically heated furnace, the sample and reference thermocouples are placed (Figure 2.11).

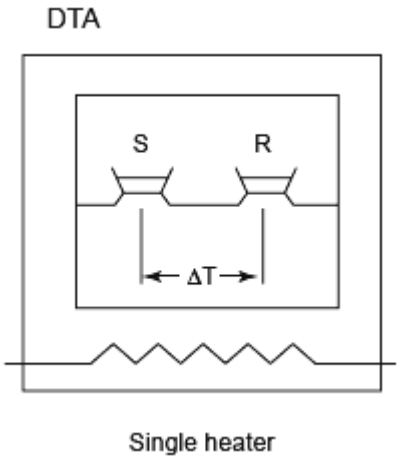

Figure 2.11 Schematic diagram of a DTA cell [85].

A microcomputer uses the sample thermocouple to control the furnace temperature in order to provide linear increase in the sample temperature. After the measurement, the difference in temperature between the sample and reference is plotted against sample temperature.

In DSC case, two types of instrumentation exist which are power-compensated DSC and heat flux DSC. Power-compensated DSCs contain two individual furnaces (Figure 2.12(a)). Temperature differences between the sample and reference are compensated by varying the heat required to keep both pans at the same temperature[85]. So, this energy difference is plotted as a function of sample temperature. Heat flux DSCs operate with a single furnace. Heat flows into both the sample and the reference material via an electrically heated constantan thermoelectric disk and is proportional to the difference in output of the two thermocouple junctions (Figure 2.12(b)) [85].

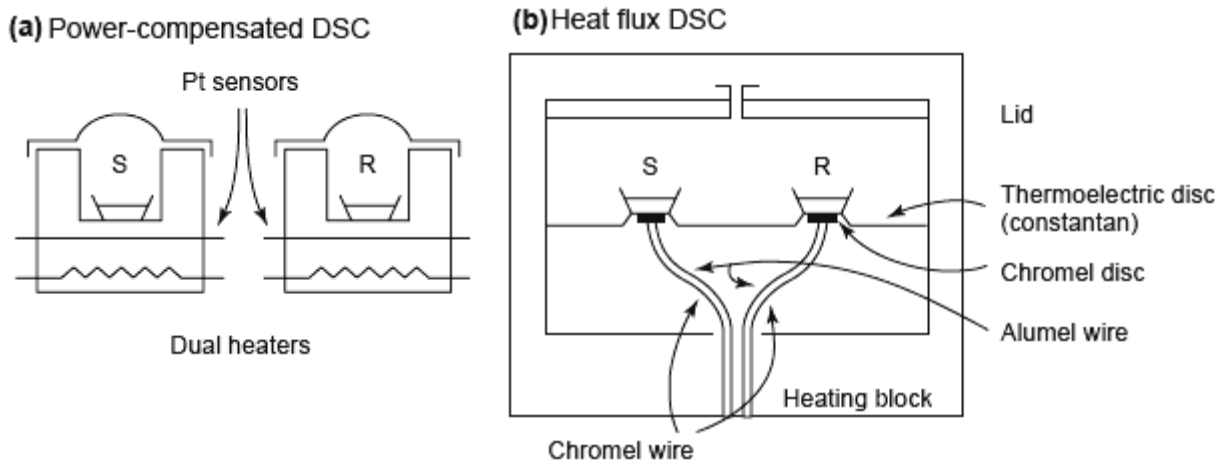

Figure 2.12 Schematic diagrams of (a) a power-compensated differential scanning calorimetry cell, (b) heat-flux differential scanning calorimetry cell [85].

Thermogravimetry (TG) is the branch of thermal analysis which examines the mass change of a sample as a function of temperature in the scanning mode or as a function of time in the isothermal mode [86]. TG curves are plotted with mass change in percent versus temperature or time. The equipment used for TG consists of a furnace measuring the temperature of the sample, a sensitive analytical balance, a purge gas system which provides either inert or reactive atmosphere, and a micro-computer / microprocessor for data recording and display.

The simultaneous application of thermogravimetry and differential scanning calorimetry as well as thermogravimetry and differential thermal analysis to a single sample yields more information than separate application in two different instruments. First of all, the test conditions are perfectly identical for the TG, DSC and DTA signals (same atmosphere, flow rate, vapor pressure on the sample, heating rate, thermal contact to the sample crucible and sensor, radiation effect, etc.). Additionally, the analyzability of the

signals is improved since two or more sets of information concerning sample behavior are always simultaneously available (differentiation between phase transformation and decomposition, between addition and condensation reactions, recognition of pyrolysis, oxidation, and combustion reactions, etc.)[87]. A schematic of instrument (NETZSCH STA 409) doing simultaneous thermal analysis and sample carriers are shown in Figure 2.13.

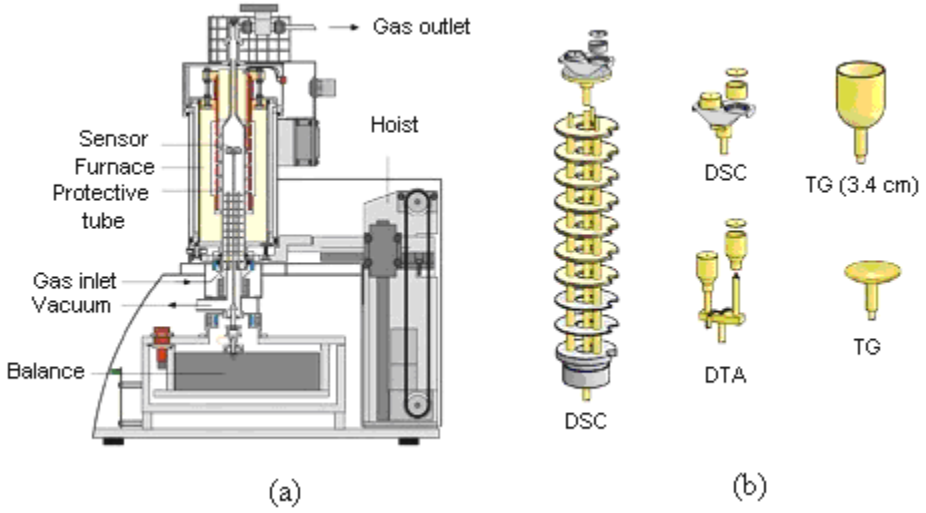

Figure 2.13 (a) Schematic of NETZSCH STA 409, (b) Sample carriers [87].

2.4.3.2 Experimental

DSC measurements are done with NETZSCH DSC 404 C instrument in which the heating is possible from room temperature to 1650 °C. DTA measurements are done with either NETZSCH DTA 404 or NETZSCH STA 409 C/CD instruments. The former one is mainly used for samples with very high melting point like TaNiSi (1852 °C). The latter has the maximum temperature limit the same as DSC instrument which is 1650 °C and the simultaneous application of thermogravimetry (TG) and DTA to a single sample is

possible. All these measurements were carried out to obtain the temperatures of the invariant reactions by applying a heating / cooling rate of 10 °C /min. Once the final temperature of the heating cycle was reached, the cooling was immediately begun without further preservation time at that temperature. All the samples were ground with an agate mortar in order to get more homogenous temperature change in grains of phases. For the air and moisture stable samples, an Al_2O_3 or Y_2O_3 crucible was used. The air sensitive measurements were performed using Nb ampoules which were sealed after filling approximately 50 mg sample in an argon-filled glove box. These instruments are also integrated inside an Ar filled glove box. In order to avoid the vibrations of a conventional glove box, the entire box table was designed as a vibration-isolated weighting table for TG measurements. Data manipulation and analysis were performed with the software program called NETZSCH (NETZSCH Proteus – Thermal Analysis-Version 4.0 beta and 4.3, NETZSCH-Geraetebau GmbH 1999). After the measurements, X-ray powder diffraction analysis was applied to the samples in order to determine the type of products formed during the heat treatment.

2.4.4 Resistivity Measurements

2.4.4.1 Theory

The electrical properties of solid materials are consequence of their band structures in sense that the arrangement of the outermost electron bands and the way in which they are filled with electrons. Four different types of band structures are possible at 0 K shown as in Figure 2.14. The difference in energy between the lowest point of the conduction band and the highest point of the valence band at 0 K is called as band gap energy E_G. The Fermi energy, E_F, correspond to the highest energy level to be occupied by an electron at 0 K. In

the first band structure (a), one outermost band is only partially filled with electrons. This energy band structure is typical for some metals, in particular those that have a single s valence electron such as copper. For the second band structure (b), the p and the s band of Mg overlaps permitting electrons to be excited into the large number of unoccupied energy levels in the combined 3s and 3p band [72]. The final two structures are similar, energy band gap lies between valence band which is completely filled with electrons and an empty conduction band. When the band structures are investigated, in some cases, the top of the valence band and the bottom of the conduction band lie at the same point in k space (reciprocal space), this is called as direct band gap. If they lie in different points, then it is called indirect band gap. Materials with band gap less than 4.0 eV is considered as semiconductor (c) and greater than that is called as insulator (d) [88].

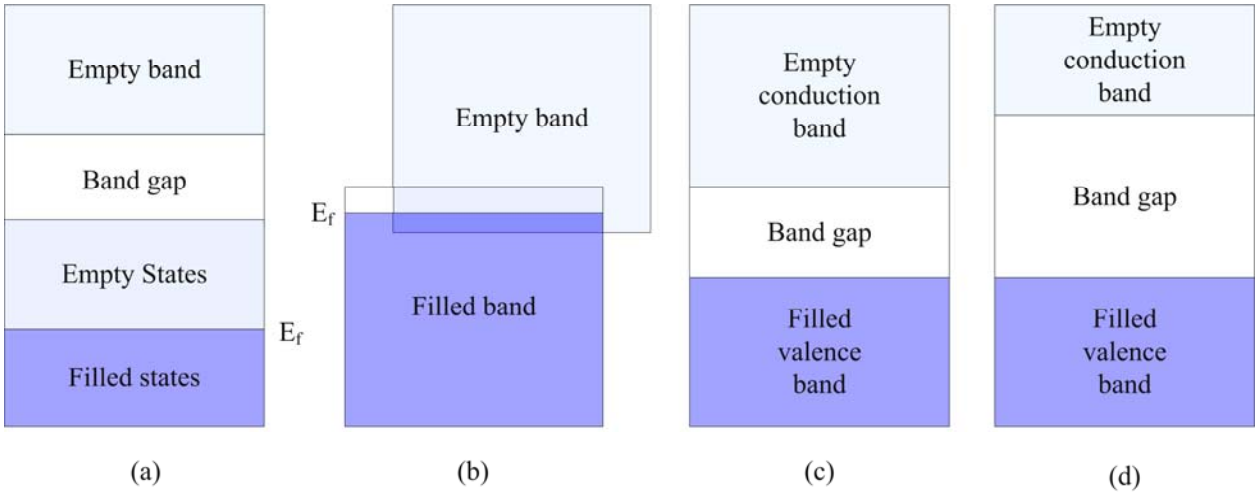

Figure 2.14 Electron band structures of (a) conductor (Cu), (b) conductor (Mg), (c) semiconductor and (d) Insulator at 0 K [72].

The resistivity ρ is independent of the specimen geometry but related to resistance of material R_m with the expression,

$$\rho = \frac{R_m A}{L} \tag{2.6}$$

where L is the distance between the two points at which the voltage is measured and A is the cross-sectional area perpendicular to the direction of the current. The unit of resistivity is ohm-meter (Ωm). The reciprocal of the resistivity is called as electrical conductivity (σ). At 300 K, metals' resistivities are less than $<10^{-6}$(Ωm), typical semimetals have ρ(300 K) in the range from 10^{-6} to 10^{-3} (Ωm), semiconductors have ρ(300K) typically in the range from 10^{-3} to 10^{8}(Ωm) and finally insulators have ρ(300 K) greater than 10^{8}(Ωm)[89].

The electrical resistivity of most metals is dominated at room temperature and increases by collision of the conduction electrons with lattice phonons and at liquid He temperature (4 K) by collision with impurity atoms and mechanical imperfections in the lattice. Hence, the net resistivity can be written as:

$$\rho = \rho_L + \rho_i \tag{2.7}$$

where ρ_L is the resistivity caused by the thermal phonons, and ρ_i is the resistivity caused by scattering of the electron waves by static defects that disturb the periodicity of the lattice [90].

An important distinction between metals and semiconductors is that the conductivity of a semiconductor increases exponentially with increasing temperature according to the equation as,

$$\sigma(T) \propto \exp(-E_g / k_B T) \tag{2.8}$$

due to increasing concentrations of charge carriers both electrons in conduction band and holes in the valence band. A hole acts in applied electric and magnetic fields as if it has a positive charge +e.

For the high-temperature data, resistivity for semiconductors can be written as,

$$\rho = \rho_0 e^{\frac{E_g}{2K_B T}} \tag{2.9}$$

where E_g is the electronic band gap and k_B is the Boltzmann constant [91]. According to the equation, the graph of ln ρ versus 1/T gives a linear relation at these temperatures. From that, energy band gap E_g can be determined for a semiconductor.

There are two types of semiconductors namely intrinsic and extrinsic. In the intrinsic case, the semiconductor is of high purity and has few defects. There are some thermally excited electrons that reside in the conduction band, and these leave behind holes in the valence band. These electrons and holes are each able to conduct an electrical current. In the extrinsic case, dopant atoms are added to the semiconductor, which may become thermally ionized and contribute either to the electrons to the conduction bands (n –type) or holes to the valence band (p-type)[89].

A superconductor is a material that exhibits zero electrical resistance under certain conditions and expels a magnetic field completely (a superconductor is also a super diamagnet). The origin of superconductivity is related to electron-phonon coupling and the resulting pairing of conduction electrons. This is explained using Bardeen, Cooper, and Schrifer (BCS) theory stating that superconductivity occurs as a result of the formation of pairs of electrons known as Cooper pairs [88]. Superconductivity in materials disappears above a certain temperature known as the critical temperature (T_c).

2.4.4.2 Experimental

The resistivity measurements of the polycrystalline samples were performed by standard four-point dc method with cryostat in an Ar filled glove box. All the samples were ground with a tungsten carbide mortar and then pressed under 5 kPa/cm^2 pressure to a pellet in a rectangle prism shape with well defined edges (length ≈ 4.0mm, width ≈ 1.5mm, height ≈ 1.0mm). The contacts were made by silver-filled epoxy glue with using either wires of 30 μm in diameter Pt or 50 μm in diameter Cu (Figure 2.15). The pellets with the attached probes were then mounted on the top of a chip, which was then connected to the multimeter with the aid of four coaxial wires. The resistivity measurements of pressed pellets were performed at temperatures in the range of 3.8 - 320 K.

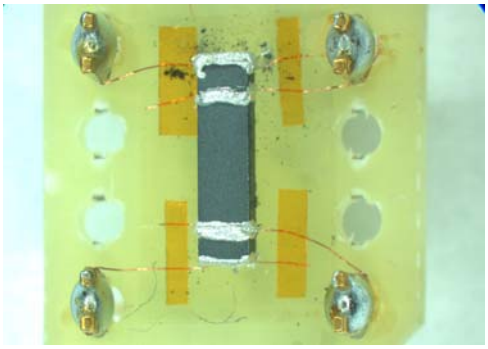

Figure 2.15 Pressed and contact attached pellet for resistivity measurement.

2.4.5 Specific Heat Capacity Measurements:

2.4.5.1. Theory

The amount of heat which must be supplied to raise the temperature of unit mass by one degree is called as the specific heat. Heat capacity or the specific heat is determined mainly by the lattice structure. The vibration of a crystal lattice is related to the heat content of the system and so to the thermodynamic temperature. From classical statistical thermodynamics, heat capacity is constant and proportional to the equation given by,

$$C_v = 3Nk_B = 24.94\ Jmol^{-1}K^{-1} \qquad (2.10)$$

where N is the number of atoms($N = N_0 = 6.02x10^{23}$ atoms for one mole of material) and k_B is the Boltzmann constant. This is the classical value of the heat capacity predicted by the Dulong-Petit law [92]. However this law applies only at high temperatures because heat capacity varies as the temperature changes. Therefore a more sophisticated and applicable theory is necessary especially at low temperatures.

The quantum corrections to the theory of heat capacity were achieved by both Einstein and Debye. Einstein predicted that the lattice vibrations of crystalline solids should be quantized and so only certain vibrational modes are allowed. These vibrational quanta are called phonons [92]. If we consider a single oscillator that is oscillating at frequency ω and contains N_0 atoms then according to Einstein theory C_v is written as:

$$C_v = 3N_0k_B(\frac{h\omega}{k_BT})^2 \frac{\exp(\frac{h\omega}{k_BT})}{\left(\exp(\frac{h\omega}{k_BT})-1\right)^2} \qquad (2.11)$$

At high temperatures, we approximate exp ($\hbar\omega/k_BT$) to 1 + $\hbar\omega/k_BT$ providing the same result as Dulong-Petit law which is $C_v = 3N_0k_B$. Hence, the Einstein model of the heat capacity works quite well for intermediate or high temperatures but it predicts a rapid decrease of the heat capacity as the temperature is reduced which is not in accordance with the experimental observations. Therefore the theory is not applicable at low temperatures and so further correction was provided later on by Debye. The idea of single frequency Einstein theory was extended by Debye and the interactions between atoms were allowed providing more frequencies from the Einstein frequency down to acoustic range. Heat capacity according to Debye model is,

$$C_v = 9N_0k_B(\frac{T}{\theta_D})^3 \int_0^{\frac{\theta_D}{T}} \frac{x^4\exp(x)}{\left(\exp(x)-1\right)^2} dx \qquad (2.12)$$

in which $x = \hbar\omega / k_BT$ and $\theta_D = \hbar\omega_D / k_B$ known as Debye temperature oscillating with ω_D above which the oscillators behave classically. At low temperatures, the expression 2.12 turns to:

$$C_v = \frac{12\pi^4}{5} N_0k_B(\frac{T}{\theta_D})^3 \qquad (2.13)$$

giving the experimentally observed dependence of the heat capacity on T^3 at low temperatures. In the same sense, the integral gets $(\theta_D/T)^3/3$ at high temperatures and $C_{v,m}$ becomes equal to $3N_0k_B$ as expected to be classical Dulong-Petit result. Therefore Debye model applies across the entire temperature range. At temperatures much below Debye temperature, the specific heat capacity of metals can be written as the sum of electron and phonon contributions:

$$C_p = \gamma T + \beta T^3 \tag{2.14}$$

where γ and β are the electronic Sommerfeld term and Debye T^3 lattice term (phononic term), respectively [93]. A plot of C_p /T versus T^2 should yield a straight line with an intercept γ and a slope of β.

2.4.5.2 Experimental

Low-temperature specific heat, C_p, was measured in the temperature range 1.8-320 K using a thermal-relaxation type microcalorimeter in a ^{3}He cryostat. A big piece of specimen (≈30mg) was thermally anchored with small amount of an Apiezon N grease (≈0.06mg) to a sapphire holder on which thin films of ruthenium oxide and nickel-chromium alloy were deposited to serve as a temperature sensor and joule-heating element, respectively. The holder then was thermally linked by four Au-Cu alloy wires to a temperature regulated copper block. The heat capacity of the sample holder and grease were measured separately for addenda correction.

2.4.6 Thermal Conductivity Measurement

2.4.6.1 Theory

The rate of flow of heat per unit temperature gradient through the material is described as the thermal conductivity K [92]. The thermal conductivity coefficient K is defined in Fourier's law given by,

$$J_Q = -K\nabla T \tag{2.15}$$

in which J_Q is the thermal flux, K is the thermal conductivity (in unit of W/mK) and ∇T is the temperature gradient [89]. The minus sign in above expression indicates that the direction of the heat flow is from cold to hot, or down the temperature gradient. From the elementary kinetic theory of gases, we can define the thermal conductivity as,

$$K=\frac{1}{3}C_v vl \tag{2.16}$$

where ν is the average particle velocity, and l is the mean free path.

Unlike electrical conduction which is only due to the movement of electrons, thermal conduction involves the contribution of both electrons and phonons (wave packets with particle-like properties). So, we can write the total thermal conductivity as,

$$K = K_e + K_p \tag{2.17}$$

where K_e and K_p are the electron and phonon contributions, respectively [94].

The velocity of phonons is assumed to be constant and approximately equal to the velocity of sound in material. The mean free path of the phonons is more complicated to estimate since two main factors are pronounced as geometrical scattering (interaction with impurities and imperfections) and scattering with other phonons. At low temperatures, there is not much thermal energy and so there is relatively few phonons lessening the chance of phononic interactions. Since at low temperatures the energy of phonon is less, the wavelength is large and these phonons are not easily scattered by the impurities and imperfections. On the other hand, at high temperatures the energy increase and the wavelength decrease of phonons increase both phononic and impurity-imperfection interactions. Hence, the mean free path of the phonons decreases as the temperature increases [94]. Since the heat capacity decreases for temperatures below Einstein or Debye temperature and drops to zero at 0 K, we conclude that the thermal conductivity attains a maximum somewhere in the intermediate range of temperature [95].

Considering the thermal conductivity of electrons, the velocity of the electrons at the Fermi surface is about 1000 times larger than that of phonons[94]. Like in electrical conductivity, it is assumed that the electrons close to the Fermi surface can contribute to the thermal conductivity [92]. Thinking that the mean free path is almost the same for both electrons and phonons, then one can easily derive that the electron contribution to the heat capacity of a metal is about 10 times larger than that of phonons(see equation 2.16)(specific heat capacity of electrons is only 1 % of that due to phonons) [94]. One may therefore expect that the thermal conductivity of metals is mainly dominated by the behavior of the free electrons at the Fermi energy level. Nonmetals, having less or no free electrons are expected to have thermal conductivities an order of magnitude less than that of metal.

More specifically, the temperature dependence of lattice thermal conductivity, $\kappa_{L,}$ is found as obeying T^3 behavior at low temperatures ($C_v(T) \propto T^3$, $l(T) \approx$ constant), T^{-p} at temperature above Debye temperature($C_v(T) \approx$ constant, $l\ (T) \approx 1/T^P$, and $1 \leq p \leq 2$) and

diminishing at high temperatures[89]. Correspondingly, the temperature dependence of thermal conductivity for metals is deduces as T, T^{-2} and T^{0} with respect to the temperature ranges specified above [96].

The Wiedemann-Franz law states that for metals not in too low temperatures, there is a relationship between electrical resistivity and thermal conductivity given as,

$$\kappa_e = \frac{LT}{\rho} = (2.45 \times 10^{-8}\ W\Omega/K^2)\frac{T}{\rho} \qquad (2.18)$$

The constant number is called as Lorenz number [96].

Generally, the room temperature thermal conductivity values for metals, ceramics and polymers range as 20 - 400, 2 - 50, and 0.3 - 1 W/Km, respectively. Semiconductors like Ge, Si and GaAs have very few electrons that can transport heat, so their thermal conductivities are less than that of metals and more representative of lattice contribution. Corresponding room temperature thermal conductivities are stated as 64, 124 and 56 W/Km for Ge, Si and GaAs, respectively [89]. Exceptionally high value for K of diamond (1000W/Km) is attributed to high speed of sound associated with the strong sp^3 covalent bond structure, and long free path due to the perfect crystallinity.

2.4.6.2 Experimental

For the thermal conductivity measurement, the usual steady-state method was employed. The samples were ground with a tungsten carbide mortar and then pressed under 5 kPa/cm^2 pressure to a pellet in a rectangle prism shape with well defined edges (length ≈ 4.0mm, width ≈ 1.5mm, height ≈ 1.0mm). The temperature gradient of both ends of the pellet was measured by two Cernox thermometers.

2.4.7 Magnetic Property Measurements

2.4.7.1 Theory

The origins of magnetism and ultimately of the magnetic properties of materials essentially result from the spin and orbital motions of electrons, the magnetic moments of electrons and the resulting magnetic moments of atoms and ions [89]. Hence magnetism is essentially a quantum mechanical phenomenon.

Independent of particular type of magnetism in a material, its macroscopic response to an external magnetic field, H, can be characterized by the resulting magnetic induction, B, present in the material in a simple relation,

$$B = \mu H \tag{2.19}$$

in which μ corresponds to magnetic permeability of the material.

Alternatively, the magnetic response can be expressed in terms of magnetization M induced by the field H as,

$$M = \chi H \quad \Rightarrow \quad \chi = \frac{M}{H} \tag{2.20}$$

where χ is the magnetic susceptibility of the material.

In SI system of unit and cgs-emu system (Gaussian system) the relationship between B, M, and H hold as,

$$B = \mu_0(H+M) = (1+\chi)\mu_0 H = \mu_r \mu_0 H \text{ (SI)}, \; B = H+4\pi M = (1+4\pi\chi)H \text{ (cgs-emu)} \tag{2.21}$$

$$\mu = (1 + \chi)\mu_0 = \mu_r\mu_0 \quad \text{(SI)}, \qquad \mu = 1 + 4\pi\chi \quad \text{(cgs-emu)} \tag{2.22}$$

where $\mu_0 = 4\pi$ x 10^{-7} N/A^2 is called as permeability of free space and μ_r is the relative permeability of the material [89].

There are several different types of magnetic materials which can be put into three traditional categories as diamagnets ($\chi<0$, $\mu_r<1$), paramagnets ($\chi>0$, $\mu_r\geq1$), and ordered magnetic materials ($\chi > 0$, $\mu_r \geq 1$) like ferromagnets, antiferromagnets, ferrimagnets, etc.

The classical derivation of diamagnetic susceptibility is based on Langevin theory [97]. According to that theory it is given by,

$$\chi = -\frac{N_v\mu_0 Ze^2}{6m_e}\left\langle r^2\right\rangle_{av} \text{ (unitless) (SI)}, \quad \chi = -\frac{N_v Ze^2}{6m_e c^2}\left\langle r^2\right\rangle_{av} \text{ (emu/cm}^3\text{)(cgs-emu)} \tag{2.23}$$

in which Z is the number of electrons, $\langle r^2\rangle_{av}$ refers to the average of occupied orbital radii, N_v is the number of atoms per unit volume, c is the speed of light, and finally m_e corresponds to the mass of the electron [97]. From 2.23, one can easily derive that the susceptibility is always negative and except for $\langle r^2\rangle_{av}$ there is no explicit temperature dependence.

The Langevin theory explains also the temperature dependence of susceptibility for paramagnetic materials assuming that the non-interacting magnetic moments on atomic sites are randomly oriented as a result of their thermal energy. When an external field is applied, the orientations of the atomic moments shift slightly toward the field direction. Corresponding susceptibility is found as,

$$\chi = \frac{N\mu_0 m^2}{3k_B T} = \frac{C}{T} \quad \text{(SI)} \qquad \chi = \frac{Nm^2}{3k_B T} = \frac{C}{T} \quad \text{(cgs-emu).} \tag{2.24}$$

Above equation is known as Curie law in which m is magnetic moment per atom, and *C* is the Curie constant. It simply states that the susceptibility of a paramagnet is inversely proportional to the temperature. A plot of inverse susceptibility versus temperature gives a straight line in which the slope is equal to the inverse of Curie constant.

In fact many paramagnetic materials do not obey the Curie law instead follow a more general temperature dependence given by Curie-Wiess law:

$$\chi = \frac{C}{T - \theta} \tag{2.25}$$

The difference in both approaches is that in Curie law it is assumed that the localized atomic magnetic moments do not interact with each other at all, they are just reoriented by the applied magnetic field. Weiss put in the equation 2.25 the existence of an internal interaction between localized moments which corresponds to a mutual interaction between the electrons tend to align the dipole moments parallel to each other[97].

When $T = \theta$, there is a divergence in the susceptibility corresponding to the phase transition to spontaneously ordered phase. The curie temperature is the temperature above which the spontaneous magnetization vanishes; it separates the disordered paramagnetic phase at $T > T_c$ from the ordered ferromagnetic phase at $T < T_c$ [90]. For antiferromagnets, the ordering temperature is known as Néel temperature (T_N).

In the Langevin theory we assumed that the electrons in the partially occupied valence shells were fully localized on their respective atoms. However, it is known that electrons in metals are able to migrate through the lattice and give rise to electrical conductivity. So this

theory is not sufficient in explaining the paramagnetism in metals completely. It was observed that the magnetic susceptibilities of paramagnetic metals is more or less independent of temperature which is a phenomenon explained by Pauli paramagnetism. This theory considers valence electrons in a solid as completely ionized from their parent atoms, and behave like a 'sea' of electrons. According to that model the expression for paramagnetic susceptibility is given as,

$$\chi = \frac{3N\mu_0 m^2}{2E_F} \quad \text{(SI)} \qquad \chi = \frac{3Nm^2}{2E_F} \quad \text{(cgs-emu)} \tag{2.26}$$

where N is total number of conduction electrons per unit volume, and E_F is the Fermi energy.

In a ferromagnet the individual magnetic moments of atoms are lined up in the same direction below T_c. Hence instead of acting individually, magnetic moments act like one very large magnetic moment. The very basic difference between a ferromagnet and paramagnet is that although all moments within a domain for a ferromagnet are aligned in the same direction, the orientation of any moment for a paramagnet is random and each moment act nearly independent from each other. Ferromagnets have very distinct T and H dependent magnetization curves. The important features are that the curves are not linear and the behaviors are not reversible. This lack of reversibility is called as magnetic hysterisis. Figure 2.16 shows that while H increasing, the magnetization gradually reaches a maximum value known as the saturation magnetization (M_s).

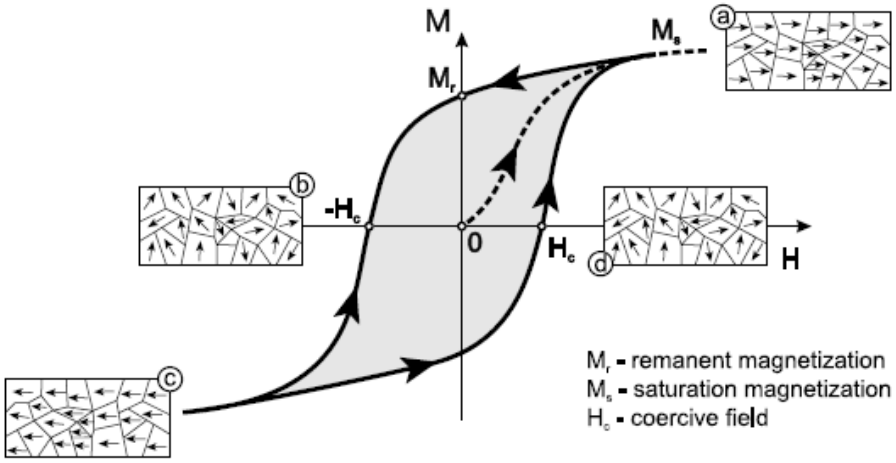

Figure 2.16 Magnetization versus magnetic field strength for a ferromagnet [98].

From the figure it is also seen that although H is reduced back to zero, M does not go to zero but has a value called as the remanent magnetization (M_r). Whereas the saturation magnetization is an intrinsic property of a sample, the ramanent magnetization depends on the sample preparation. To demagnetize a ferromagnetic material, a strong magnetic field at opposite direction (H_c) has to be applied.

Antiferromagnetism and ferrimagnetism will not be discussed here in detail since they are out of scope of the magnetic susceptibility results of the research (see more in Table 2.2, [99]).

For the understanding of the spontaneous magnetization in Table 2.2, two phenomena are to be considered: bulk magnetization which occurring after a ferromagnet has been subjected to a magnetic field and the microscopic or spontaneous magnetization which is the magnetization within a domain. Spontaneous magnetization M_s is close in value to saturation magnetization M_0 and as the temperature T is reduced to 0 K , M_s(T) approaches to M_0 [92].

Table 2.2 Classification of materials by their magnetic properties

Class	Critical Temperature	Magnitude of χ	Temperature variation of χ	Spontaneous magnetization	Structure on atomic scale	Examples
Diamagnetism	None	$\approx -10^{-6}$ to -10^{-5}	Constant	None	Atoms have no permanent dipole moments	Inert gases; many metals, e.g. Cu, Hg, Bi; non-metallic elements, e.g. B, Si,P,S; many ions, e.g. Na^+, Cl^-; and their salts; most diatomic molecules, e.g H_2,N_2; water; most organic comounds.
Paramagnetism	Curie temperature θ_c	$\approx +10^{-5}$ to $+10^{-3}$	$\chi = C / (T-0)$	None	Atoms have permanent dipole moments.Neighbouring moments don't interact	Some metals, e.g. Cr,Mn; some diatomic gases, e.g. O_2,NO; ions of transition metals and rare earth metals, and their salts; rare earth oxides.
Ferromagnetism	Curie temperature θ_c	Large(χ_c)	Above θc, $\chi = C / (T-0)$, with $\theta \approx \theta$c	Below θ_c, $M_s(T)/M_s(0)$ against T/θ_c follows a universal curve; above θ_c, none	Atoms have permanent dipole moments.Interaction produces ↑↑ allignment	Transition metals Fe,H,Co,Ni; rare earths with $64<Z<69$; alloys of ferromagnetic elements; some alloys of Mn, e.g. MnBi, Cu_2MnAl
Antiferromagnetism	Néel temperature θ_N	As paramagnetic	Above θ_N, $\chi = C / (T\pm\theta)$, with $\theta \neq \theta_N$; below θ_N, χ decreases, anisotropic	None	Atoms have permanent dipole moments.Interaction produces ↑↓ allignment	Many compounds of thransition metals, e.g. MnO, CoO, NiO, Cr_2O_3, MnS,MnSe,$CuCl_2$
Ferrimagnetism	Curie temperature, θ_c	As ferromagnetic	Above θc, $\chi \approx C / (T\pm\theta)$, with $\theta \neq \theta$c	Below θ_c, does not folow universal curve; above θ_c, none	Atoms have permanent dipole moments.Interaction produces ↑↓ allignment, but moments are unequal	Fe_3O_4(magnetite); γ-Fe_2O_3(maghemite); mixed oxides of iron and other elements

2.4.7.2 Experimental

The measurements of magnetic susceptibilities of samples were carried out with a Quantum Design's Magnetic Property Measurement System (MPMS XL – 7, Quantum Design). The principle components of this measurement system comprise temperature controller system, magnet control system, superconducting SQUID (superconducting quantum interference device) amplifier system, sample handling system and computer operating system (Figure 2.17) [100]. In order to do the measurements, the samples were sealed inside a pre-calibrated thin walled quartz tube (wall thickness 1 mm) under a He-pressure of 400 mbar (Figure 2.18). The magnetic susceptibilities were measured in the temperature range of 1.8-300 K with a fixed magnetic field from 20 Oe to 70 kOe (1Oe=79.6 A/m).

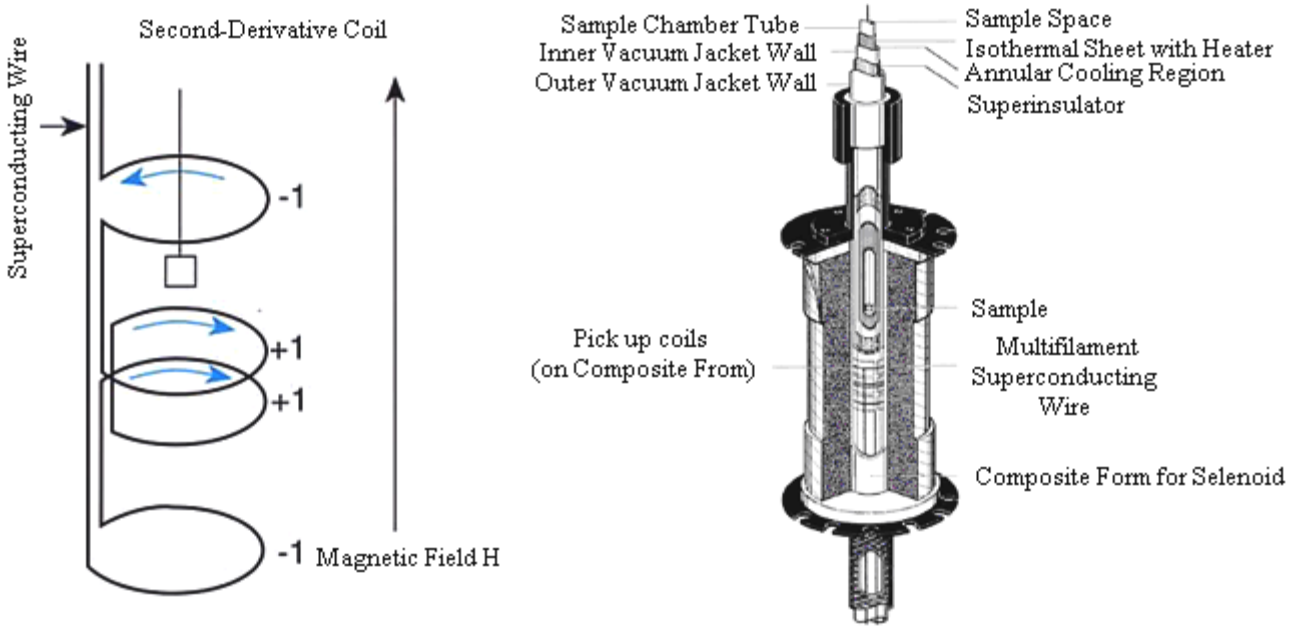

(a) (b)

Figure 2.17 The configuration (a) and location (b) of the second order gradiometer superconducting detection coil. The coil sits outside of the sample space within the liquid Helium bath.

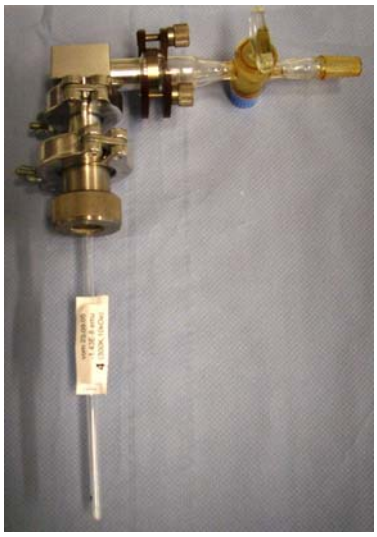

Figure 2.18 Setup of a sample for magnetic susceptibility measurement.

Chapter 3

CLATHRATE I COMPOUNDS OF Ba WITH TRANSITION METAL, Si AND Ge FRAMEWORK

3.1 Synthesis

In order to investigate the stable phase range of $Ba_8(Ni_xGe_y\square_z)Ge_{40}$ ($\square$ = defect; x+y+z = 6), the stoichiometric amounts of elemental Ba, Ni foil and finely ground Ge powder were weighed in different compositions and melted in a high frequency induction furnace in sealed Ta ampoules. To optimize the preparation conditions, the annealing temperatures of the samples were determined according to the reinvestigated Ba-Ge phase diagram at the germanium-rich part by Carrillo-Cabrera et al.(T > 430 °C; 75-100 at.% Ge) (Figure 3.1) [34].

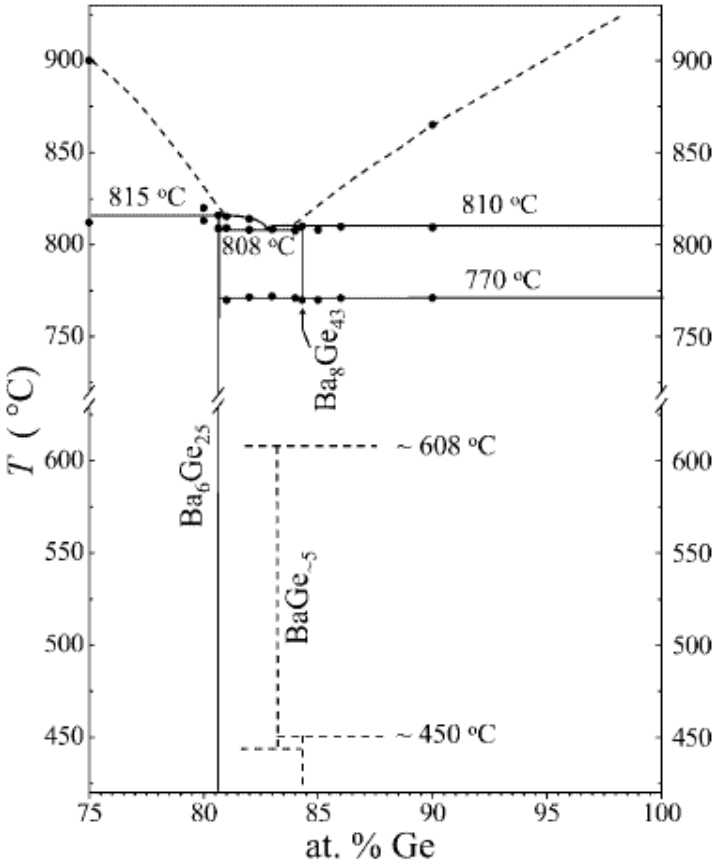

Figure 3.1 Phase diagram of the Ba-Ge system in the germanium - rich region.

It was found that at higher temperatures (770-810 °C), Ba_8Ge_{43} is a stable phase. The temperature 810 °C corresponds to peritectic decomposition temperature of the same compound. Quenching was reported to be also required since any stable phase of ternary Ge clathrates may decompose into Ba_6Ge_{25} and a metastable phase $BaGe_5$ together with Ge at relatively lower temperatures. In the light of the phase diagram, the long time annealing was performed in sealed quartz tubes at 700 °C for 4 days followed by water quenching.

The samples with Pd and Pt ($Ba_8(Pd,Pt)_xGe_y\square_z)Ge_{40}$ ($\square$ = defect; x+y+z = 6) were prepared with elemental Ba, Pd-Pt granules and finely ground powder at the same conditions as Ni case.

It is observed that although the germanium clathrates are prepared with IF at relatively low temperatures (700-800 °C), the silicon clathrates generally require moderately high pressures (3-5GPa) and temperatures (800-1300 °C) [6,7]. $Ba_8(Ni_xSi_y\square_z)Si_{40}$ compounds were synthesized from elemental Ba, Ni foil and finely ground Si powder in a glassy carbon crucible. The synthesis route followed in this study is based on single annealing of the reactants at 1000 °C for four days without any pressure application. The applied method yielded almost in all cases mono-phase products.

All samples were prepared in argon-filled glove box (content of O_2, $H_2O \leq$ 1ppm). The reaction products were metallic gray and relatively stable to air and moisture. Their phase purity was checked by X-ray powder diffraction method. The analysis was performed on a HUBER image plate Guinier-camera (Huber G670) equipped with a germanium monochromator and $CuK_{\alpha 1}$ radiation. The data collections were made in the range of $3° \leq 2\theta \leq 100°$ with a step size of 0.005° 2θ. Figures 3.2-3.6 show the observed and calculated powder patterns from the structure determination. The good agreements for the clathrates with Ni underline the high purity of the samples. For the Pd and Pt cases, trace impurity of Ba_6Ge_{25} was observed.

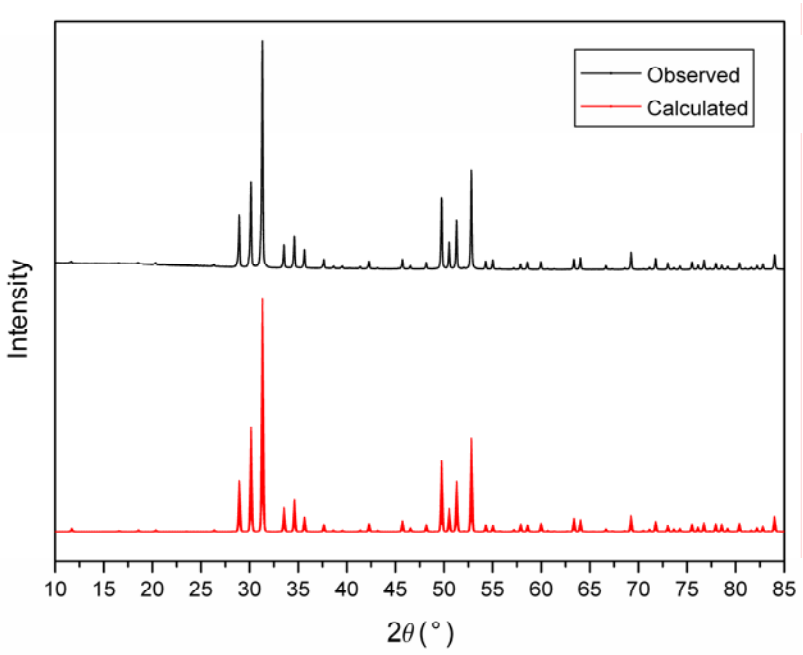

Figure 3.2 Observed and calculated X-ray powder diffraction patterns of $Ba_8Ni_4Ge_{42}$.

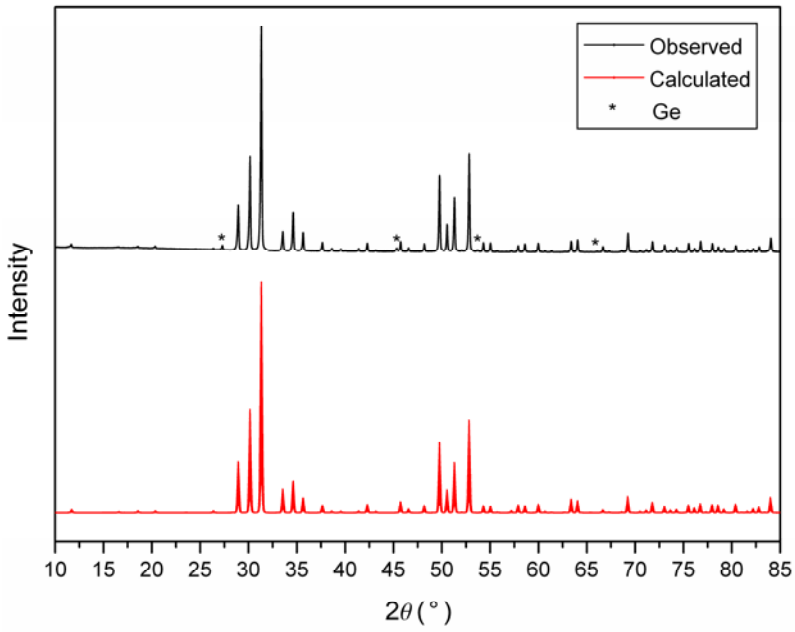

Figure 3.3 Observed and calculated X-ray powder diffraction patterns of $Ba_8Ni_3Ge_{43}$.

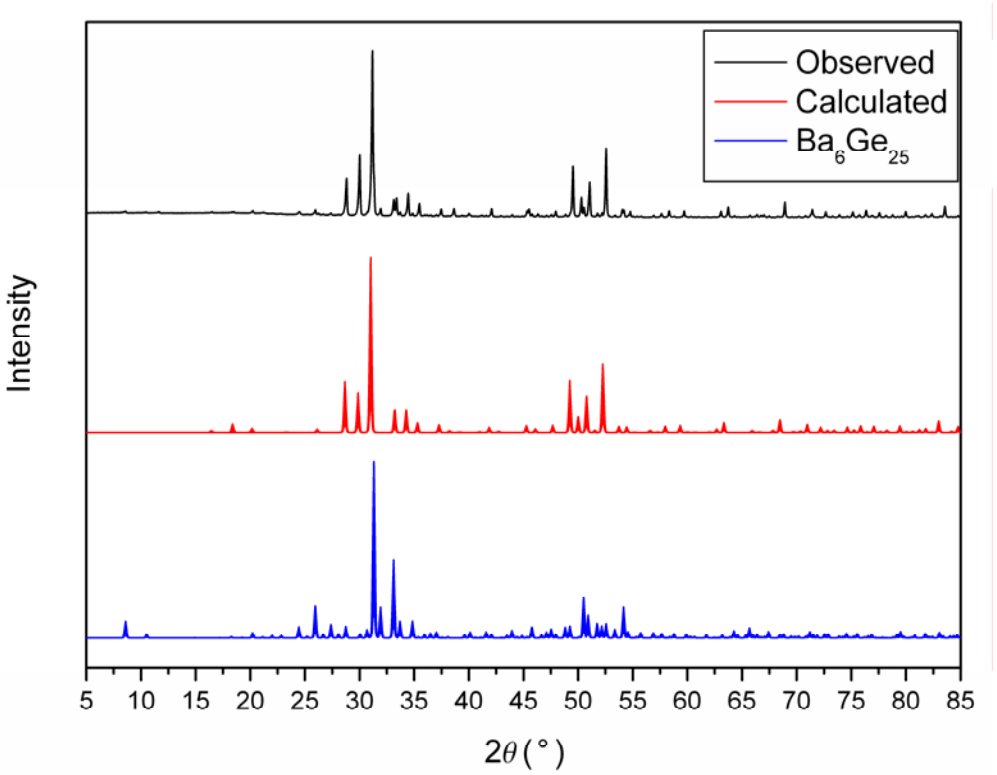

Figure 3.4 Observed and calculated X-ray powder diffraction patterns of $Ba_8Pd_{2.5}Ge_{43.5}$.

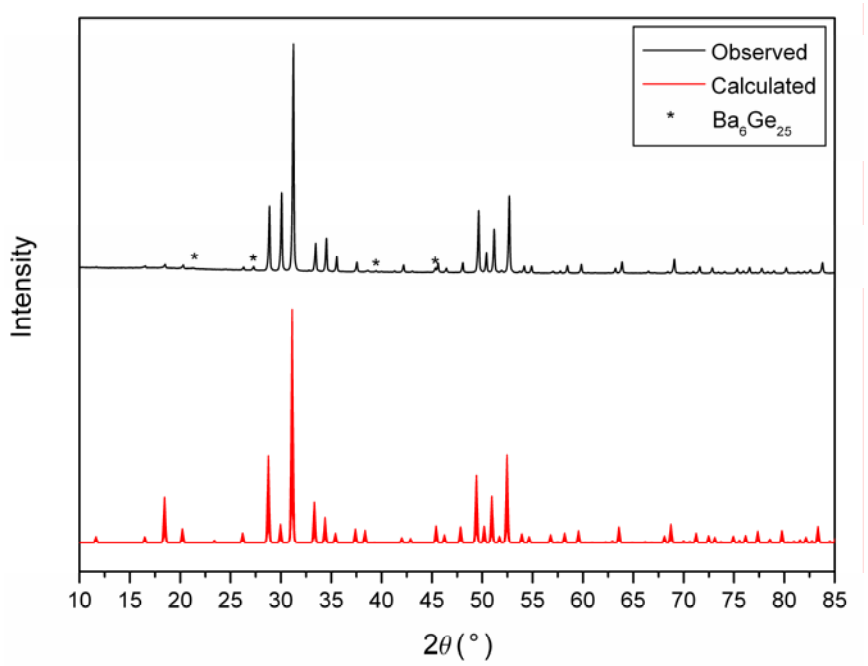

Figure 3.5 Observed and calculated X-ray powder diffraction patterns of $Ba_8Pt_{1.9}\square_{0.5}Ge_{43}$.

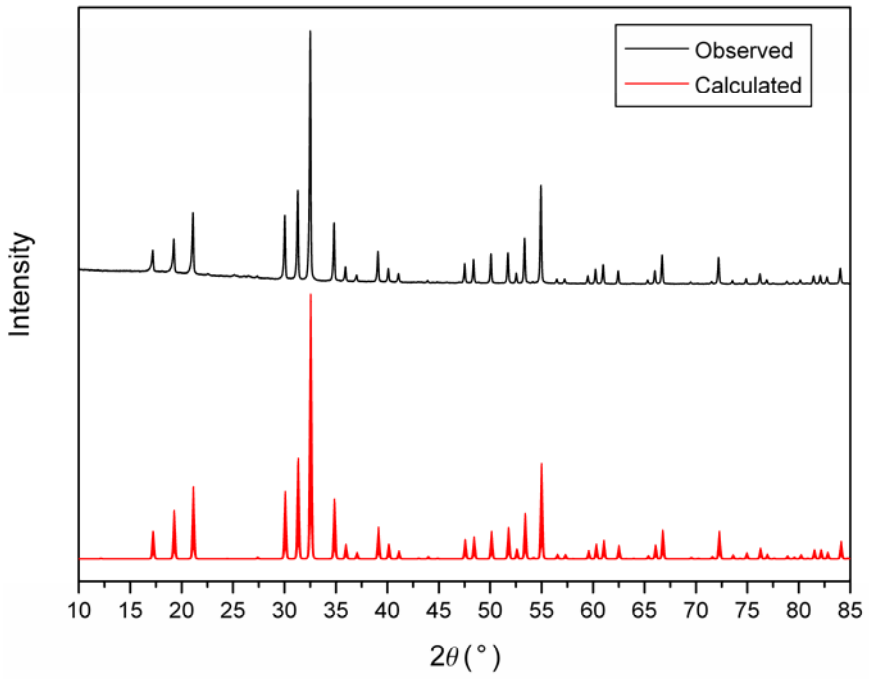

Figure 3.6 Observed and calculated X-ray powder diffraction patterns of $Ba_8Ni_{3.3}\square_{0.7}Si_{42}$.

3.2 Microstructure Analyses

The microstructure analyses were performed on a chunk of sample embedded in epoxy resin substrate containing carbon fibers which increase the surface conductivity. Grinding was performed using fixed abrasive papers mainly silicon carbide and either alcohol including lubricant or water. Polishing was done in steps by using slurry with different micron sized diamond powders (6, 3, ¼) in paraffin. After each step the specimens were cleaned with ethanol to remove all remaining particles. For the WDXS measurements, $BaGe_4$, NiSi, Pd, and Pt were selected as standards.

The WDXS analyses were performed at ten different points on the polished clathrate surfaces. The back-scattered electron (BSE) micrographs, and optical microscope images are shown below. The averages of the WDXS results are also tabulated. It should be kept in mind that one selected chunk taken from the polycrystalline powders may not be representative for the exact compositions of whole samples. This fact has been also taken into account for the interpretations of the microstructure analyses.

The WDXS analysis for $Ba_8Ni_4Ge_{42}$ resulted in the composition $Ba_{8.0}Ni_{4.0}Ge_{41.6}$ (Figure 3.7 and Table 3.1).The EDXS analysis shows that the sample consists of some trace amount of randomly distributed Ta, $BaGe_2$ and NiGe phases (Figure 3.8).

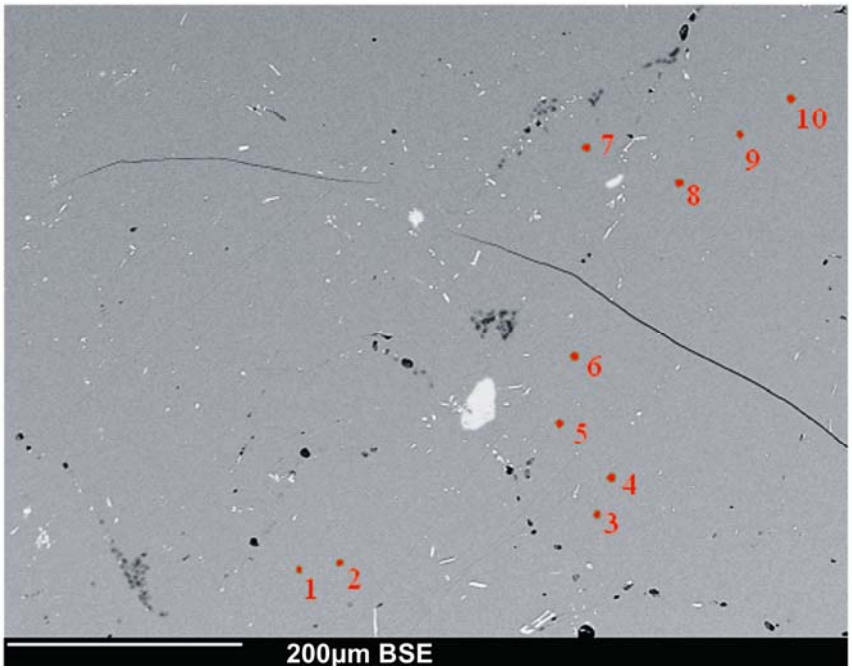

Figure 3.7 Back-scattered electron micrograph for $Ba_8Ni_4Ge_{42}$ with the points in which the measurements were performed.

Table 3.1 WDXS quantification result for $Ba_8Ni_4Ge_{42}$ at ten different points on the sample**.**

Average	Weight %	NormWeight %	Atomic %	Dev_Wt
Ba	24.92	25.24	14.92	0.03
Ni	5.39	5.46	7.55	0.01
Ge	68.44	69.30	77.53	0.19
Total	98.75	100.00	100.00	

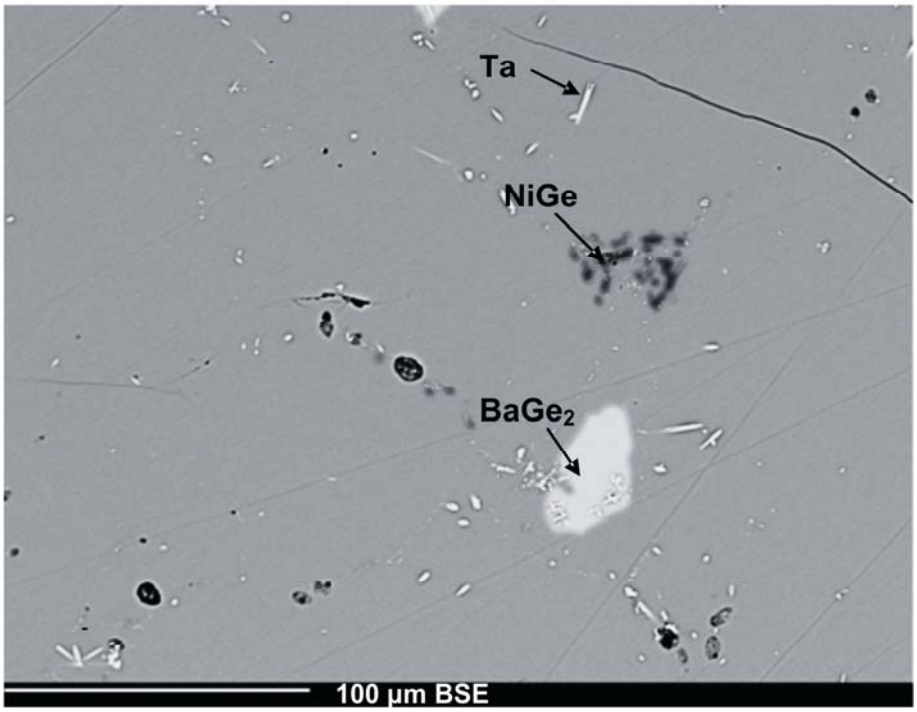

Figure 3.8 Back-scattered electron image of $Ba_8Ni_4Ge_{42}$ showing the additional phases.

The same analyses were performed on $Ba_8Ni_3Ge_{43}$ sample revealing the composition of $Ba_{8.0}Ni_{3.1}Ge_{43.3}$ and indicating the sample is phase pure except for trace amount of Ta (Figure 3.9, Table 3.2). The possible source of Ta is the reaction of the melt with the Ta ampoule in the high frequency furnace.

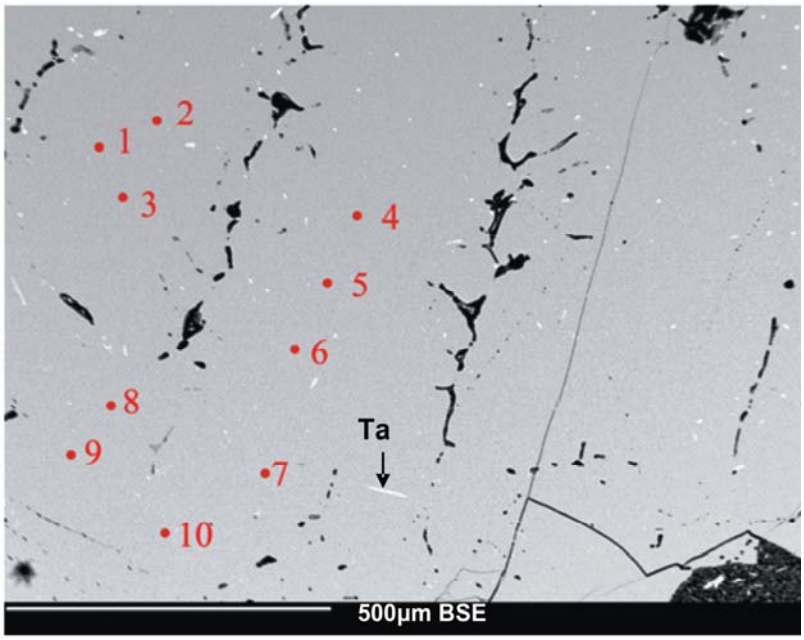

Figure 3.9 Back-scattered electron micrograph of $Ba_8Ni_3Ge_{43}$ with the points in which the measurements were performed. The Ta phase is also marked.

Table 3.2 WDXS quantification result for $Ba_8Ni_3Ge_{43}$ at ten different points on the sample**.**

Average	Weight %	NormWeight %	Atomic %	Dev_Wt
Ba	24.50	24.86	14.73	0.19
Ni	4.01	4.07	5.63	0.02
Ge	70.04	71.07	79.64	0.15
Total	98.54	100.00	100.00	

Figure 3.10 shows the back scattered electron image of $Ba_8Ni_{1.4}Ge_{42.6}$ indicating that Ba_6Ge_{25} is found at the grain boundaries and Ge depositing within the Ba_6Ge_{25} grains. This finding together with other results confirms that Ge clathrates form probably at a peritectic temperature in equilibrium with NiGe, $BaGe_2$, Ba_6Ge_{25}, Ge and melt.

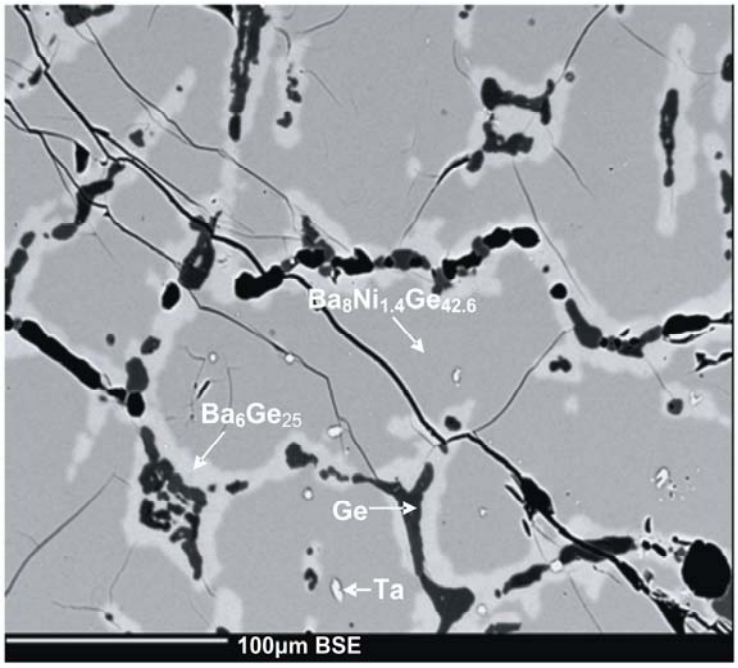

Figure 3.10 Back-scattered electron micrograph for $Ba_8Ni_{1.4}Ge_{42.6}$ together with the results for phase identification.

Clathrate samples containing Pd and Pt with the initial composition 8 : 2 : 44 were found to be in chemical compositions $Ba_{8.0}Pd_{2.5}Ge_{43.5}$ and $Ba_{8.0}Pt_{1.9}\square_{0.5}Ge_{43.6}$ (Tables 3.3-3.4). The EDXS analyses show that the first sample consists of at least three different phases corresponding to Ba_6Ge_{25}, $TaGe_2$ and $Ba_{8.0}Pd_{2.5}Ge_{43.6}$ and the latter contains Ge as secondary phase (Figures 3.11-3.12).

Table 3.3 WDXS quantification result for $Ba_8Pd_{2.5}Ge_{43.5}$ at ten different points on the sample**.**

Average	Weight %	NormWeight %	Atomic %	Dev_Wt
Ba	24.45	24.75	14.80	0.11
Pd	5.85	5.80	4.75	0.04
Ge	70.42	69.92	80.64	0.15
Total	100.71	100.00	100.00	

Table 3.4 WDXS quantification result for $Ba_8Pt_{1.9}\square_{0.5}Ge_{43.6}$ at ten different points on the sample**.**

Average	Weight %	NormWeight %	Atomic %	Dev_Wt
Ba	24.06	23.91	15.06	0.21
Pt	7.75	7.70	3.41	0.21
Ge	68.82	68.39	81.52	0.22
Total	100.71	100.00	100.00	

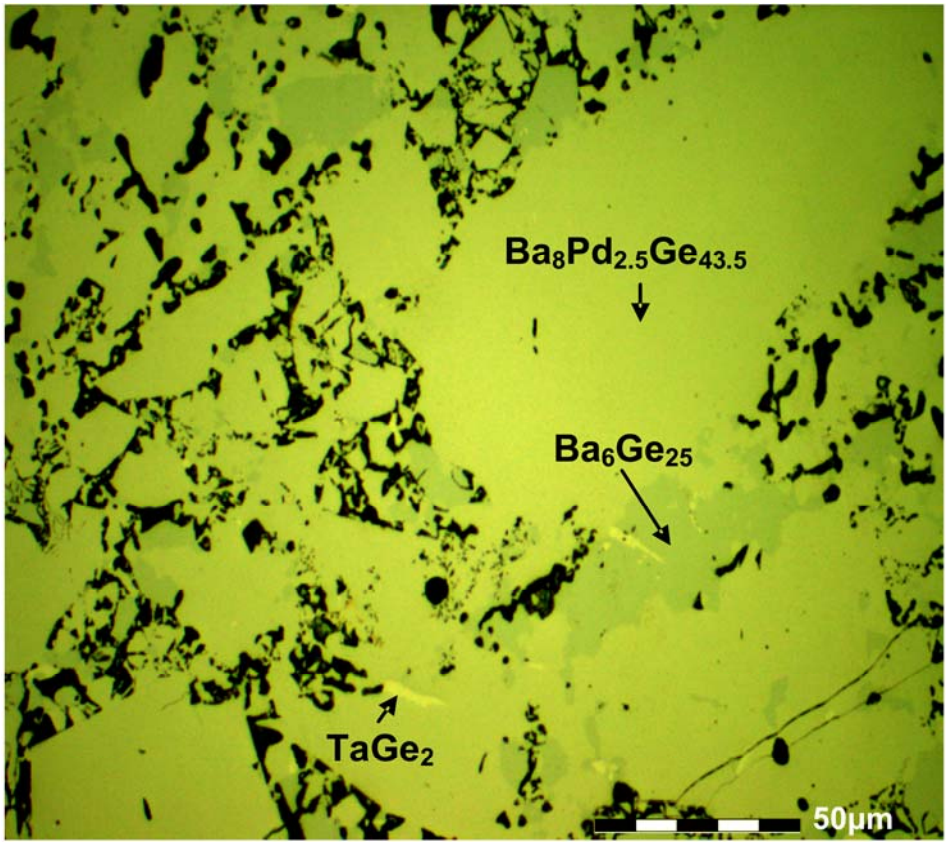

Figure 3.11 Bright-field image of $Ba_8Pd_{2.5}Ge_{43.5}$.

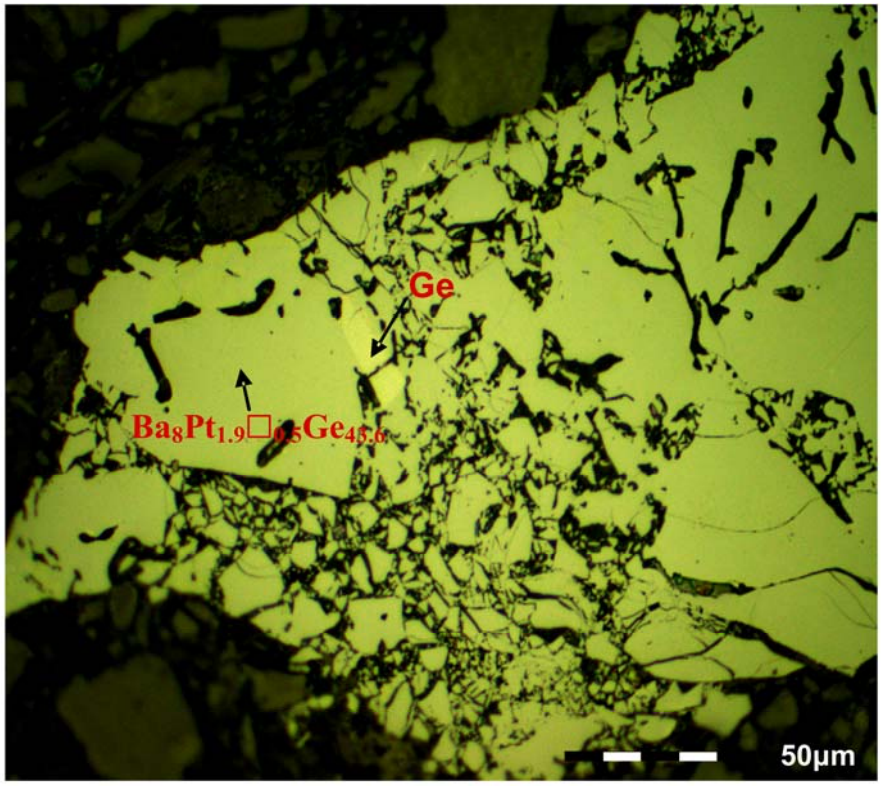

Figure 3.12 Bright-field image of $Ba_8Pt_{1.9}\square_{0.5}Ge_{43.6}$.

For $Ba_8Ni_4Si_{42}$, the stoichiometry was found to be $Ba_8Ni_{3.3}\square_{0.7}Si_{42}$ (Table 3.5). The additional phases are $BaNi_{8.1}Si_{13.6}$, and $NiSi_2$ (Figure 3.13). The same conclusion can be made for the Si clathrates, primarily formed at a peritectic temperature in which the main phase is in equilibrium with the additional phases and the melt.

Table 3.5 WDXS quantification result for Si clathrate at ten different points on the sample**.**

Average	Weight %	NormWeight %	Atomic %	Dev_Wt
Ba	44.22	44.39	14.99	0.16
Ni	7.86	7.89	6.23	0.16
Si	47.53	47.72	78.78	0.21
Total	99.61	100.00	100.00	

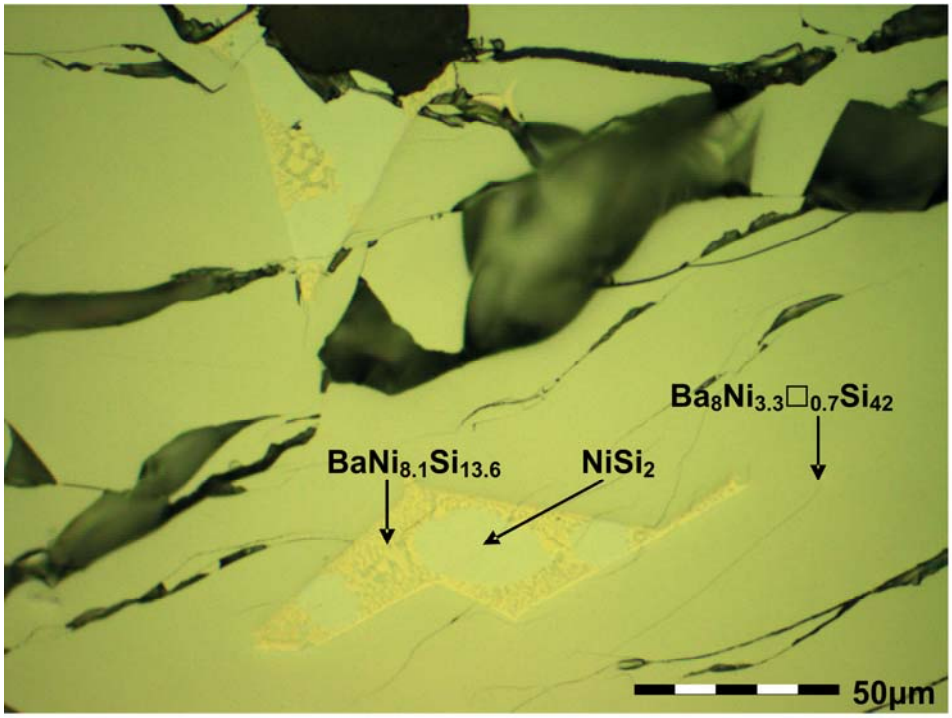

Figure 3.13 Bright-field image of $Ba_8Ni_{3.3}\square_{0.7}Si_{42}$.

Based on the results of the metallographic study, phases with the compositions $Ba_{8.0}Ni_{4.0}Ge_{41.6}$ and $Ba_{8.0}Ni_{3.1}Ge_{43.3}$ are regarded as $Ba_8Ni_4Ge_{42}$ and $Ba_8Ni_3Ge_{43}$, respectively. Hereby, the compositions for $Ba_8(T_x(Ge,Si)_y\square_z)(Ge,Si)_{40}$ (T = Ni, Pd, Pt; □ =

defect) with respect to x+y+z = 6 was preserved within the standard deviations derived from the WDXS results.

Based on the WDXS results, the homogeneity phase range for Ge clathrates with Ni was determined on corresponding Ni-Ge-Void ternary phase diagram as shown in Figure 3.14.

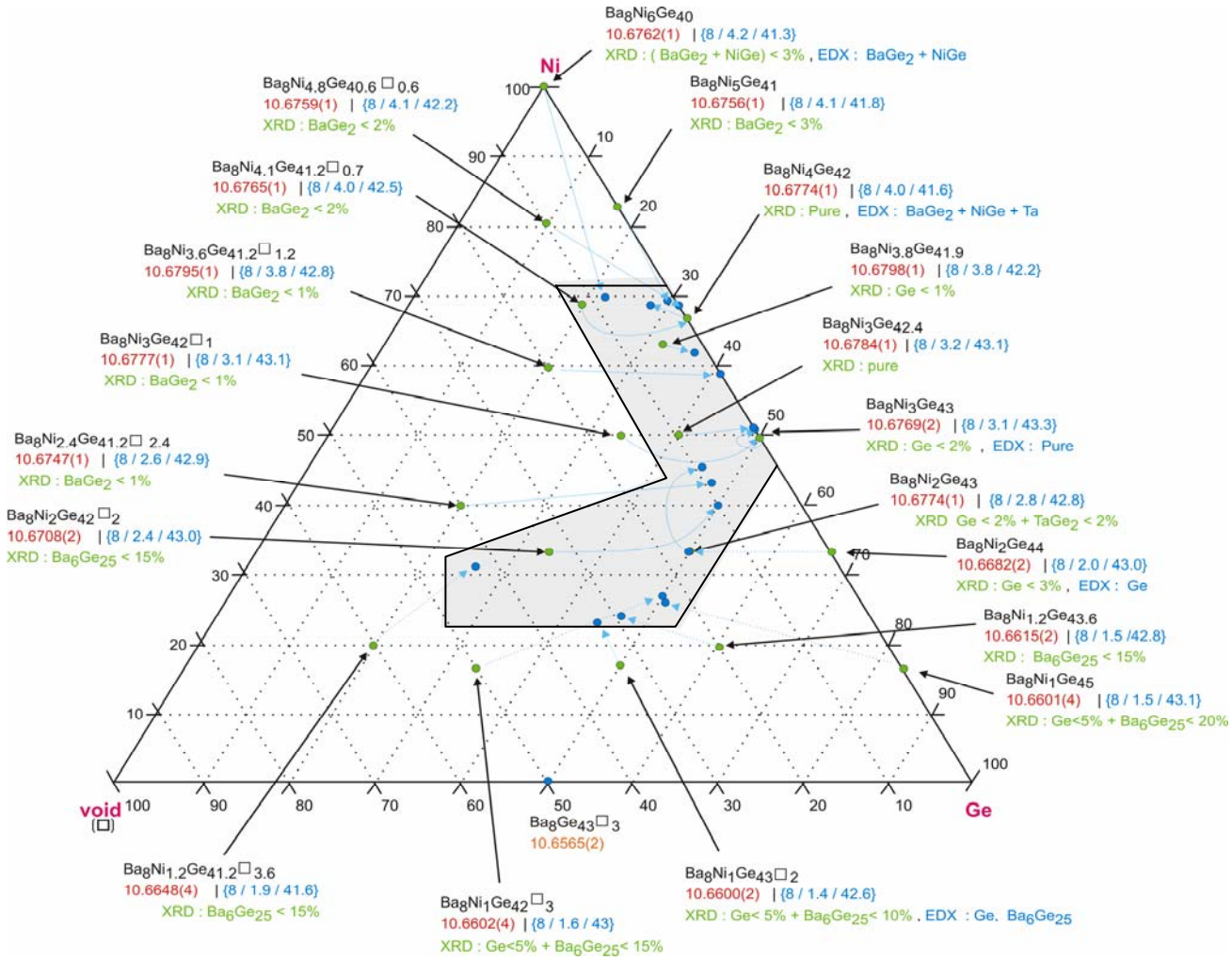

Figure 3.14 Homogeneity phase range is shown with blue region on ternary phase diagram.

The nominal compositions are shown in black. The lattice parameters are given in red. They are refined based on the X-ray powder diffraction result via utilizing WinCSD Cell program and LaB_6 as standard. For each case, the same set of miller indices were used both for clathrate samples and LaB_6 (Table 3.6). The compositions and the additional phases determined via WDXS and EDXS analysis are shown in blue. By-products observed from the X-ray powder diffraction analyses are depicted in green. Finally, green and blue circles represent the nominal compositions and the final composition obtained after heat treatment based on WDXS results.

Table 3.6 Set of Miller indices for lattice parameters refinement.

Common Miller Indices for Clathrates			LaB_6 Miller Indices
h k l	h k l	h k l	
1 1 0	6 1 1	6 5 4	
2 0 0	6 2 0	7 5 2	h k l
2 1 0	5 4 0	8 4 0	1 0 0
2 1 1	6 2 2	9 1 0	1 1 0
3 1 0	6 3 0	7 5 3	1 1 1
2 2 2	6 3 1	8 4 2	2 0 0
3 2 0	4 4 4	6 5 5	2 1 0
3 2 1	6 3 2	6 6 4	2 1 1
4 0 0	7 2 0	8 5 0	2 2 0
4 1 0	6 3 3	7 5 4	3 0 0
3 3 0	7 3 0	9 3 1	3 1 1
4 2 0	6 4 3	7 6 3	2 2 2
4 2 1	6 5 1	8 4 4	3 2 0
3 3 2	8 1 0	7 7 0	3 2 1
4 2 2	8 2 0	8 6 0	4 0 0
4 3 0	8 2 1	7 6 4	4 1 0
4 3 2	6 5 3	10 1 1	
5 2 1	8 2 2	10 2 0	(a = 4.15695 Å)
4 4 0	8 3 0	9 5 0	
5 3 0	7 5 0	10 3 0	Note: 3 1 0 is omitted
5 3 1	7 5 1	7 6 5	due to peak coincidence
6 0 0	6 6 2		with 5 5 4 of clathrate compounds.

The variation of the lattice parameters of Ge clathrate structures with the Ni content is depicted in Fig. 3.15.

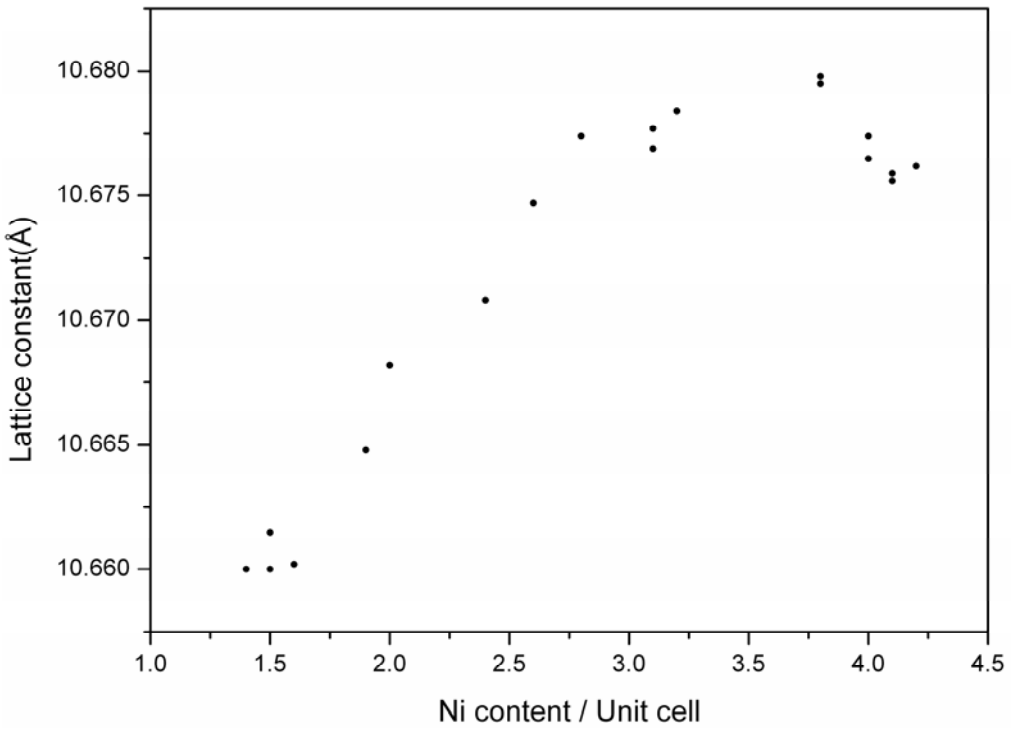

Figure 3.15 Lattice parameters of $Ba_8(Ni_xGe_y\square_z)Ge_{40}$ with respect to Ni content.

The figure shows that the lattice parameters undergo a successive increase whose maximum is reached at a Ni content of 3.8 per unit cell. On further Ni addition, the lattice constant values begin to decrease again. One explanation might be that after a Ni content > 3.8, the occupation of the *6c* position is less favored and Ni atoms preferably center other sites. Unfortunately, the single crystal X-ray data do not allow any detailed analysis, since both Ge and Ni have very similar atomic radii and electronic properties. Further investigations on Pd and Pt compounds may reveal a clearer picture in comparison to Ni case, since the differences in atomic radii and electronic structures between heavier Ni homologues and Ge are expected to be more distinct.

3.3 Crystal Structure Determination

For $Ba_8Pd_{2.5}Ge_{43.5}$, $Ba_8Pt_{1.9}\square_{0.5}Ge_{43.6}$ and $Ba_8Ni_{3.3}\square_{0.7}Si_{42}$, the cubic unit cell parameters were determined from X-ray powder diffraction data as 10.7193(6), 10.7046(4) and 10.2905(2)Å by using WinCSD Cell program and LaB_6 as standard.

The crystal structure determination of $Ba_8Ni_4Ge_{42}$ was performed with low temperature single crystal X-ray diffraction experiment. A suitably sized single crystal was fixed on a glass capillary with grease. The crystal qualities were first checked with the Laue method. After that, single crystal data were collected by the STOE IPDS automatic diffractometer (AgKα radiation, graphite monochromator) equipped with an open nitrogen gas stream as coolant. For $Ba_8Ni_3Ge_{43}$, suitably sized crystals with well-formed edges and faces were picked and mounted properly on top of the sharpened end of a glass capillary by using two-component glue. After checking the crystal quality, the single crystal data were collected at room temperature (RT) on a Rigaku AFC7 four-circle diffractometer equipped with a Mercury-CCD detector (MoKα radiation, graphite monochromator).

In order to determine the quality of the crystal to be measured, diffracted X-rays are recorded on photographic films. Figures 3.16(a) and 3.16(b) show the Weissenberg and Laue photographs of selected crystals confirming perfectly aligned single crystals (producing rings) with sharp and undistorted reflection spots. 3.16 (c) is the single crystal picked for single crystal structure determination of $Ba_8Ni_3Ge_{43}$.

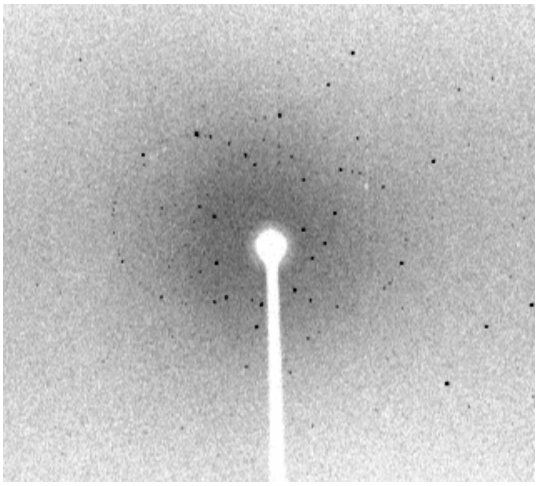

(a)

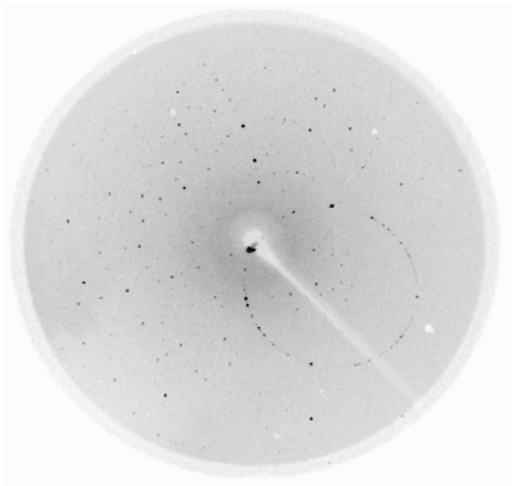

(b)

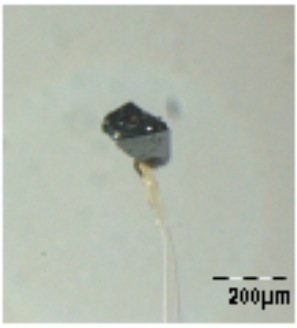

(c)

Figure 3.16 (a) Weissenberg photograph of the single crystal of $Ba_8Ni_4Ge_{42}$ (b) Laue photograph obtained for the single crystal picked from $Ba_8Ni_3Ge_{43}$ shown in (c).

The data were corrected for Lorentz and polarization effects and a multi-scan absorption correction was applied. The crystal structures were solved by direct methods using the program SHELXS-97. Fourier calculations and subsequent full-matrix least-squares refinements were carried out by using SHELXL-97 program.

Complete data collection parameters and details of structure solutions and refinement results of the compounds are given in Tables 3.7 and 3.8.

Table 3.7 Crystallographic data and refinement details for $Ba_8Ni_4Ge_{42}$.

Diffractometer	STOE IPDS diffractometer with graphite monochromator		
X-ray source	AgKα (0.56087Å)		
2θ range [°]	4.2. - 50.00		
Scan type	Φ / ω		
Space Group	$Pm\bar{3}n$ (No. 223)		
Temperature	255K	180K	105K
Cell Parameters			
a=b=c [Å]	10.6653(7)	10.6560(7)	10.6518(7)
α=β=γ [°]	90	90	90
V[Å^3] / Z	1213.16(1) / 1	1209.99(1) / 1	1208.56(1) / 1
Miller-index range	-16 ≤ h ≤ 16	-16 ≤ h ≤ 16	-16 ≤ h ≤ 16
	-14 ≤ k ≤ 16	-14 ≤ k ≤ 16	-14 ≤ k ≤ 16
	-16 ≤ l ≤ 16	-16 ≤ l ≤ 16	-16 ≤ l ≤ 16
No. of measured reflections	14495	14405	14405
Unique data	419	416	416
Observed data ($F_0 > 4\sigma(F_0)$)	308	311	311
Number of parameters refined	17	17	17
R1($F_0 > 4\sigma(F_0)$)	0.0262	0.0258	0.0260
R1(all data)	0.0445	0.0433	0.0454
wR2 ($F_0 > 4\sigma(F_0)$)	0.0350	0.0389	0.0407
wR2 (all data)	0.0367	0.0410	0.0442
Goof (for F^2)	1.018	0.981	1.035

Table 3.8 Crystallographic data and refinement results of $Ba_8Ni_3Ge_{43}$.

Compound	$Ba_8Ni_3Ge_{43}$
Space Group	$Pm\bar{3}n$ (No. 223)
Cell Parameters	
a=b=c [Å]	10.6778(4)
α=β=γ [°]	90
V[Å^3] / Z	1217.43 (8) / 1
Diffractometer	Rigaku AFC7 CCD with graphite monochromator
X-ray source	MoKα (0.71070Å)
2θ range [°]	5.40 - 61.79
Scan type	Φ / ω
Miller-index range	$-14 \leq h \leq 14$
	$-15 \leq k \leq 15$
	$-12 \leq l \leq 15$
No. of measured reflections	9695
Unique data	377
Observed data ($F_0 > 4\sigma(F_0)$)	376
Number of parameters refined	19
R1 ($F_0 > 4\sigma(F_0)$)	0.0356
R1 (all data)	0.0358
wR2 ($F_0 > 4\sigma(F_0)$)	0.0746
wR2 (all data)	0.0749
Goof (for F^2)	1.225

No superstructure reflections were observed from the close investigations of both single crystal and powder XRD experiments. The observed Laue symmetry and systematic extinctions were indicative of the space group of $Pm\bar{3}n$ (No. 223) for all crystals. This space group was then tried for refinements and the statistically better solutions were chosen on the basis of *R* values and number of other variables. The initial positions of all atoms were obtained from direct methods. Once all atoms were assigned, the occupancies of atoms at 2a, 6d and 16i were fixed with full occupancy while the occupancies for the 6c

position were set according to WDXS results. For the latter case, it is assumed that the atoms occupy 6c site randomly. The occupancy factor for Ge in 24k site is fixed with full occupancy for $Ba_8Ni_4Ge_{42}$ since the applied split model did not bring any significant improvement in terms of anisotropy. For the $Ba_8Ni_3Ge_{43}$ case which shows also high anisotropy a split model was introduced. For split atoms, the thermal parameters (atomic displacement parameters) were constrained to the same value. Atomic coordinates, equivalent isotropic displacement parameters and anisotropic displacement parameters are given in the subsequent tables (3.9-3.16). Estimated standard deviations (e.s.d) are given in parenthesis.

Table 3.9 Atomic coordinates, equivalent isotropic displacement parameters ($Å^2$) and occupancies for $Ba_8Ni_4Ge_{42}$ at 255 K.

Atom	Site	x	y	z	Ueq	Occ. (%)
Ba1	2a	0.00000	0.00000	0.00000	0.00977(19)	1
Ba2	6d	0.25000	0.50000	0.00000	0.03892(29)	1
Ni1	6c	0.50000	0.25000	0.00000	0.00907(26)	0.6667
Ge1	6c	0.50000	0.25000	0.00000	0.00907(26)	0.3333
Ge2	16i	0.18357(3)	0.18357(3)	0.18357(3)	0.00800(12)	1
Ge3	24k	0.31653(6)	0.12203(6)	0.00000	0.01341(14)	1

Table 3.10 Anisotropic displacement parameters (Uij x 10^4 ($Å^2$)) for $Ba_8Ni_4Ge_{42}$ at 255 K.

Atom	U11	U22	U33	U12	U13	U23
Ba1	98 (2)	98 (2)	98 (2)	0	0	0
Ba2	186 (5)	491 (4)	491 (4)	0	0	0
Ni1,Ge1	82 (4)	109 (6)	82 (4)	0	0	0
Ge2	80 (1)	80 (1)	80 (1)	-10 (1)	-10 (1)	-10 (1)
Ge3	119 (3)	199 (3)	84 (3)	67 (3)	0	0

Table 3.11 Atomic coordinates, equivalent isotropic displacement parameters ($Å^2$) and occupancies for $Ba_8Ni_4Ge_{42}$ at 180 K.

Atom	Site	x	y	z	Ueq	Occ. (%)
Ba1	2a	0.00000	0.00000	0.00000	0.00743(20)	1
Ba2	6d	0.25000	0.50000	0.00000	0.03513(27)	1
Ni1	6c	0.50000	0.25000	0.00000	0.00705(25)	0.6667
Ge1	6c	0.50000	0.25000	0.00000	0.00705(25)	0.3333
Ge2	16i	0.18359(3)	0.18359(3)	0.18359(3)	0.00603(13)	1
Ge3	24k	0.31656(6)	0.12200(6)	0.00000	0.01139(14)	1

Table 3.12 Anisotropic displacement parameters (Uij x 10^4 ($Å^2$)) for $Ba_8Ni_4Ge_{42}$ at 180 K.

Atom	U11	U22	U33	U12	U13	U23
Ba1	74 (2)	74 (2)	74 (2)	0	0	0
Ba2	154 (5)	450 (4)	450 (4)	0	0	0
Ni1,Ge1	63 (4)	85 (6)	63 (4)	0	0	0
Ge2	60 (1)	60 (1)	60 (1)	-10 (1)	-10 (1)	-10 (1)
Ge3	103 (3)	176 (3)	63 (3)	68 (3)	0	0

Table 3.13 Atomic coordinates, equivalent isotropic displacement parameters ($Å^2$) and occupancies for $Ba_8Ni_4Ge_{42}$ at 105 K.

Atom	Site	x	y	z	Ueq	Occ. (%)
Ba1	2a	0.00000	0.00000	0.00000	0.00556(21)	1
Ba2	6d	0.25000	0.50000	0.00000	0.03168(29)	1
Ni1	6c	0.50000	0.25000	0.00000	0.00573(27)	0.6667
Ge1	6c	0.50000	0.25000	0.00000	0.00573(27)	0.3333
Ge2	16i	0.18353(3)	0.18353(3)	0.18353(3)	0.00450(14)	1
Ge3	24k	0.31661(6)	0.12191(7)	0.00000	0.00991(15)	1

Table 3.14 Anisotropic displacement parameters (Uij x 10^4 ($Å^2$)) for $Ba_8Ni_4Ge_{42}$ at 105 K.

Atom	U11	U22	U33	U12	U13	U23
Ba1	56 (2)	56 (2)	56 (2)	0	0	0
Ba2	126 (5)	412 (4)	412 (4)	0	0	0
Ni1,Ge1	53 (4)	65 (7)	53 (4)	0	0	0
Ge2	45 (1)	45 (1)	45 (1)	-7 (1)	-7 (1)	-7 (1)
Ge3	89 (3)	162 (3)	47 (3)	68 (3)	0	0

Table 3.15 Atomic coordinates, equivalent isotropic displacement parameters ($Å^2$) and occupancies for $Ba_8Ni_3Ge_{43}$.

Atom	Site	x	y	z	Ueq	Occ. (%)
Ba1	2a	0.00000	0.00000	0.00000	0.01125(34)	1
Ba2	6d	0.25000	0.50000	0.00000	0.04041(41)	1
Ni1	6c	0.50000	0.25000	0.00000	0.01634(42)	0.5
Ge1	6c	0.50000	0.25000	0.00000	0.01634(42)	0.5
Ge2	16i	0.18368(5)	0.18368(5)	0.18368(5)	0.01043(26)	1
Ge31	24k	0.30867(32)	0.11907(73)	0.00000	0.01246(63)	0.6415
Ge32	24k	0.33247(79)	0.12704(144)	0.00000	0.01246(63)	0.3585

Table 3.16 Anisotropic displacement parameters (Uij x 10^4 ($Å^2$)) for $Ba_8Ni_3Ge_{43}$.

Atom	U11	U22	U33	U12	U13	U23
Ba1	113 (3)	113 (3)	113 (3)	0	0	0
Ba2	203 (5)	505 (6)	505 (6)	0	0	0
Ni1	153 (5)	185 (9)	153 (5)	0	0	0
Ge1	153 (5)	185 (9)	153 (5)	0	0	0
Ge2	104 (3)	104 (3)	104 (3)	-16 (2)	-16 (2)	-16 (2)
Ge31	38 (17)	225 (11)	111 (4)	34 (15)	0	0
Ge32	38 (17)	225 (11)	111 (4)	34 (15)	0	0

Atomic displacement parameters (ADPs) measure the mean-square displacement amplitudes of an atom about its equilibrium position in a crystal. Typically ADPs are reported as 3x3 matrixes, Uij, that allows for anisotropic displacements. The nature of the framework and the atomic displacement parameters (ADPs) of atoms play important roles in the properties of clathrates. Especially, dynamic disorder associated with the alkaline earth metals inside the polyhedra can lead to low thermal conductivities. The very basic reason is that the atoms in cages can 'rattle' inside the polyhedra and produce low-frequency anharmonic phonon modes, which scatter the heat-carrying acoustic phonons. Figures 3.17–3.20 show the temperature dependence of the anisotropic (Uii) and isotropic (Ueq) ADPs that were obtained from single crystal diffraction measurement on $Ba_8Ni_4Ge_{42}$ (with error bars).

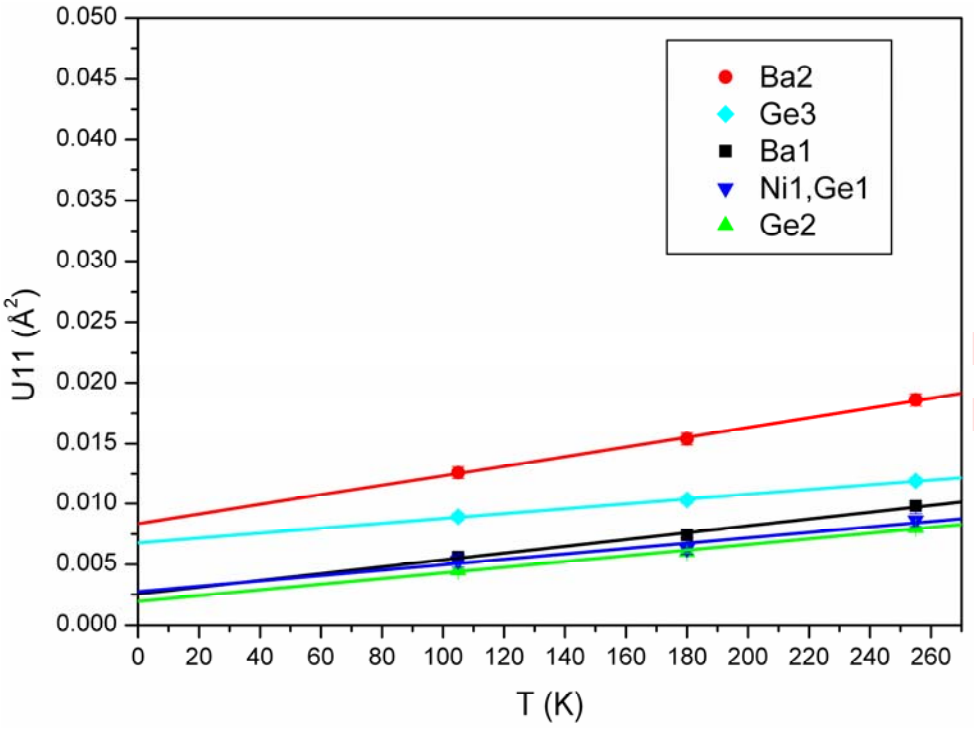

Figure 3.17 Temperature dependence of U11 for $Ba_8Ni_4Ge_{42}$.

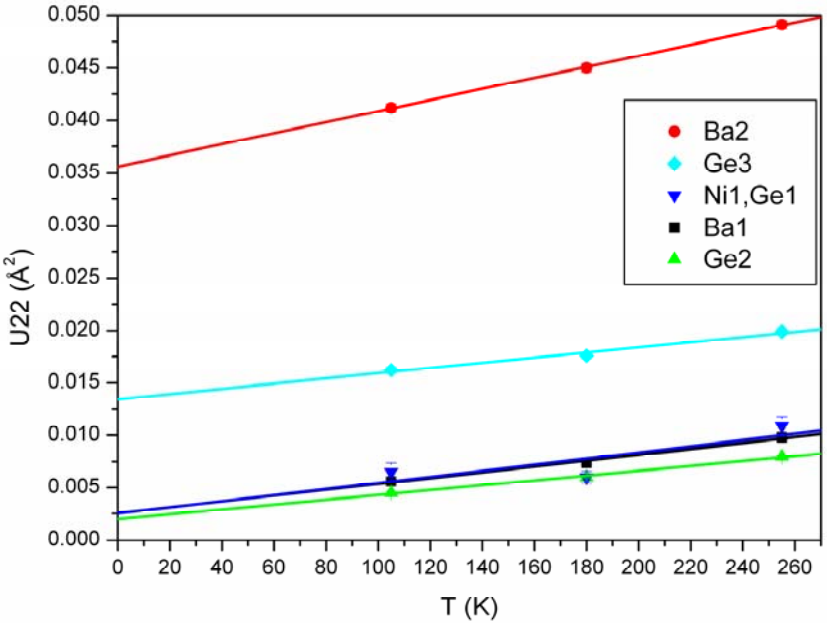

Figure 3.18 Temperature dependence of U22 for $Ba_8Ni_4Ge_{42}$.

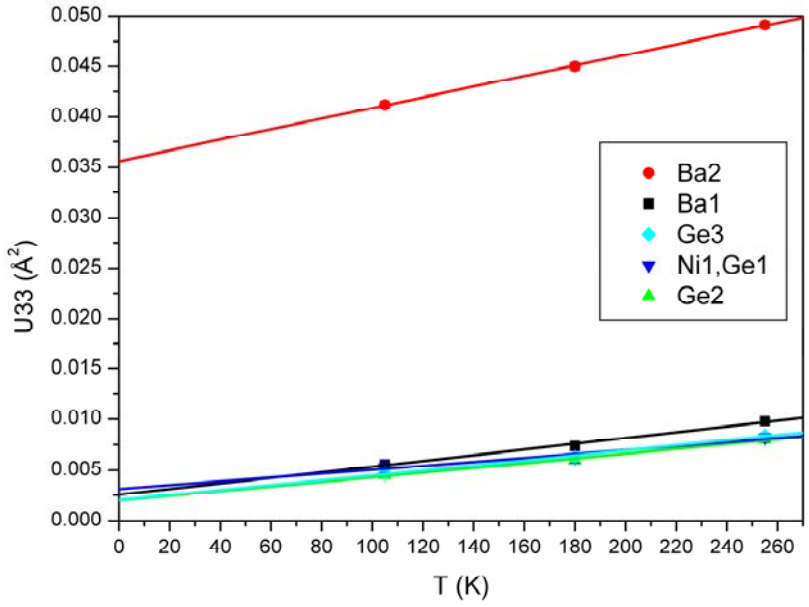

Figure 3.19 Temperature dependence of U33 for $Ba_8Ni_4Ge_{42}$.

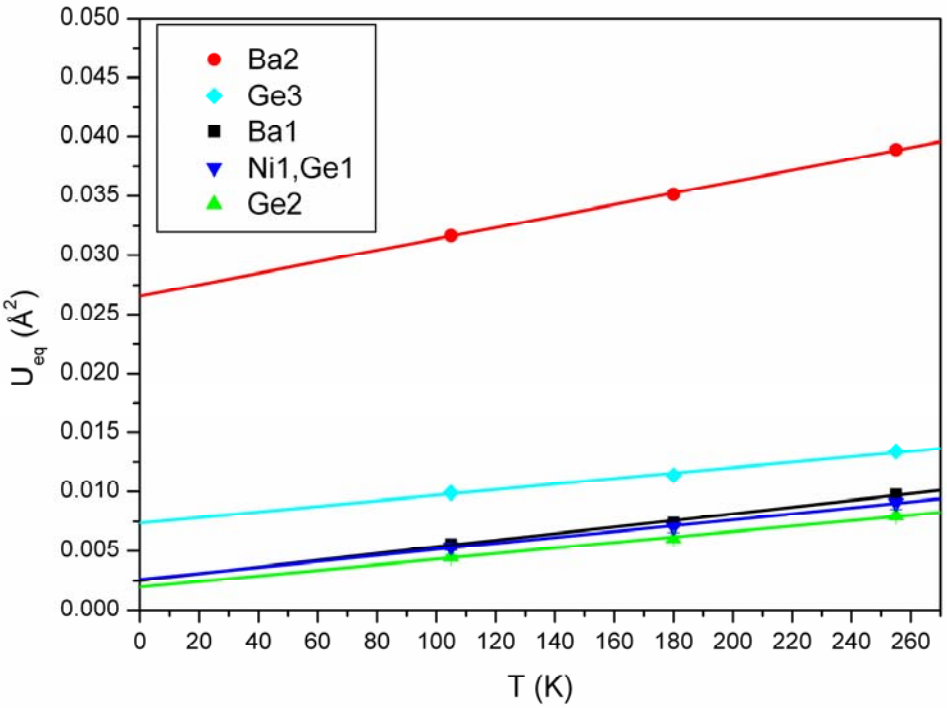

Figure 3.20 Temperature dependence of Ueq for $Ba_8Ni_4Ge_{42}$.

The ADPs for the framework atoms in these figures display a weak temperature dependence indicating that the framework is relatively stiff. However, the ADPs for Ba2 show strong temperature dependence with ordinate intercept greater than the others in all cases when extrapolated to 0 K. The temperature dependence of the ADPs can be considered as an indication of the degree of dynamic or rattling disorder. Very large ADPs for Ba2 in tetrakaidecahedron indicate an increase of the amplitude for the atom's rattling as the size of the cage framework becomes larger.

For clathrate compounds, in which one of the atoms is poorly bonded and rattling in an oversized cage, the simplest model for the "rattler" is that of a harmonic oscillator which is also called Einstein oscillator. In this model it is assumed that all of the rattlers vibrate

independently from each other at the same frequency. The remaining atoms, forming the framework are considered within the Debye model. In this picture, the entire structure is composed of an Einstein mode in a Debye host solid in which the Einstein mode interact with the acoustic phonons of the Debye host. It has been previously shown that isotropic ADPs can be used to determine the Einstein temperature and localized vibration frequencies for the rattler and the Debye temperature for the cage framework as

$$U_{eq} = = \frac{h^2 T}{4\pi^2 m k_B \theta_E{}^2} = \frac{3\, h^2 T}{4\pi^2 m k_B \theta_D{}^2} \tag{3.1}$$

$$\theta_E = \frac{hf}{k_B} \tag{3.2}$$

where U_{eq} is the isotropic mean-square displacement, k_B is Boltzmann's constant, *m* is the mass of the atoms and f is the frequency of vibration [101]. Given the Debye temperature, the average velocity of sound can be found as,

$$v_s = \frac{\theta_D k_B 2\pi/h}{(6\pi^2 N_V)^{1/3}} \tag{3.3}$$

where N_v is the number of atoms per unit volume.

Taking the slope of the Ueq data for Ba2 (4.8267×10^{-5} Å^{2}K^{-1}) results in an Einstein temperature of 86 K and a localized vibration frequency of 17.92×10^{11} s^{-1}. The Debye temperature was calculated as 295 K with average of the slopes (2.3504×10^{-5} Å^{2}K^{-1}) and average mass per atom (71.4 amu) for the cage framework. The velocity of sound was calculated as 2795 and 2798 ms^{-1} for 255 K and at room temperature, respectively. For room temperature calculation the lattice parameter of 10.6774 Å was used which was

refined from X-ray powder diffraction data. The results are similar to another type I clathrate compound $Sr_8Ga_{16}Ge_{30}$ with 85 K(θ_E), 271 K(θ_D), and 2600 ms^{-1}(v_s) values.

3.4 Crystal Structure Description

The investigated clathrate compounds crystallize in the cubic space group $Pm\bar{3}n$ (No: 223). The crystal structure is characterized by polyhedral cages formed by E10 (Ni, Pd, Pt) and E14(Ge, Si) and guest atoms, Ba, centering the polyhedra. The unit cell contains two types of cages: two 20-atom pentagonal dodecahedra and six 24-atom tetrakaidecahedra both encapsulating guest atoms as shown in Figure 3.21.

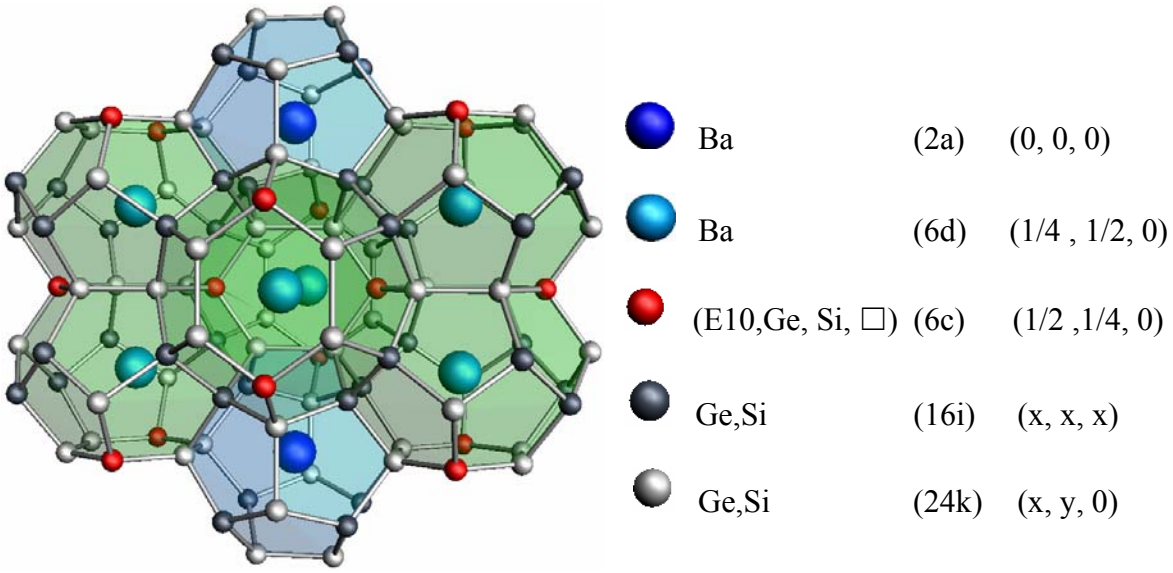

Figure 3.21 Polyhedral structure of the clathrate-I unit cell.

While the pentagonal dodecahedron is formed by 12 pentagonal faces, the tetrakaidecahedron is built up by 12 pentagonal and 2 hexagonal faces (Figure 3.22).

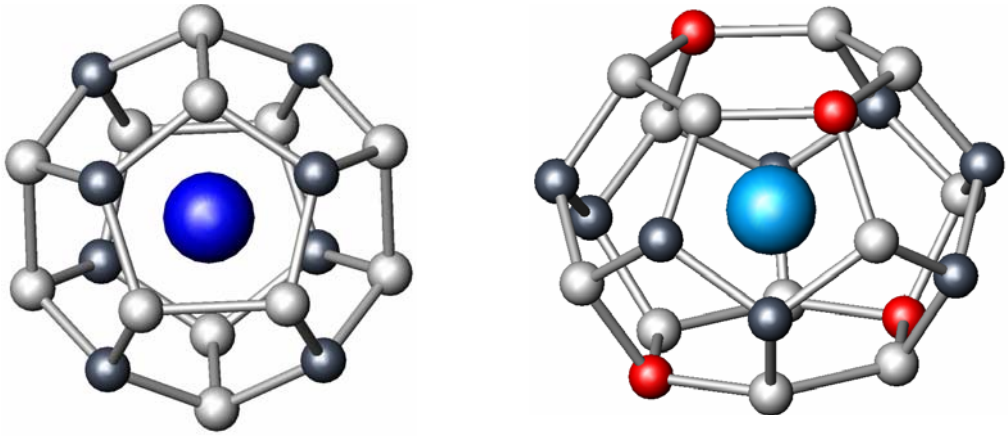

(a) **(b)**

Figure 3.22 Building units of the clathrate-I structure: **(a)** the 20-atom pentagonal dodecahedron (12 pentagonal faces) and **(b)** the 24-atom tetrakaidecahedra (12 pentagonal and 2 hexagonal faces)

In the structure, 20-atom polyhedra are linked via six interstitial 6c-positions, enabling the formation of 24-atom polyhedra. In this sense, 20 and 24 atom polyhedra share planes with each other building up a tetrahedrally coordinated covalent framework. The local bonding in the framework of the clathrate lattices is similar to that in the diamond structure. However, these lattices contain pentagonal rings which make their topology quite different from that in the diamond lattice. Another feature of this structure is that the tetrakaidekahedra form three mutually perpendicular channels by sharing hexagonal faces. These three pairs of channels enclose the 20-atom polyhedra and separate them from each other (Figure 3.23).

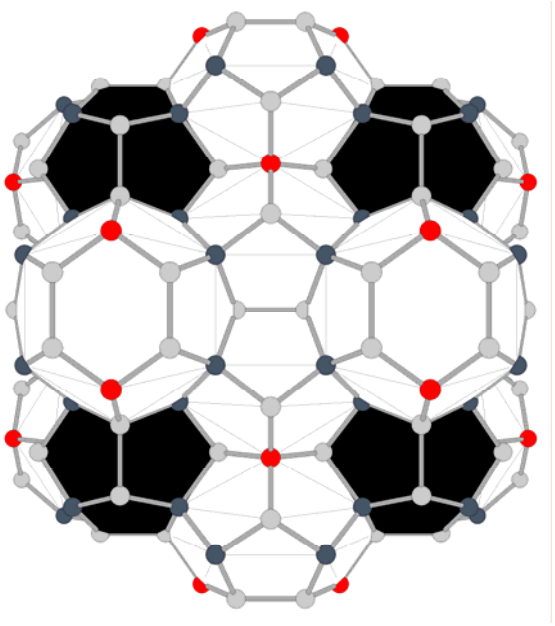

Figure 3.23 The black polyhedra are the pentagonal dodecahedra enclosed between the three mutually perpendicular channels of tetrakaidecahedra (white) sharing their hexagonal faces.

The atoms forming the cage framework are located in 6c, 16i and 24k sites, whereas guest atoms center the 2a and 6d sites. Vacancies found in the type-I clathrate compounds preferentially occupy the 6c sites that can be substituted by transition metals. For the possible positions of transition metals and vacancies, the model where the 6c sites are occupied by them and E14 atoms is random. In the structure, 6c sites occupy two out of six vertices of each hexagonal faces of tetrakaidecahedra. They are bonded to four framework atoms of the site symmetry 24k. The 24k sites belong to both the smaller and larger cages, and an atom at this site is bonded to one 6c atom, one 24k atom and two 16i atoms. The 16i atoms are found only on the pentagonal faces. All the bonds they form are almost perfectly tetrahedral and they bond to another 16i atom and three 24k atoms. Since the 24k and 6c sites build the hexagonal phases, some of their angles are not perfectly tetrahedral. Angle within the hexagonal phase could be larger than 120° for the 24k sites and 110° for 6c sites.

The values of selected interatomic distances and angles for $Ba_8Ni_4Ge_{42}$ are given together with estimated standard deviations in Tables 3.17 and 3.18.

Table 3.17 Selected interatomic distances for $Ba_8Ni_4Ge_{42}$.

Atoms		Distances [Å]		
		255 K	180K	105K
Ba1-	Ge2	3.3910 (6)	3.3885 (6)	3.3870 (7)
	Ge3	3.6181 (7)	3.6151 (7)	3.6139 (8)
Ba2-	Ge3	3.5542 (5)	3.5508 (5)	3.5487 (5)
	Ni1(Ge1)	3.7708 (3)	3.7675 (2)	3.7660 (2)
Ni1(Ge1)-	Ge3	2.3857 (7)	2.3836 (7)	2.3827 (7)
	Ba2	3.7708 (2)	3.7675 (2)	3.7660 (2)
Ge2-	Ge2	2.4544 (11)	2.4514 (12)	2.4507 (13)
	Ge3	2.5049 (4)	2.5031 (4)	2.5027 (5)
	Ba1	3.3910 (6)	3.3885 (6)	3.3870 (7)
Ge3-	Ni1(Ge1)	2.3857 (7)	2.3836 (7)	2.3827 (7)
	Ge2	2.5049 (4)	2.5031 (4)	2.5027 (5)
	Ge3	2.6029 (13)	2.6001 (13)	2.5971 (14)
	Ba2	3.5542 (5)	3.5508 (5)	3.5487 (5)
	Ba1	3.6181 (7)	3.6151 (7)	3.6139 (8)

Table 3.18 Selected interatomic angles for $Ba_8Ni_4Ge_{42}$.

Atoms	Bond Angle [°]		
	255K	180K	105K
Ge3 – Ni1(Ge1) – Ge3	109.10 (1)	109.11 (1)	109.14 (2)
Ge3 – Ni1(Ge1) – Ge3	110.21 (3)	110.19 (3)	110.13 (3)
Ge3 – Ge2 – Ge2	106.00 (2)	106.01 (2)	106.01 (2)
Ge3 – Ge2 – Ge3	112.71 (2)	112.70 (2)	112.70 (2)
Ge2 – Ge3 – Ni1(Ge1)	108.33 (2)	108.31 (2)	108.29 (3)
Ge2 – Ge3 – Ge2	102.81 (3)	102.81 (3)	102.77 (3)
Ge3 – Ge3 – Ni1(Ge1)	124.90 (1)	124.91 (1)	124.93 (2)
Ge3 – Ge3 – Ge2	105.19 (2)	105.20 (2)	105.22 (2)

In $Ba_8Ni_4Ge_{42}$ (255 K), Ge-Ge interatomic distances (d(Ge-Ge)) vary between 2.4544(11) and 2.6029(13) Å which are a slightly larger than that of pure Ge (2.445) Å [10]. Similar results were obtained also by Carrillo et al. for Ba_8Ge_{43} with 3 ordered voids in which the bond lengths are in the range of 2.441(1)-2.611(1) Å [34]. The maximum bond length (2.6029Å) is observed to be between Ge3 atoms, which are close to the vacancies if present. The distance of 2.3857Å between Ni1(Ge1) and Ge3 is very close to the Ni-Ge bond length in the binary NiGe compound changing between 2.329 and 2.399 Å [102]. The interatomic distances between Ba2 and its surrounding cage atoms in tetrakaidekahedra (3.5542(5) and 3.7708(3) Å) are generally larger than that of Ba1 and its surrounding cage atoms in pentagonal dodecahedron (3.3910(6)-3.6181(7) Å). This reveals that the bond strength between Ba2 atoms and its surrounding cage atoms in tetrakaidekahedra are weaker than that of Ba1 and pentagonal dodecahedra. Correspondingly the Ba2 atoms vibrate more significantly than Ba1 atoms which can be

deducted also from the value of atomic displacement parameters. Almost all angles within the Ge(Ni) framework are close to tetrahedral angles. Ge3-Ge3-Ni(Ge) bond angle is 124.90°. With a temperature decrease, the bond angles remain almost constant but the bond lengths become shorter due to the decrease of the thermal vibrations of the atoms.

The values of selected interatomic distances and angles for $Ba_8Ni_3Ge_{43}$ are given together with estimated standard deviations in Tables 3.19 and 3.20.

Table 3.19 Selected interatomic distances for $Ba_8Ni_3Ge_{43}$.

Atoms		Distances [Å]
Ba1-	Ge2	3.3971 (9)
	Ge32	3.5327 (34)
Ba2-	Ge32	3.4880 (81)
	Ge31	3.5939 (39)
Ni1(Ge1)-	Ge32	2.219 (10)
	Ge31	2.4755 (43)
	Ba2	3.7752 (1)
Ge2-	Ge2	2.4530 (19)
	Ge31	2.4706 (33)
	Ge32	2.5955 (69)
	Ba1	3.3971 (9)
Ge31-	Ge2	2.4706 (33)
	Ni1(Ge1)	2.4755 (43)
	Ba1	3.5327 (34)
	Ba2	3.5939 (39)
Ge32-	Ni1(Ge1)	2.210 (10)
	Ge2	2.5955 (69)
	Ge31	2.6402 (77)
	Ge32	2.713 (11)
	Ba2	3.4880 (81)
	Ba1	3.8004 (85)

Table 3.20 Selected interatomic angles for $Ba_8Ni_3Ge_{43}$.

Atoms	Bond Angle [°]
Ge31 – Ni1 – Ge31	108.60 (17)
Ge31 – Ni1 – Ge31	111.23 (34)
Ge31 – Ni1 – Ge32	109.52 (9)
Ge32 – Ni1 – Ge32	109.34 (21)
Ge32 – Ni1 – Ge32	110.49 (38)
Ge32 – Ni1 – Ge32	107.45 (74)
Ge31 – Ge2 – Ge2	107.92 (9)
Ge32 – Ge2 – Ge2	102.56 (20)
Ge31 – Ge2 – Ge31	110.98 (9)
Ge32 – Ge2 – Ge31	113.21 (44)
Ge32 – Ge2 – Ge31	113.63 (38)
Ge2 – Ge31 – Ni1(Ge1)	106.74 (20)
Ge2 – Ge31 – Ge2	105.10 (20)
Ge31– Ge31 – Ni1(Ge1)	124.38 (17)
Ge32– Ge31 – Ni1(Ge1)	118.86 (38)
Ge31– Ge31 – Ge2	106.22 (17)
Ge32– Ge31 – Ge2	109.27 (18)
Ge2 – Ge32 – Ni1(Ge1)	110.83 (42)
Ge32 – Ge32 – Ni1(Ge1)	126.28 (37)
Ge2 – Ge32 – Ge2	98.17 (35)
Ge2 – Ge32 – Ge31	99.76 (33)
Ge2 – Ge32 – Ge32	103.47(32)

In the $Ba_8Ni_3Ge_{43}$ case, the splitting of the Ge3 site caused significant changes in terms of bond lengths and bond angles. The Ge-Ge bond lengths vary between 2.453(2) and 2.713(11) Å which are slightly larger than the bond lengths between the same atoms in $Ba_8Ni_4Ge_{42}$ and in elemental germanium. The maximum bond length is observed between

Ge32 atoms with d(Ge-Ge) = 2.713 Å. The distance of 2.219 Å is less than the bond lengths d(Ni-Ge) reported for NiGe (2.329 - 2.399 Å) [102], because of the split model. The interatomic distances between Ba1 and Ge atoms are in the range of 3.3971(9)-3.5327(34) Å. For the Ba2 and Ge case, they vary between 3.4880(5) and 3.5939(3) Å. Almost all angles within the Ge(Ni) framework are close to tetrahedral angles. The bond angles between splitted Ge and Ge(Ni) atoms are greater than 120 ° (124.38 -126.28 °).

3.5 Thermal Analysis

Thermal investigations of the compounds were carried out with NETZSCH DSC 404 C instrument inside the glove-box. All measurements were performed by applying a heating / cooling rate of 10 °C /min. The samples were ground in an agate mortar followed by sealing 50 mg of sample in Nb crucible. Once the final temperature of the heating cycle was reached, the cooling was immediately started without further preservation time at that temperature. DSC curve of $Ba_8Ni_4Ge_{42}$ and $Ba_8Ni_3Ge_{43}$ show one endothermic peaks at 836 and 843 °C, respectively. Two prominent exothermic peaks are observed for both compositions at 801-802.1 °C and 758-755 °C (Figures 3.24-3.25). The endothermic peak originates from the decomposition of the clathrate and the exothermic peaks represent the crystallization from the melt. Investigations on other samples show the decomposition temperature range of the clathrates with Ni changes between 835 and 845 °C.

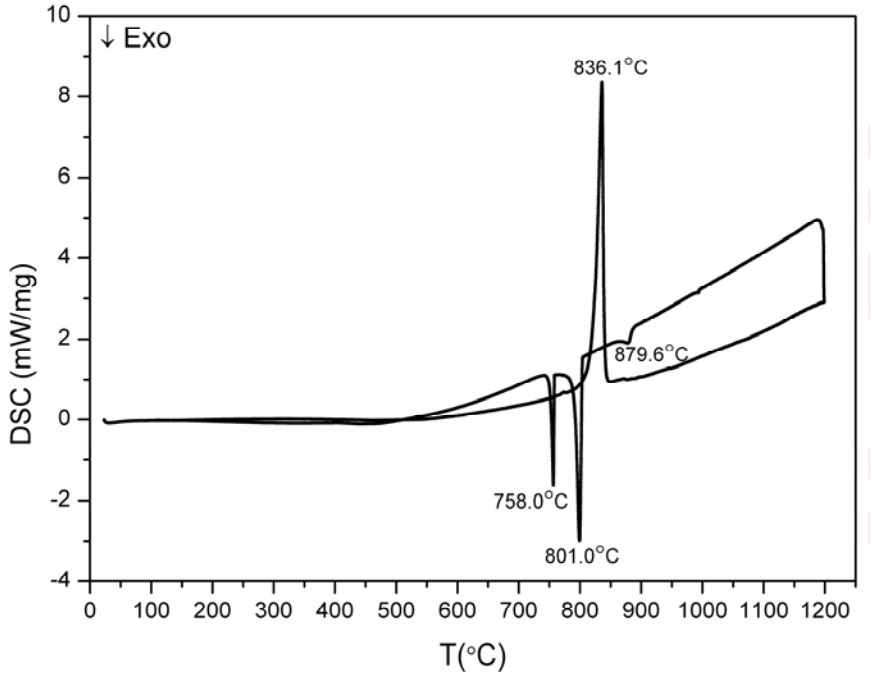

Figure 3.24 The DSC curve of $Ba_8Ni_4Ge_{42}$ heated up to 1200°C.

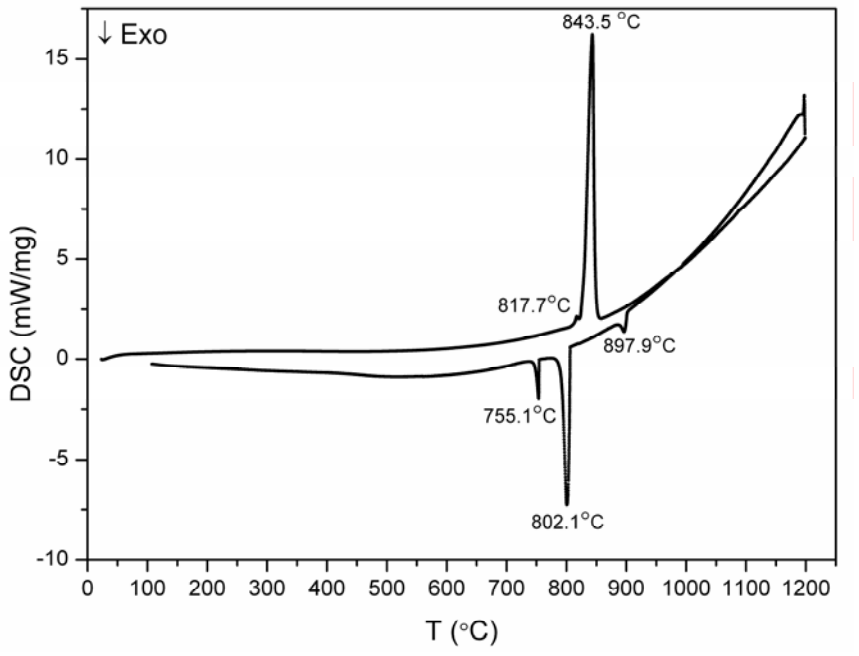

Figure 3.25 The DSC curve of $Ba_8Ni_3Ge_{43}$ heated up to 1200°C.

After DSC investigation, $Ba_8Ni_4Ge_{42}$ was measured by X-ray powder diffraction analysis and identified as both clathrate and $BaGe_2$ (Figure 3.26).

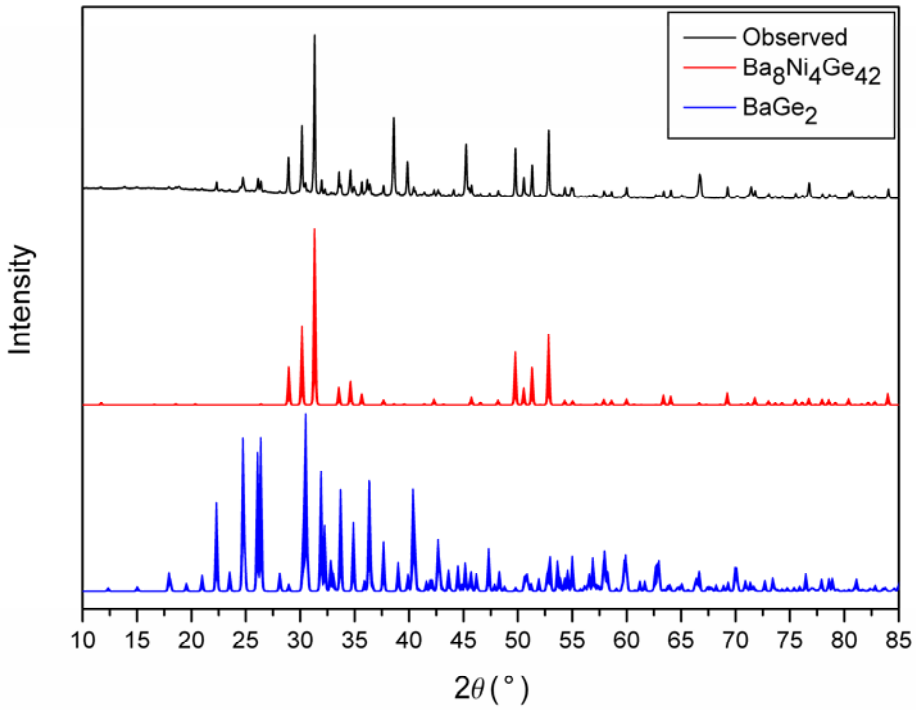

Figure 3.26 X-ray powder diffraction pattern of $Ba_8Ni_4Ge_{42}$ after heating up to 1200 °C.

The same peaks are observed for the samples with Pd and Pt at slightly different temperatures (Figures 3.27-3.28).

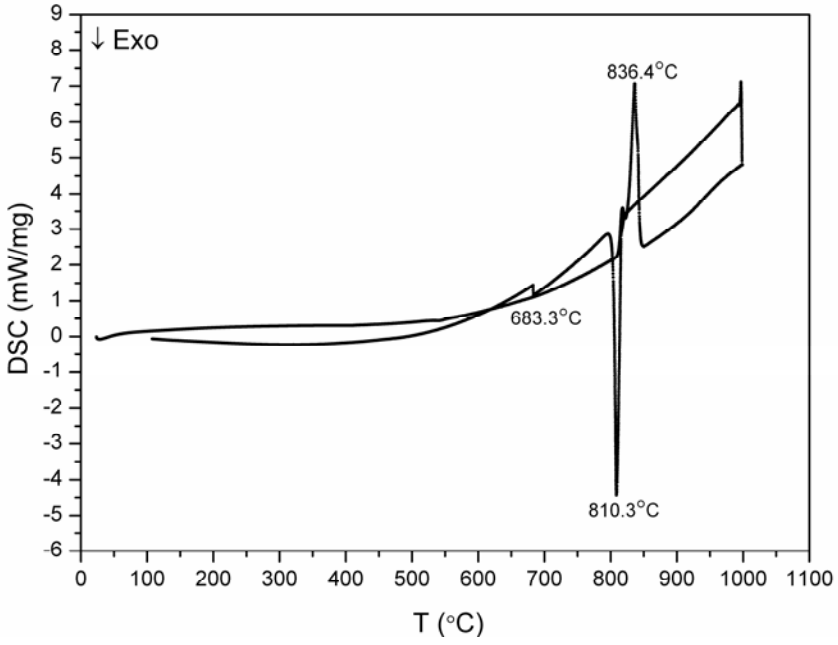

Figure 3.27 The DSC curve of $Ba_8Pd_{2.5}Ge_{43.5}$ heated up to 1000 °C.

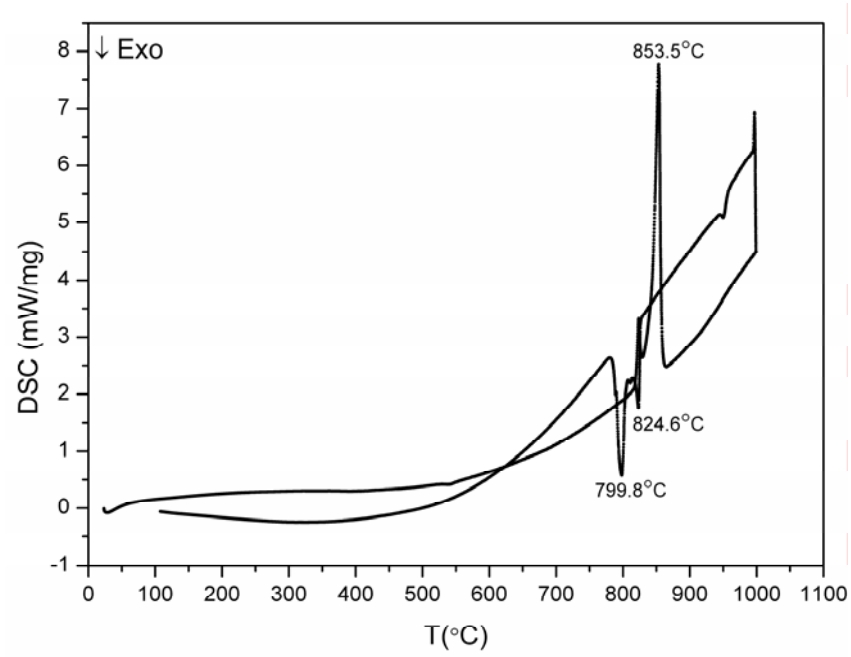

Figure 3.28 The DSC curve of $Ba_8Pt_{1.9}\square_{0.5}Ge_{43.6}$ heated up to 1000 °C.

Figure 3.29 shows that the clathrate sample with Si is stable until 1105 °C. This high decomposition temperature is mainly due to the electronegativity and size differences between Ni and Si atoms resulting in more ionic character and hence forming rigid cage framework.

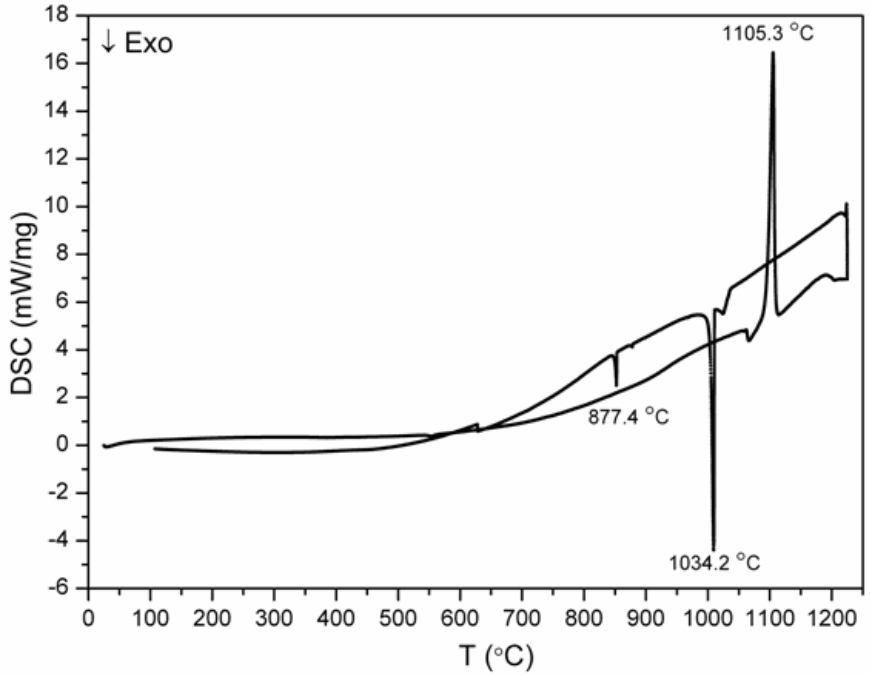

Figure 3.29 The DSC curve of $Ba_8Ni_{3.3}\square_{0.7}Si_{42}$ heated up to 1250 °C.

3.6 Theoretical Calculations

The theoretical calculations were performed in collaboration with *Dr. Alim Örmeci* at MPI-CPfS, Dresden. The clathrate compounds with $Ba_8(Ni_xGe_y)Ge_{40}$ (x + y = 6) composition were studied with first-principles electronic structure calculations. Since Ni atoms are expected to occupy the Wyckoff *6c* site, fully ordered compounds can be

obtained when x = 0 or 6. As explained in the section on crystal structure, this unit cell is cubic and contains 54 atoms. For these cases, all-electron full-potential local orbital (FPLO) method is used. FPLO is based on the construction of extended crystal wave functions via a linear combination of overlapping nonorthogonal basis orbitals. The representation of density and potential is a lattice sum of local overlapping contributions [103]. In this method, the whole space is treated in a uniform manner so that charge density is continuous at all points.

For x = 2 or 4, it is possible to model the observed disordered compounds in a tetragonal 1 x 1 x 2 supercell with space group *P 41 2 2* (No.91) (Figure 3.30). Because the unit cell in such cases contains 108 atoms, the tight-binding linear muffin-tin orbital method within the atomic sphere approximation (TB-LMTO-ASA) was used [104-106]. Compared to FPLO method in which atomic spheres are absent, overlapping atomic spheres are used in this method.

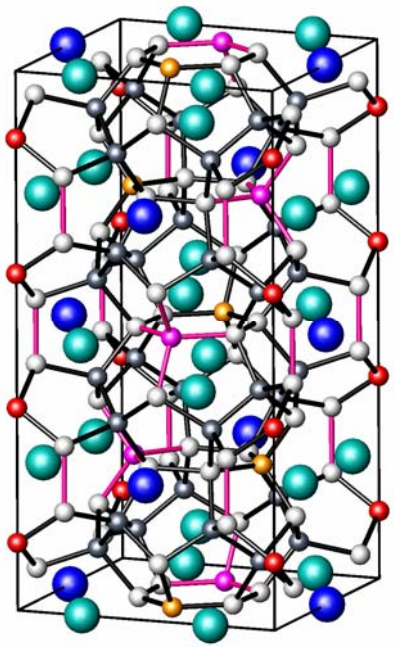

Figure 3.30 Tetragonal supercell with 108 atoms for $Ba_8Ni_4Ge_{42}$. The atoms are in colors as following: blue (light): Ba1, blue: Ba2, pink:Ge1, gray:Ge2, gray(light): Ge3, red&orange: Ni1.

Zintl-Klemm-Busmann or shortly Zintl rules are assumed to be applicable to the present clathrate system. As explained in chapter 1, in a Zintl compound the formal electronic structures can be explained as such: the most electropositive guest atom behaves as an electron donor and transfers its valence electrons to the more electronegative host atoms. For a binary clathrate such as Ba_8Ge_{46} this would mean that 8 Ba atoms having valence of 2+ transfer total of 16 electrons to the cage atoms. In the mixed clathrate of $Ba_8Ni_4Ge_{42}$, the four Ni atoms are assumed to receive all 16 electrons provided by Ba atoms, so that each Ni becomes formal Ni^{4-} enabling them to form tetrahedral covalent bonds with the four neighboring Ge atoms. Hereby, Ge remains formal zero and behaves 4b: $[Ba^{2+}]_8\{[Ni^{4-}(4b)]_4[Ge^0(4b)]_{42}\}$. If this picture is correct, then there will be no excess electrons left, since all available electrons will be used for forming covalent bonds; therefore the material is expected to be a semiconductor. We can model the conductivity behaviors of these compounds like in the case of extrinsic semiconductors. Since Zintl rules seem to be hold for $Ba_8(Ni_xGe_y)Ge_{40}$ ($x + y = 6$) with $x = 4$, it can be concluded that for $x < 4$, there will be excess electrons in the compound giving rise to metallic behavior where the charge carriers are electrons (n type). Likewise, for $x > 4$, there will be electron deficiency. For this range of x values, metallic behavior is also expected (finite number of DOS at the Fermi level) where the charge carriers are holes (p type). The DOS computed by FPLO for $x = 0$ (Ba_8Ge_{46}) and $x = 6$ ($Ba_8Ni_6Ge_{40}$) are in good agreement with this reasoning (Figures 3.31-3.32). On well characterized samples Hall Effect measurements can be performed to confirm the theoretical predictions regarding the type of charge carriers.

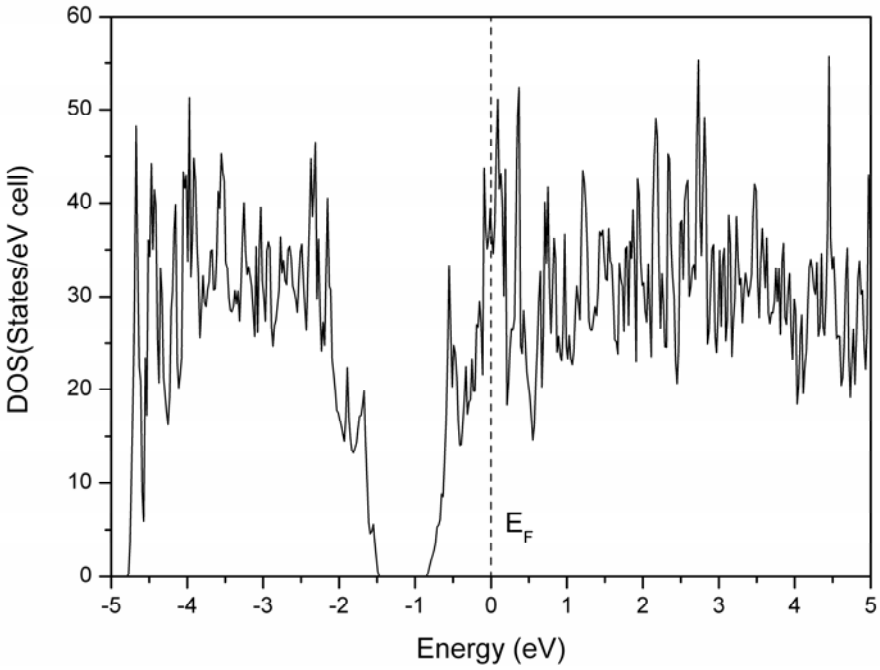

Figure 3.31 Total density of states (DOS) for Ba_8Ge_{46}**.**

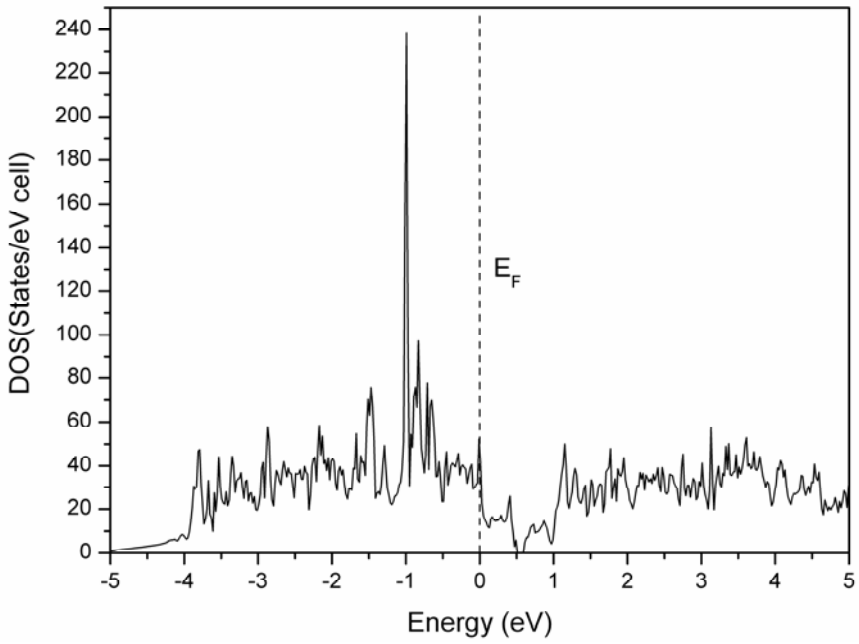

Figure 3.32 Total density of states (DOS) for $Ba_8Ni_6Ge_{40}$**.**

Band structure calculations performed by the TB-LMTO-ASA method also confirm this expectation for the $Ba_8Ni_4Ge_{42}$ case. The calculated density of states (DOS) for this compound has a very small gap, 0.13 eV, indicating a semiconducting behavior. Total DOS and band structure are shown in Figures 3.33 and 3.34, respectively. From the band structure calculations, the band gap is found to be indirect (the top of the valence band is near Gamma point and bottom of the conduction band is near M).

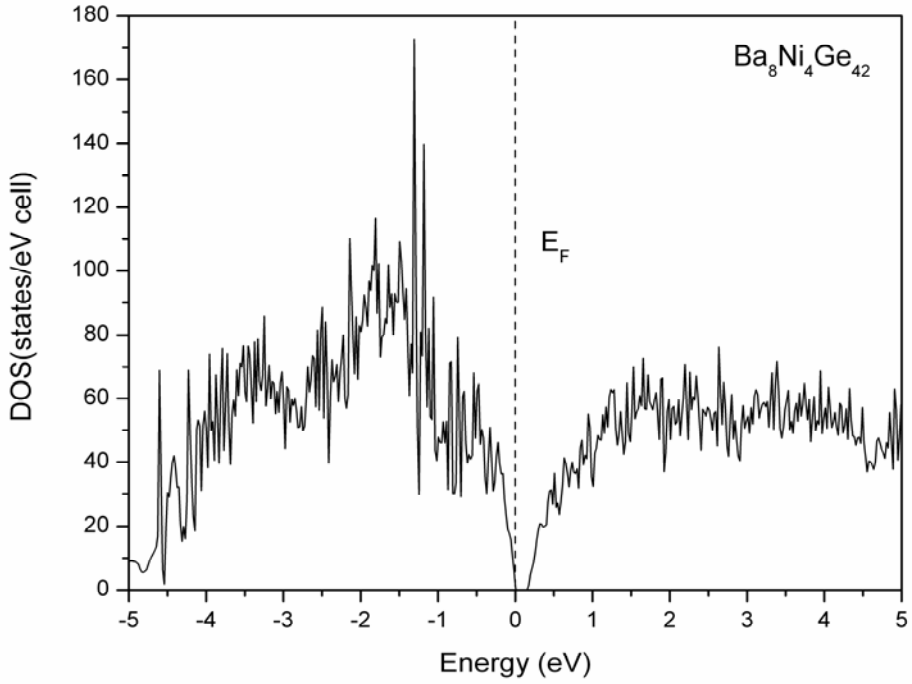

Figure 3.33 Total density of states (DOS) for $Ba_8Ni_4Ge_{42}$.

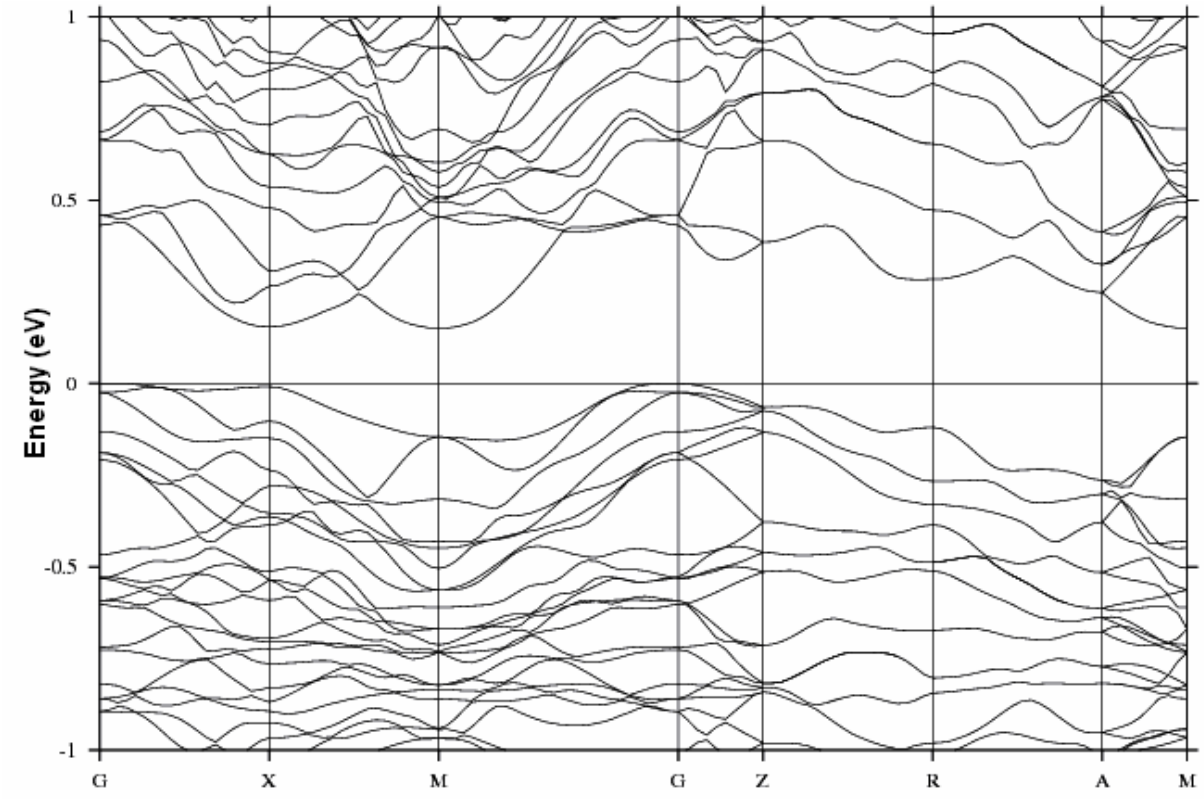

Figure 3.34 Band structure for $Ba_8Ni_4Ge_{42}$ near band gap region.

The electron localization function (ELF) [107-109] was also computed for $Ba_8Ni_4Ge_{42}$. It was introduced by Becke and Edgecombe as a tool aiming to identify the regions where electrons are localized in atomic and molecular systems [107]. Then, Savin et al. suggested an alternative interpretation which is based on the calculation of ELF by density functional methods [108]. Nowadays it is a widely used tool for studying chemical bonds in molecules and solids [109]. From the ELF calculations, it was observed that Ni atoms are found to form covalently bonded tetrahedral arrangement with their Ge neighbors. In Figure 3.35, the ELF distribution is shown for the isosurface value of 0.585. Although the bonding attractors for Ge-Ge bonds are located near the mid-points of the bonds, but are somewhat

displaced from the bond line, the attractors for Ni-Ge bonds are "ring-like" and the intersections with the bond lines occur at smaller ELF values.

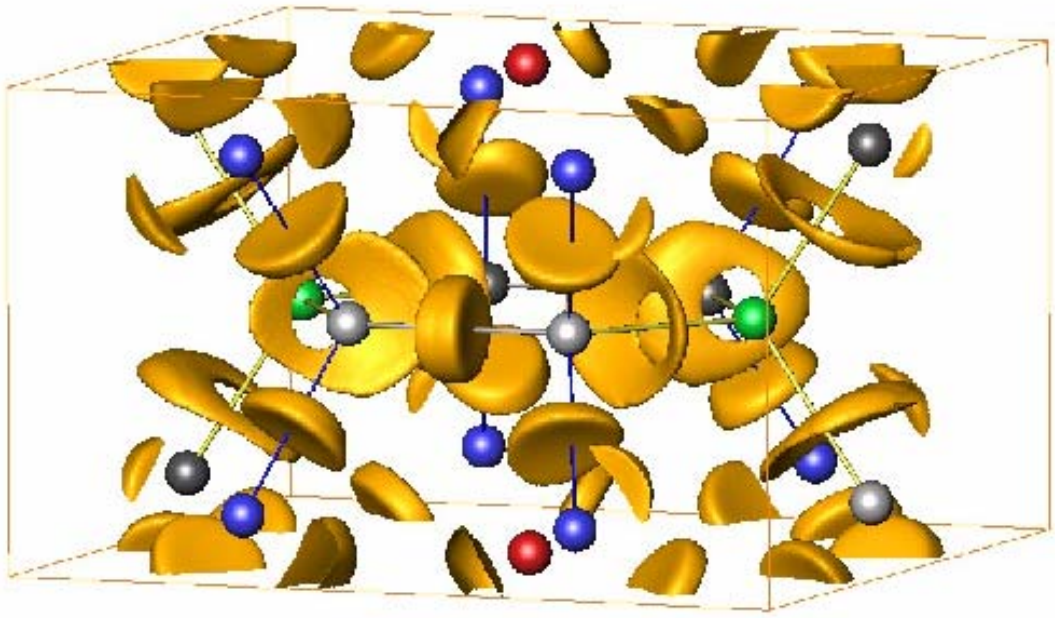

Figure 3.35 Electron localization function (ELF) isosurfaces for $Ba_8Ni_4Ge_{42}$. Atoms with colors: red: Ba2, green: Ni, blue: Ge2, and gray: Ge3.

3.7 Physical Properties

3.7.1 Electrical Resistivity Measurements

Investigations of electrical-transport properties of $Ba_8(T_xGe_y\square_z)(Ge)_{40}$ (T = Ni, Pd, Pt; $\square$ = defect; x+y+z = 6) compositions revealed a semiconductor–metal transition in terms of electrical resistivity (Figures 3-36-3.37). $Ba_8Ni_4Ge_{42}$ compound clearly displays a semiconducting property as predicted by the theory.

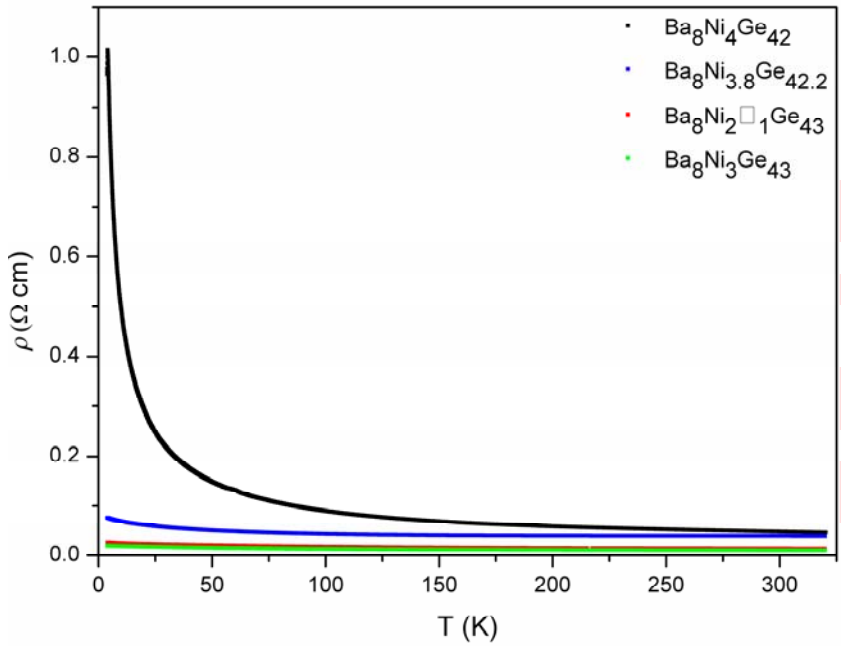

Figure 3.36 Electrical resistivity versus temperature for Ge clathrates with Ni.

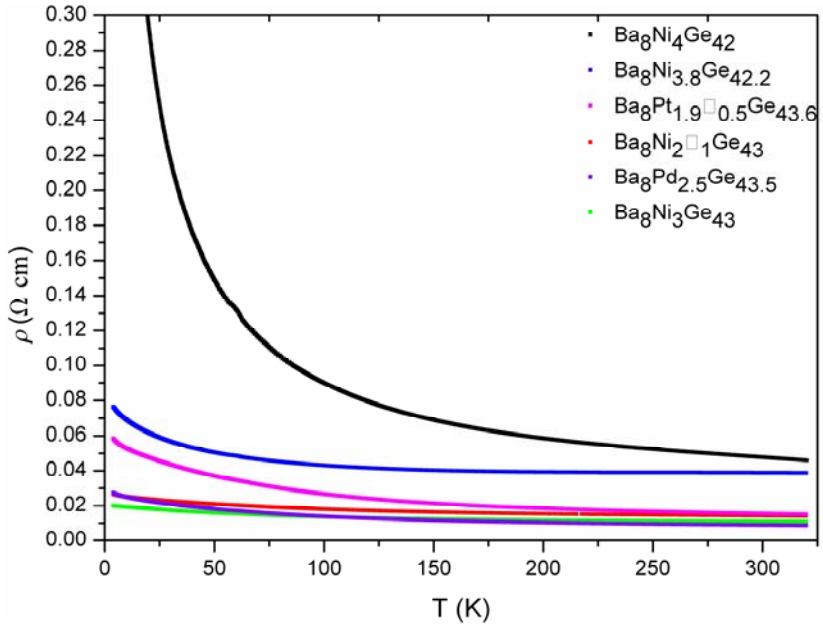

Figure 3.37 ρ vs. T for Ge clathrates with Ni, Pd and Pt.

These resistivity behaviors can be explained using Zintl-Klemm-Busmann concept as discussed in theoretical calculations. Based on this concept, the following charge balanced formulas can be proposed for the title compounds as,

$Ba_8Ni_4Ge_{42}$: $(Ba^{2+})_8$ $((4b)Ge^0)_{42}$ $(Ni^{4-})_4$

$Ba_8Ni_3Ge_{43}$: $(Ba^{2+})_8$ $((4b)Ge^0)_{43}$ $(Ni^{4-})_3(4e^-)$

$Ba_8Ni_2\square_1Ge_{43}$: $(Ba^{2+})_8((3b)Ge^-)_4(Ni^{4-})_2((4b)Ge^0)_{39}(4e^-)$

where $(3b)Ge^-$ are three-bonded and $(4b)Ge^0$ are four-bonded Ge species shown in Figure 3.38.

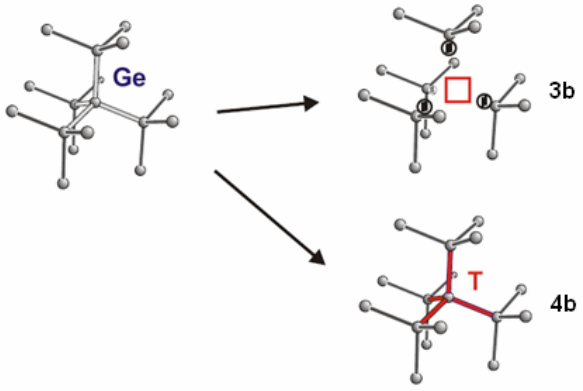

Figure 3.38 Three bonded and four bonded atoms in tetrahedral arrangement.

The bonding situation has already been discussed in 3.6, according to which the valence electrons in $Ba_8Ni_4Ge_{42}$ are used entirely for forming covalent bonds, in good agreement with the observed semiconducting behavior. For the other cases due to the extra 4 electrons per formula unit remaining in the conduction band of the cage framework, all these compounds should be metallic conductors. Hence, this provides a nice agreement between experimental data and the theory.

The band gap of semiconductor, $Ba_8Ni_4Ge_{42}$, can be found from the high temperature resistivity data as explained in section 2.4.4 by using equation 2.9. A plot of ln ρ/ρ_0 versus 1/T gives a slope which is equal to $E_g/2k_B$ (Figures 3.39-3.40). From the equation, energy band gap E_g was determined to be E_g = 11.518(2) meV.

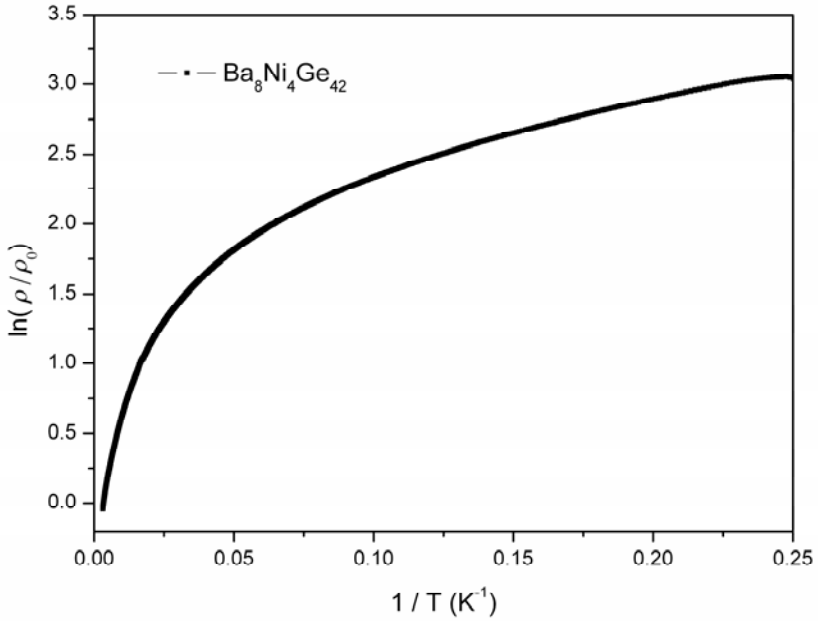

Figure 3.39 ln(ρ) vs. 1/T curve for $Ba_8Ni_4Ge_{42}$.

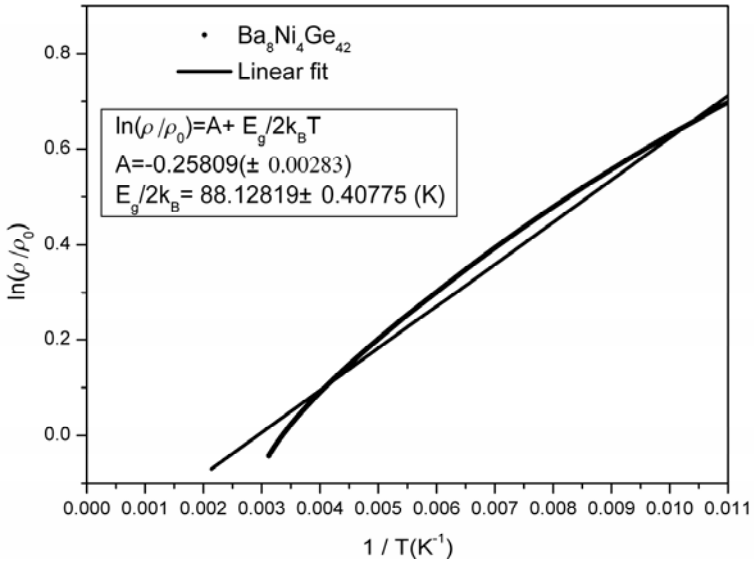

Figure 3.40 ln(ρ) vs. 1/T curve for $Ba_8Ni_4Ge_{42}$ at high temperature regime.

Although the compunds with Pd and Pt show the same resistivity behaviors as observed for Ni case, the behavior completely changes in the case of the Si compound (Figure 3.41). Almost linear increase of resistivity with respect to increasing temperature indicates a metallic behavior of $Ba_8Ni_{3.3}\square_{0.7}Si_{42}$. Room temperature resistivity around $4.2x10^{-5}$ Ωm indicates a bad metallic conduction. This behavior originates from the strong hybridization of 5d orbitals of Ba with the Si 3p states, high density of states resulting at the conduction edge.

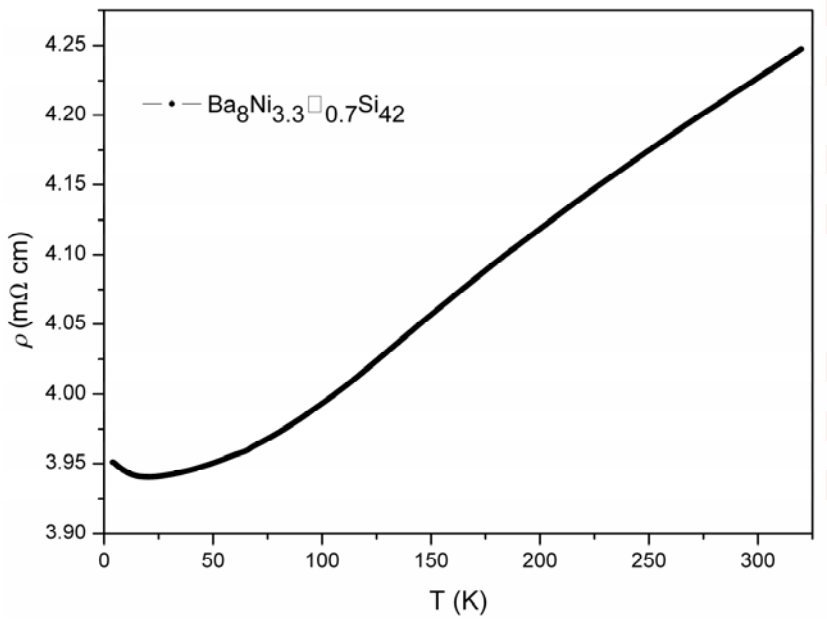

Figure 3.41 Electrical resistivity as a function of temperature for $Ba_8Ni_{3.3}\square_{0.7}Si_{42}$.

No superconductivity was observed for any compound in a temperature range down to 2 K. It has to be kept in mind that in powder samples, polycrystals are more interrupted and separated in comparison to single crystals thus increasing the overall resistivity.

3.7.2 Thermal Conductivity Measurement

For maximum performance of a thermoelectric material, high electrical and low thermal conductivity would be required as indicated on previous chapters. However, good conductors of electricity are usually good conductors of heat as well, whereas the thermopower reaches its maximum for small band-gap semiconductors [6]. Therefore thermal conductivity of polycrystalline small band gap $Ba_8Ni_4Ge_{42}$ semiconductor was investigated. Figure 3.42 shows lattice thermal conductivity, $\kappa_L(T)$, and electronic thermal

conductivity, $\kappa_{e,}$ of $Ba_8Ni_4Ge_{42}$ in the temperature range 1.8-300 K in a semilogarithmic plot.

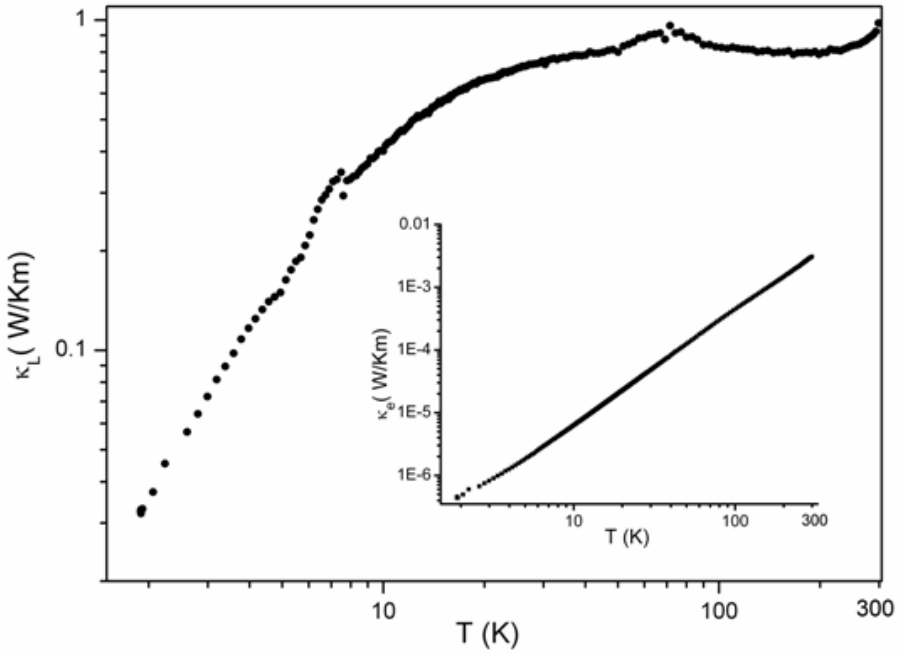

Figure 3.42 Temperature dependence of the lattice thermal conductivity $\kappa_L(T)$ of $Ba_8Ni_4Ge_{42}$ on a double - logarithmic scale. The inset shows the electronic contributions $\kappa_e(T)$ obtained as explained in the text.

κ_L(T) was calculated by subtracting the electronic contribution from κ(T). The electronic thermal conductivity was estimated using the electrical resistivities and Wiedemann-Franz law with ideal Lorenz number according to the equation 2.18. For the title compound, κ_e ranges between $4.5x10^{-7}$ and $3x10^{-3}$ W/Km and increases almost linearly with increasing temperature as expected for semiconducting materials. The room temperature value of lattice thermal conductivity, around 1W/Km, is very small and lying between that of amorphous SiO_2, a-SiO_2, and amorphous Ge, a-Ge, like the other clathrates shown in Figure 3.43.

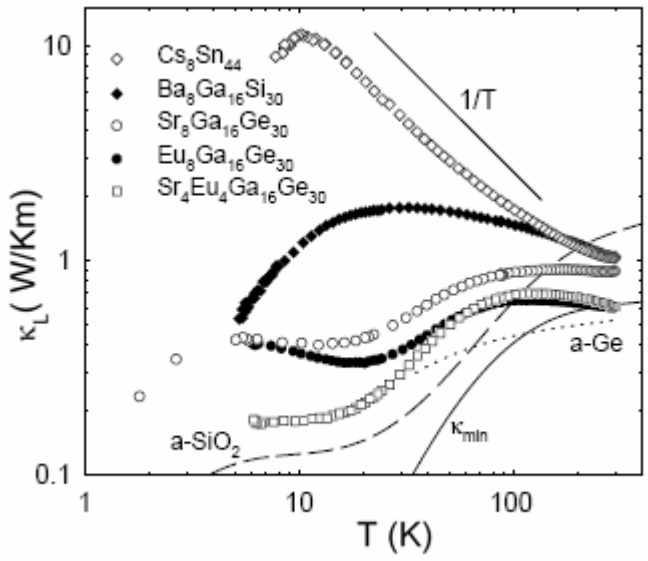

Figure 3.43 Lattice thermal conductivity vs. temperature for the five clathrate specimens. The dashed and dotted curves are for a-SiO_2 and a-Ge[110].

When considering Figure 3.43, the Sn clathrate is exhibiting a temperature dependence of crystalline insulator in which the lattice thermal conductivity decrease as temperature increase in 1/T relation. For the Si compound, the same behavior is also observed above 20 K but not as strong as in the Sn case indicating additional scattering at low temperatures. The Ge clathrates on the same figure show glass-like temperature dependence predicted from $\kappa_L \propto T^2$ depence at lowest temperatures and nearly temperature independent κ_L at relatively high temperatures. In considering $Ba_8Ni_4Ge_{42}$, as temperature increases from 1.8 to 6 K the sample has an approximate $T^{1.63}$ dependence which is similar to glass-like thermal behavior (Figure 3.44). The source of this temperature dependence could be phonon charge carrier scattering.

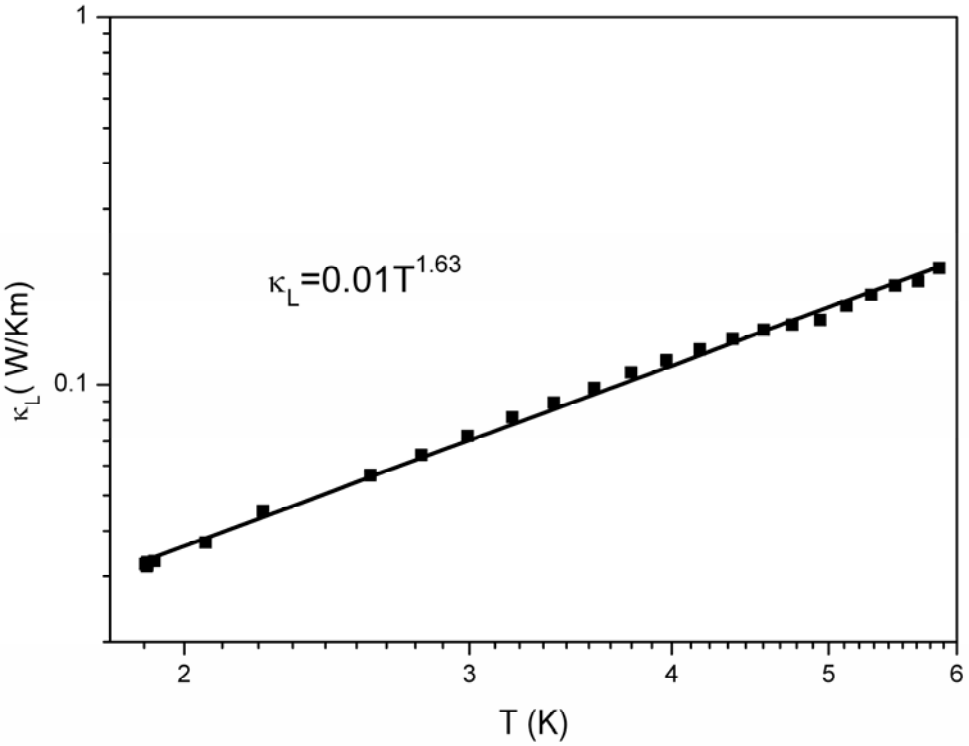

Figure 3.44 Lattice thermal conductivity as a function of temperature with fit represented by solid curve.

Considering Figure 3.42, as the temperature increases further, starting at around 40 K a broad plateau with a minimum at around 200K appears and is followed by a monotonic increase of κ_L with increasing temperature. $\kappa_L(T)$ above 40K is determined from resonant scattering of phonons from the Ba^{2+} cation in the cages. The anomalies at 7.6 and 70 K originate from the measurement conditions. However the increase of κ_L above 200 K is questionable. The reasons could be as following: first κ_e calculated from Widemann-Franz law is only exact in the limit $T \longrightarrow 0$ and a small error at high temperatures may be the reason for the apparent upturn in κ_L. Heat radiation emitted during the measurement might be another reason.

3.7.3 Magnetic Susceptibility Measurements ,

Magnetic properties of clathrates with different compositions were investigated. Figure 3.45 shows the temperature dependence of magnetic susceptibilities of compounds at applied magnetic field of 70 kOe.

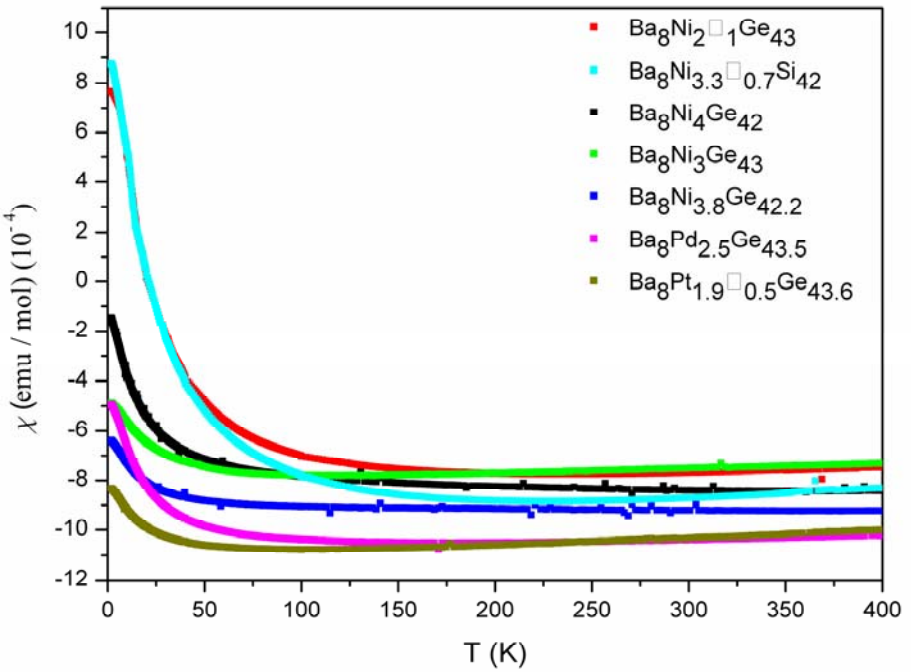

Figure 3.45 Temperature dependence of magnetic susceptibilities for Si and Ge clathrates at H = 70 kOe.

Almost for all samples, the susceptibility consists of both diamagnetic and Curie-Weiss paramagnetic susceptibilities. The Curie-Weiss behavior is mainly due to the magnetic impurities found at ppm levels which could not be detected in the X-ray powder diagram. The metallographic findings give rise to the assumption that the impurities are stemming primarily from binary transition metal silicides and germanides, $T_x(Ge,Si)_y$. These paramagnetic moments of impurities are more present in $Ba_8Ni_{3.3}\square_{0.7}Si_{42}$ and $Ba_8Ni_2\square_1Ge_{43}$

samples obvious from longer paramagnetic tails at low temperatures. The susceptibilities slightly decrease with increasing temperature, above 100 K for the two respective samples and 50 K for all the others, reaching negative values and remaining almost constant above these temperatures. The measured negative susceptibility values correspond to the diamagnetic susceptibilities of the samples varying between -7.5 x 10^{-4} and -10.3 x 10^{-4} emu/mol. The least squares fits (performed with OriginPro 7.0, Figure 3.46) of the data of χ versus T at H = 10kOe between $1.8 \leq T \leq 100$ K to

$$\chi = \chi_0 + \frac{C}{(T - \theta)} \tag{3.4}$$

for $Ba_8Ni_{3.3}\square_{0.7}Si_{42}$ and $Ba_8Ni_2\square_1Ge_{43}$ yield temperature independent susceptibilities as $\chi_0 = -12.9\times10^{-4}$ and -12.1x10^{-4} emu/mol, respectively. Following the same equation, Curie-Weiss constants, C, and Curie-Weiss temperatures, θ , were found to be 5.91x10^{-2}, 5.69x10^{-2} emu K / mol and -23.9 and -24.6 K, respectively. The magnitude of temperature independent susceptibilities are little larger than that of diamagnetic susceptibilities mentioned above.

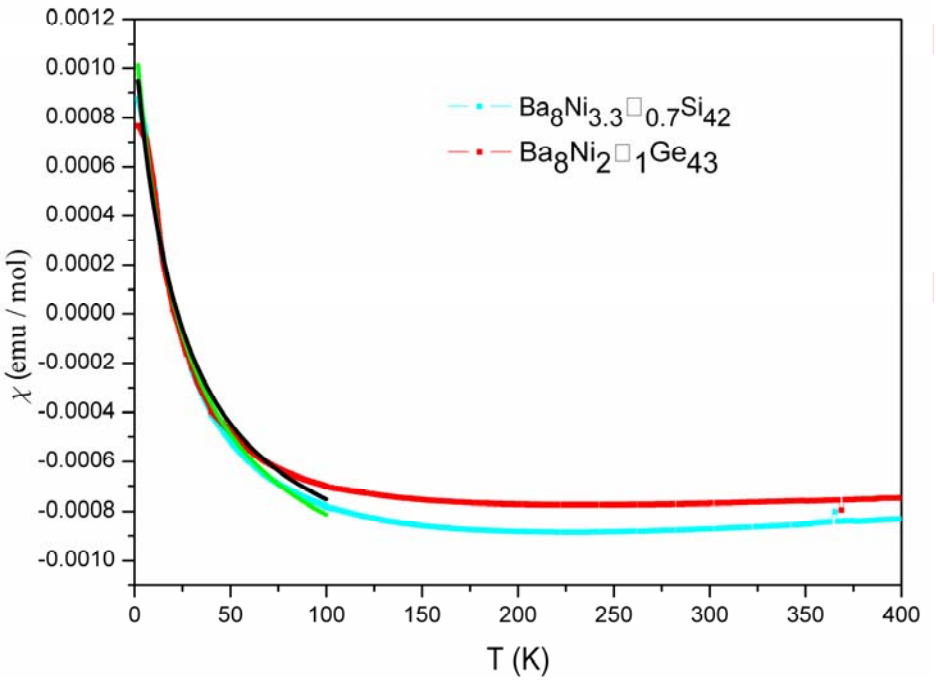

Figure 3.46 Magnetic susceptibilities for $Ba_8Ni_{3.3}\square_{0.7}Si_{42}$ and $Ba_8Ni_2\square_1Ge_{43}$. The green and blue curves denote the least-squares fittings to equation (3.6). The fitting parameters are given in the text.

The calculation of effective magnetic moments of the Curie-Weiss paramagnetic impurities were performed with,

$$P_{eff} = (3k_B C / N_0)^{\frac{1}{2}} \qquad (3.5)$$

where N_0 is the avagadro's number, k_B is the Boltzmann's constant and C is the Curie-Weiss constant[100]. The formula 3.5 gives the effective magnetic moment in units of erg/Oe in terms of cgs units. Dividing the results by 0.927×10^{-20} (erg/Oe)/μ_B give the P_{eff} in terms of Bohr magneton, μ_B. The effective magnetic moments for $Ba_8Ni_{3.3}\square_{0.7}Si_{42}$ and

$Ba_8Ni_2\square_1Ge_{43}$ were found to be 0.73 and 0.67 μ_B which are too less for 54 atoms per unit cell.

3.8 Conclusions and Outlook

In this project, polycrystalline single phase samples of compounds with $Ba_8(T_x(Ge,Si)_y\square_z)(Ge,Si)_{40}$ (T = Ni, Pd, Pt; $\square$ = defect; x+y+z = 6) compositions were successfully synthesized. Powder and single crystal X-ray diffraction were used to check phase purity, determine and refine the crystal structures and investigate the localized vibrational modes of rattlers in terms of ADPs. Crystal structure refinements show that there is no significant change in the crystal structures within the range of the compounds investigated. All clathrates belong to type I structure and have the same space group $Pm\bar{3}n$. Microstructure analyses were performed with WDXS and EDXS techniques to check the phase purities, identify the additional phases if present, and also to determine the exact compositions of the additional phases and clathrate compounds. The results of the metallographic studies revealed that ternary clathrates form at a peritectic temperature and are in equilibrium with some ternaries, binaries, elemental Si or Ge and melt. Based on the WDXS results, homogeneity phase range of clathrates with nickel was determined on a nickel-germanium-void ternary phase diagram. Thermal analysis with DSC method was used to analyze the thermal stability of the compounds. Investigations on Ge clathrates show that they decompose at temperature range between 835 and 855 °C. The same analysis shows also that the sample with Si is stable until 1105 °C. Band structure and density of states calculations indicate that the samples depending on the Ni content exhibit either semiconducting or metallic properties. $Ba_8Ni_4Ge_{42}$ was found to be semiconducting with a band gap energy of 130 meV. The compounds with low or high Ni contents show metallic behavior, where the charge carriers are either electrons (n type carrier), or holes (p

type carrier), respectively. Electron localization function calculation elucidates the covalently bonded tetrahedral arrangement of Ni atoms with their Ge neighbors. A detailed investigation of transport and magnetic properties of clathrates have also been conducted. For compounds with Ni, a semiconductor–metal transition in terms of electrical resistivity has been observed, as predicted by theoretical calculations. The band gap energy of $Ba_8Ni_4Ge_{42}$ was calculated from the high temperature resistivity data as 11.5 meV which is also in fairly good agreement with the value predicted by band structure calculation. No superconductivity was observed for temperatures down to 2 K. The low thermal conductivity of these compounds can be explained in terms of the dynamic rattling modes of the Ba2 atoms inside tetrakaidecahedra, which couple with the lattice modes by resonantly scattering the acoustic mode heat carrying phonons of the host framework atoms. It can be also deduced from the low temperature single crystal X-ray analysis. Atomic displacement parameters obtained from that analysis were used to determine the Einstein temperature and localized vibration frequencies of the rattler, the Debye temperature for the cage framework and the velocity of sound. Here the Einstein mode interacts with the acoustic phonons of the Debye host. Magnetic susceptibility measurements showed a large diamagnetic response consistent with semiconducting or semimetallic behaviors.

It is worth mentioning that the title compounds $Ba_8(Ni_xGe_y\square_z)Ge_{40}$ ($\square$ = defect; x+y+z = 6) were selected as model substances for fundamental understanding of the guest - host interactions, bonding situation and structure-property relationships for clathrates, at the Virtual Laboratories C (VIL-C) meeting organized by European Network of Excellence – Complex Metallic Alloys which took place on 20-21 February 2006 in Stuttgart. With this insight, the compositions intended to be tuned to systematically improve figures of merit for technological applications. One way to optimize the thermoelectric property is to substitute Ba with rare earth guest atoms like Yb and Sm. The main aim in doing so is to

enlarge Seebeck coefficient which is proportional to the gradient of the electronic DOS at the Fermi energy level. Sharp DOS peaks can be created by the introduction of rare earth guest atoms as their f-electrons cause narrow bands with hybridization and strong electron correlations. Rare earth elements are known to be multivalent and strong electron donors requiring as counterparts strong electron acceptors among the cage atoms like Ni. In this respect, large single crystals growth, theoretical calculations, structure and physical property investigations will be done by different groups in Europe including MPI-CPfS.

Chapter 4

TANTALUM NICKEL SILICIDE (TaNiSi)

4.1 Synthesis

Ternary TaNiSi was prepared using a new synthesis route by melting the binary NiSi in Ta ampoule. The educts were purchased as ultra pure chemicals from ChemPur. For the synthesis of NiSi, chunks of Si were finely powdered down to sizes around 80 μm via using a tungsten carbide mortar and then pressed to a 6 mm pellet. Ni was used as a foil and then cut into smaller pieces. Silicon pellet and Nickel foil (ratio of 1:1) were then arc-melted under Ar atmosphere to yield nickel silicide. After the synthesis, NiSi was placed in a Ta tube (d = 8mm) and annealed for four days at 1323 K which is around 60 K higher then the melting temperature of NiSi (Figure 4.1). During the annealing process, the corrosive NiSi melt dissolves Ta from the crucible surface resulting in formation of ternary TaNiSi. The metallic gray final product is air and moisture stable.

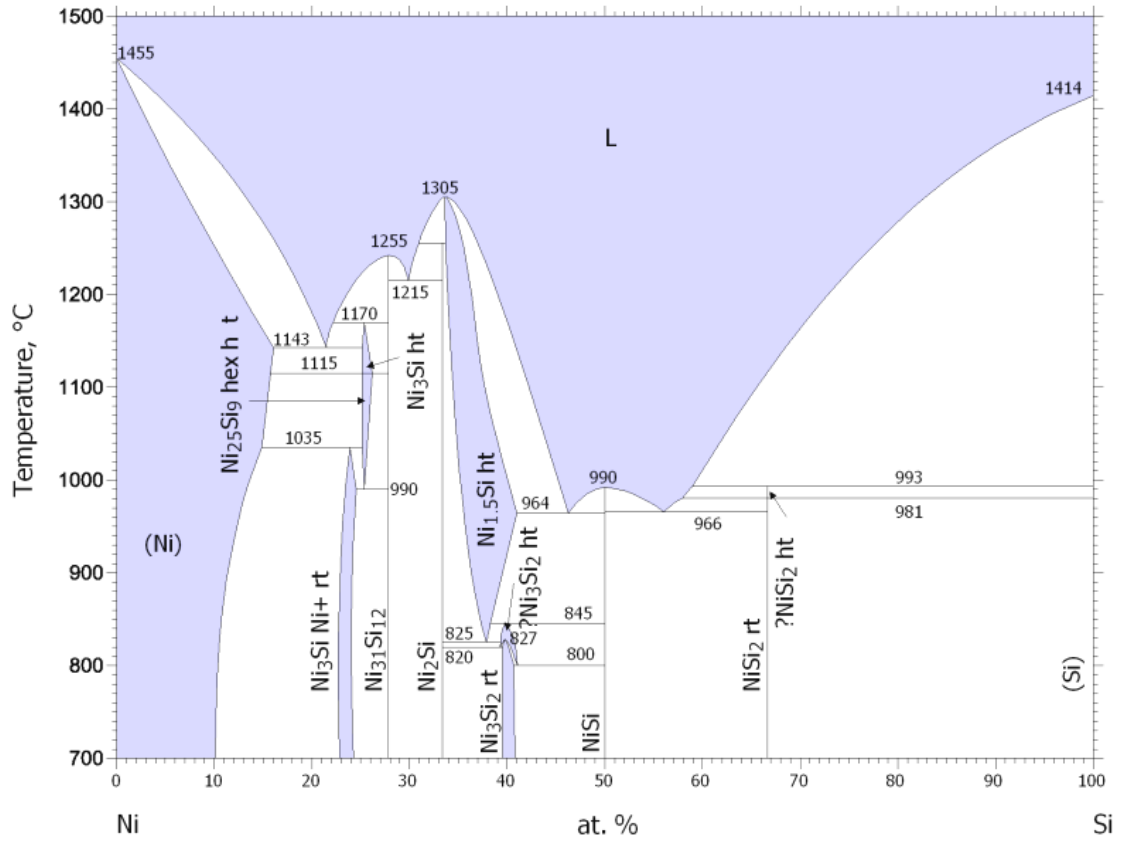

Figure 4.1 Phase diagram of the NiSi [111]

X ray powder diffraction was employed for the investigation of the phase purity. Figure 4.2 shows the observed and calculated powder patterns from the structure determination. No byproduct could be detected by the analysis.

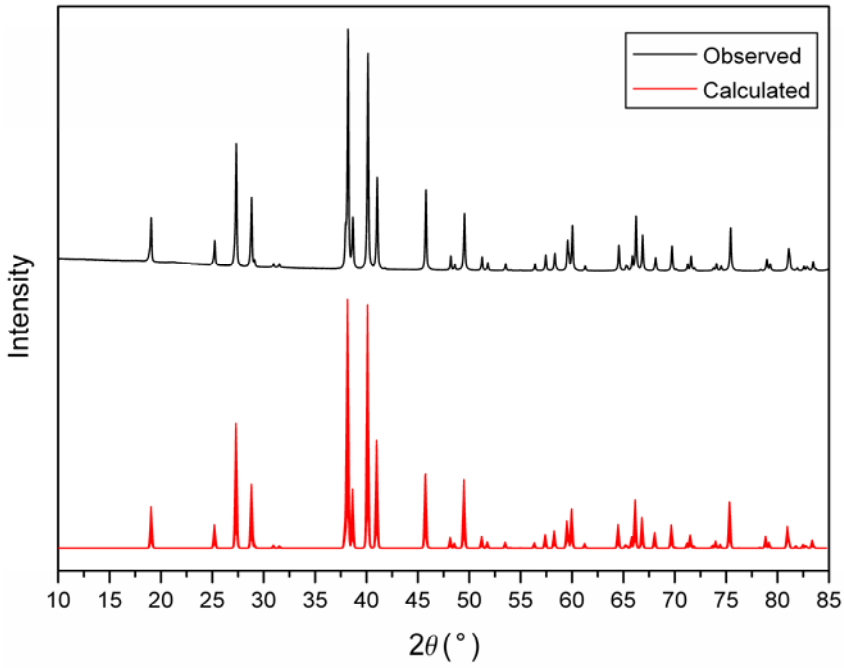

Figure 4.2 Observed and calculated X-ray powder diffraction patterns of TaNiSi.

4. 2 Microstructure Analyses

Due to the mutual interference of the peaks of Ta / Si and Ta / Ni in EDXS, WDXS analysis was applied with SiKα[TaMα/β] and TaLα[NiKβ] peak overlap corrections. For the microstructure analysis, a chunk of sample was embedded in epoxy resin substrate containing carbon fibers increasing the surface conductivity. Grinding was performed using fixed abrasive papers mainly silicon carbide and either alcohol including lubricant or water. Polishing was done in steps by using slurry with different micron sized diamond powders (6, 3, ¼) in paraffin. After each step the specimens were cleaned with ethanol to remove all remaining particles. For the WDXS measurements, NiSi and Ta were selected as standards.

The WDXS analysis was performed at ten different points on a polished TaNiSi surface (Figure 4.3). The average of the results gives the chemical composition of $Ta_{1.0}Ni_{1.0}Si_{1.1}$

(Table 4.1). Since the peak overlapping was still causing problems in terms of determination of the exact and reliable compositions, the sample of the composition 1: 1 : 1.1 was finally regarded as TaNiSi. The EDXS results show that the sample is single phase (figure 4.4).

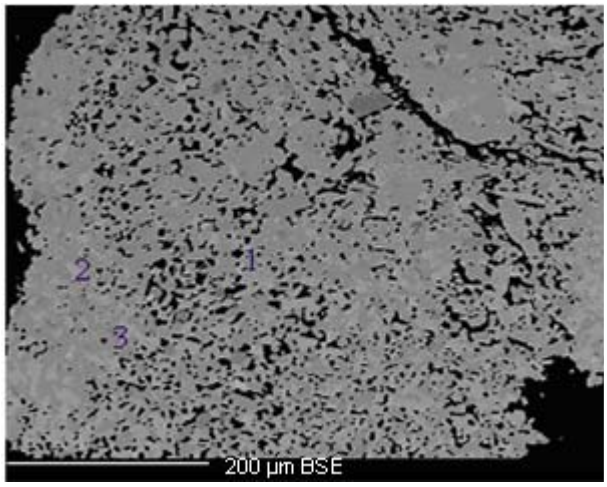

(a)

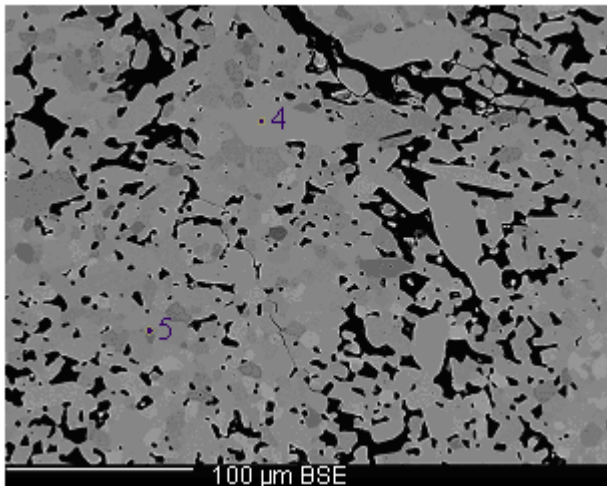

(b)

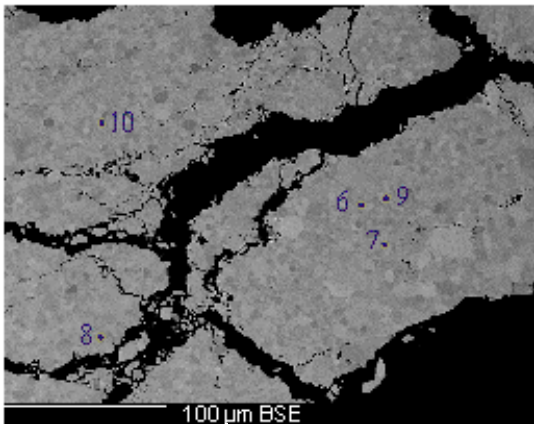

(c)

Figure 4.3 (a), (b), (c): Back-scattered electron images with the points in which the measurements are done.

Table 4.1 WDXS quantification result for ten different points on the sample**.**

Average	Weight %	NormWeight %	Atomic %	Dev_Wt
Si	11.56	11.40	35.35	0.08
Ni	22.26	21.95	32.57	0.15
Ta	67.60	66.65	32.09	0.18
Total	101.42	100.00	100.00	

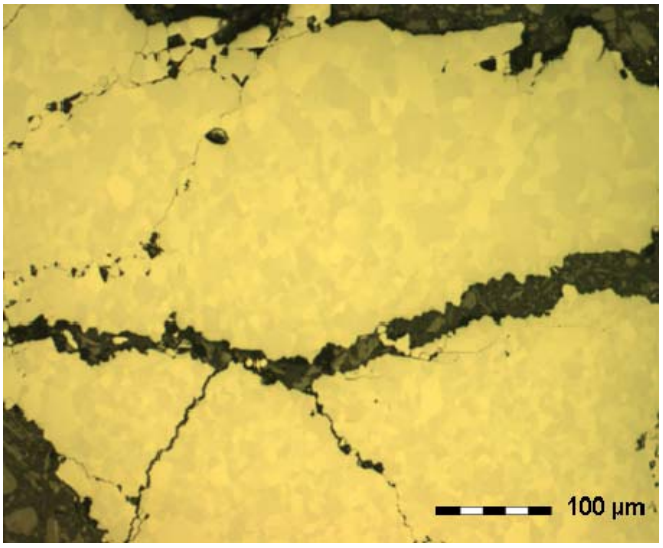

Figure 4.4 Bright-field optical microscope image of TaNiSi.

4.3. Crystal Structure Determination

The crystal structure of TaNiSi was determined by a single crystal X-ray diffraction experiment. For the analysis, a suitably sized crystal with well-formed edges and faces was mounted properly with grease on top of a sharpened end of a glass capillary. After checking the crystal quality with Laue photographs, single crystal data were collected by a STOE IPDS diffractometer (AgKα radiation, graphite monochromator). The data were

corrected for Lorentz and polarization effect and a multi-scan absorption correction was applied. The structure solutions and refinements were performed with SHELXS-97 and SHELXL-97 programs found in WinGX software. The crystallographic results are summarized in table 4.2. Atomic coordinates and the displacement parameters are given in tables 4.3 and 4.4. Estimated standard deviations (e.s.d) are in parenthesis.

Table 4.2 Crystallographic data and refinement details for TaNiSi

Space Group	*Pnma* (No. 62)
Cell Parameters[Å/°]	a= 6.1907(3) / 90
	b= 3.6769(2) / 90
	c= 7.0542(4) / 90
V[Å^3] / Z	160.57 / 4
Diffractometer	STOE IPDS diffractometer with graphite monochromator
X-ray source	AgKα (0.56087)
2θ range [°]	7.0 - 51.53
Miller-index range	$-9 \leq h \leq 9$
	$-5 \leq k \leq 5$
	$-10 \leq l \leq 10$
No. of measured reflections	2365
Unique data	352
Observed data ($F_0 > 4\sigma F_0$)	328
Number of parameters refined	20
R1($F_0 > 4\sigma F_0$)	0.0197
R1(all data)	0.0223
wR2 ($F_0 > 4\sigma F_0$)	0.0385
wR2 (all data)	0.0385
Goof (for F^2)	1.178

Table 4.3 Atomic coordinates, equivalent isotropic displacement parameters ($Å^2$) and occupancies for TaNiSi.

Atom	Site	x	y	z	Ueq	Occ. (%)
Ta	4c	0.01777(4)	0.25000(0)	0.67630(4)	0.00274(12)	1
Ni	4c	0.15422(13)	0.25000(0)	0.06856(14)	0.00411(18)	1
Si	4c	0.27983(28)	0.25000(0)	0.38393(31)	0.00356(32)	1

Table 4.4 Anisotropic displacement parameters (Uij x 10^4 ($Å^2$) for TaNiSi.

Atom	U11	U22	U33	U12	U13	U23
Ta	13 (2)	43 (2)	26 (2)	0	-2 (1)	0
Ni	31 (3)	54 (4)	37 (4)	0	6 (3)	0
Si	27 (6)	35 (7)	45 (9)	0	6 (5)	0

No superstructure reflection was observed from the close investigations of both single crystal and powder XRD experiments. The observed Laue symmetry and systematic extinctions were compatible with the space group of *Pnma* (No. 62) for the crystal refined. This space group was tried for refinements and the statistically better solutions were chosen on the basis of *R* values and number of other variables. The initial positions of all atoms were obtained from direct methods. Once all atoms were assigned, the occupancies of atoms at all sites were fixed with full occupancy. The lattice parameters were refined from the X-ray powder diffraction analysis as 6.1919(2), 3.6770(2) and 7.0526(3) Å in accordance with the single crystal analysis results.

4.4 Crystal Structure Description

Different branches of the $PbCl_2$ structure types reach from pure ionic compounds up to intermetallic phases and phases with covalent character. A tetrahedral environment of atoms in ionic compounds and a 3D four-connected anionic network of atoms in covalent compounds lead only by chance to a similar topology and the question arises, whether such phases are comparable with each other at all.

In TaNiSi, the (NiSi) substructure is characterized by chair-like six membered rings of alternating Ni and Si atoms which are further condensed to form corrugated 6^3 layers parallel to *bc* plane (Figure 4.5). The stucking of these nets follow (..AB..) arrangement. The 6^3 layers are further interconnected via (Ni-Si) linkages along *a*, generating small rectangular and large octagonal channels along *b* (Figure 4.6). The larger octagonal channels are filled by Ta atoms. Both Ni and Si are mutually coordinated by four neighbors, respectively.

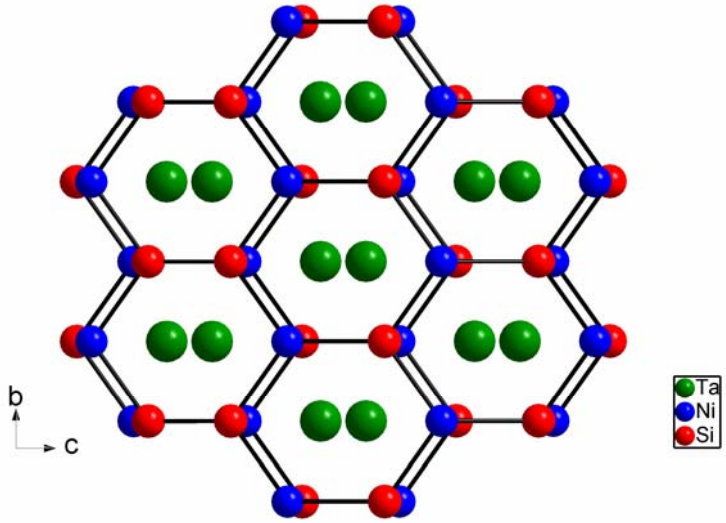

Figure 4.5 View of crystal structure along a axis showing the stacking of the corrugated 6^3 nets formed by Ni and Si atoms.

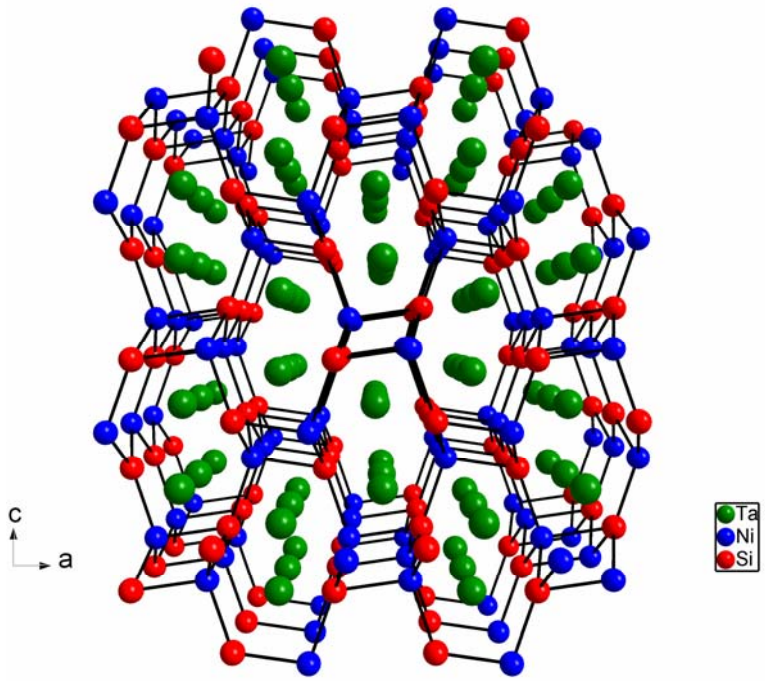

Figure 4.6 View of crystal structure with small rectangular and large octagonal channels along b.

The local environment around Ni corresponds to a distorted tetrahedron with d(Ni-Si) = 2.290(2) (2x), 2.342(2) and 2.357(2) Å, in good agreement with those reported for binary NiSi: d(Ni-Si) = 2.277-2.400 Å [112]. The bond angles ∠(Si-Ni-Si) vary in the range of 101.04(6)-118.56(4)°. The coordination polyhedra around Si correspond to a very irregular tetrahedron, in which the silicon atom has moved from the central position to occupy a triangular face (Figure 4.7(a)). An alternative description for the Si coordination might be a very distorted trigonal bipyramidal coordination arranged by four nearest Ni neighbors at d(Si-Ni) = 2.290-2.357 Å and a fifth one at considerably larger distance (d(Si-Ni) = 3.887 (2)) Å (Figure 4.7(b)). Ta atoms are surrounded by five silicon neighbors in slightly distorted square pyramidal arrangement: d(Ta-Si) = 2.624(2), 2.637(1) (2x) and 2.664(1) (2x)Å. The interatomic distances d(Ta-Si) are comparable with those found in $TaSi_2$

($d_{average}$ = 2.703 Å)[113]. For further structural details see the Tables 4.5 and 4.6 in which the selected interatomic distances and angles for TaNiSi are presented together with their estimated standard deviations

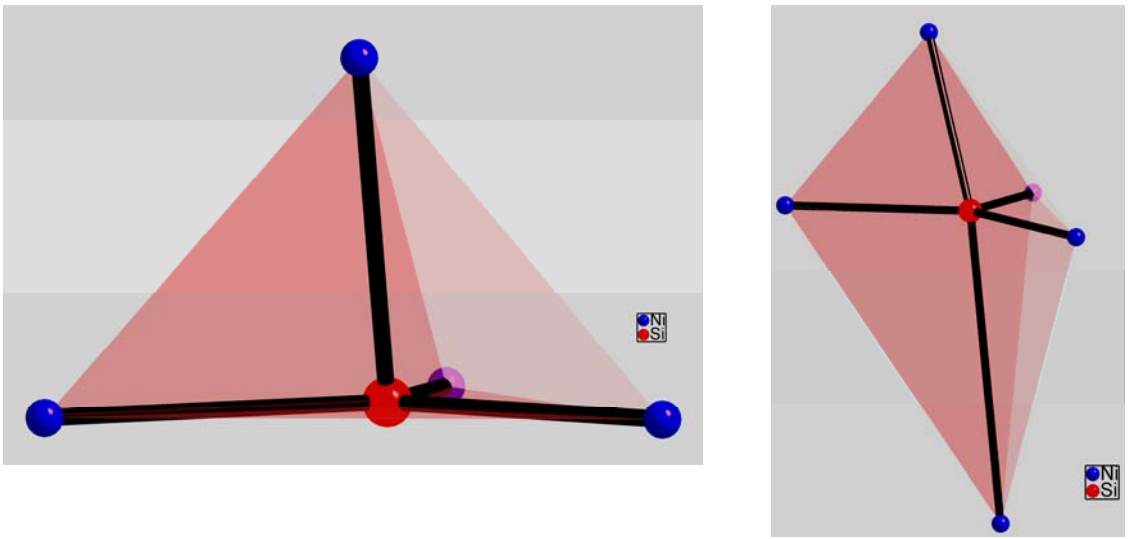

(a) **(b)**

Figure 4.7 (a) Strongly distorted $SiNi_4$ tetrahedron. Si atom has moved out of center to occupy one of the trigonal faces. (b) Alternative description of Si environment as an irregular trigonal bipyramidal.

Table 4.5 Selected interatomic distances for TaNiSi.

Atoms		Distances [Å]
Ta-	Si	2.6240 (20)
	Si	2.6372 (13)
	Si	2.6637 (14)
	Ni	2.7844 (7)
	Ni	2.8370 (9)
	Ni	2.8427 (6)
	Ni	2.8931 (10)
	Ta	3.1008 (4)
Ni-	Si	2.2897 (15) 2x
	Si	2.3419 (19)
	Si	2.3567 (24)
	Si	3.8870 (17)
	Ni	2.8216 (12)
	Ta	2.7844 (7)
	Ta	2.8370 (9)
	Ta	2.8427 (6)
	Ta	2.8931 (10)
Si-	Ni	2.2897 (15) 2x
	Ni	2.3419 (19)
	Ni	2.3567 (24)
	Ni	3.8870 (17)
	Ta	2.6240 (20)
	Ta	2.6372 (13)
	Ta	2.6637 (14)

Table 4.6 Selected bond angles in the crystal structure of TaNiSi

Atoms	Bond Angle [°]	Atoms	Bond Angle [°]
Si – Ni – Si	101.04 (6)	Ni - Si - Ni	117.49 (9)
	118.56 (4)		75.06 (6)
	104.94 (6)		126.57 (5)
	106.82 (10)		106.82 (10)

4.5 Thermal Analyses

DTA and DTA/TG measurement were performed with NETZSCH DTA 404 and NETZSCH STA 409 C/CD instruments, respectively. To investigate the air stability of TaNiSi, the DTA/TG experiment was performed with an Al_2O_3 crucible under static air. The DTA analysis implemented with Y_2O_3 crucible in an Ar filled glove box in order to prevent any air and moisture effect.

The simultaneous DTA/TG analysis revealed that the TG curve of TaNiSi shows the step for overall weight gain of 23.54% starts at around 800 °C (Figure 4.8). After DTA/TG investigation, X-ray powder diffraction analysis was performed on the heated sample and identified as Ta_2NiO_6, NiO and amorphous SiO_2 (Figure 4.9). The DTA analysis in air shows two sharp exothermic peaks with maximum temperatures at 885.5°C and 1529.1°C. These thermal effects are associated with the oxidation of the sample.

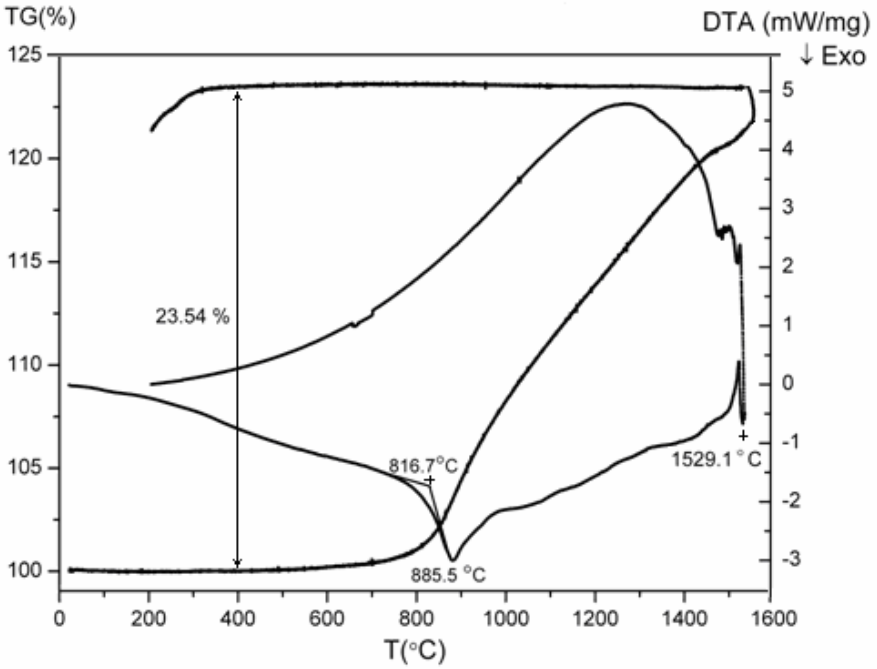

Figure 4.8 DTA/TG curve of TaNiSi.

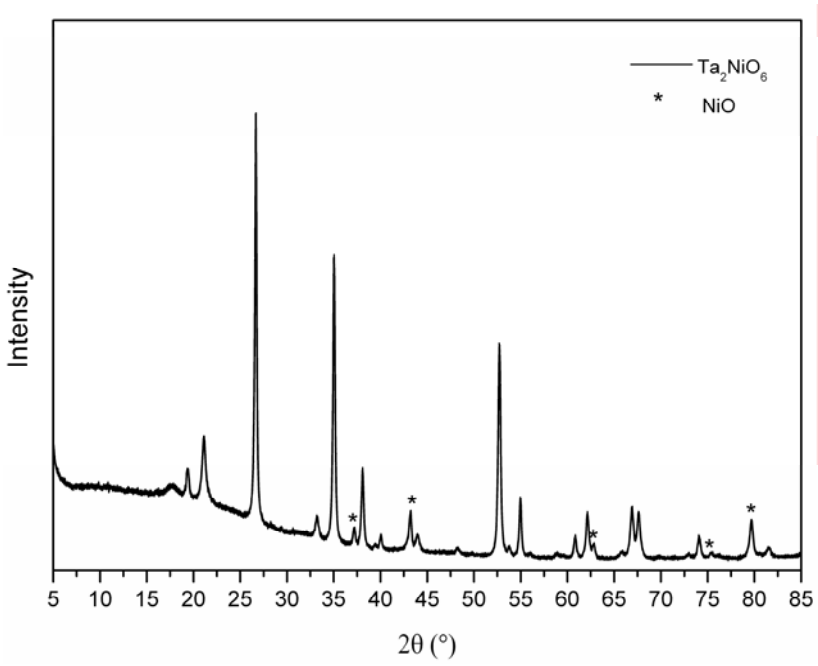

Figure 4.9 X-ray powder diagram of TaNiSi after oxidation in air.

High temperature DTA analysis under Argon revealed that TaNiSi is stable up until 1852.2 °C which is shown as an endothermic peak (Figure 4.10). Upon cooling three prominent peaks were observed at 1729 °C, 1722.8 °C and 1420.2 °C which can be presumed as crystallization of phases from the melt.

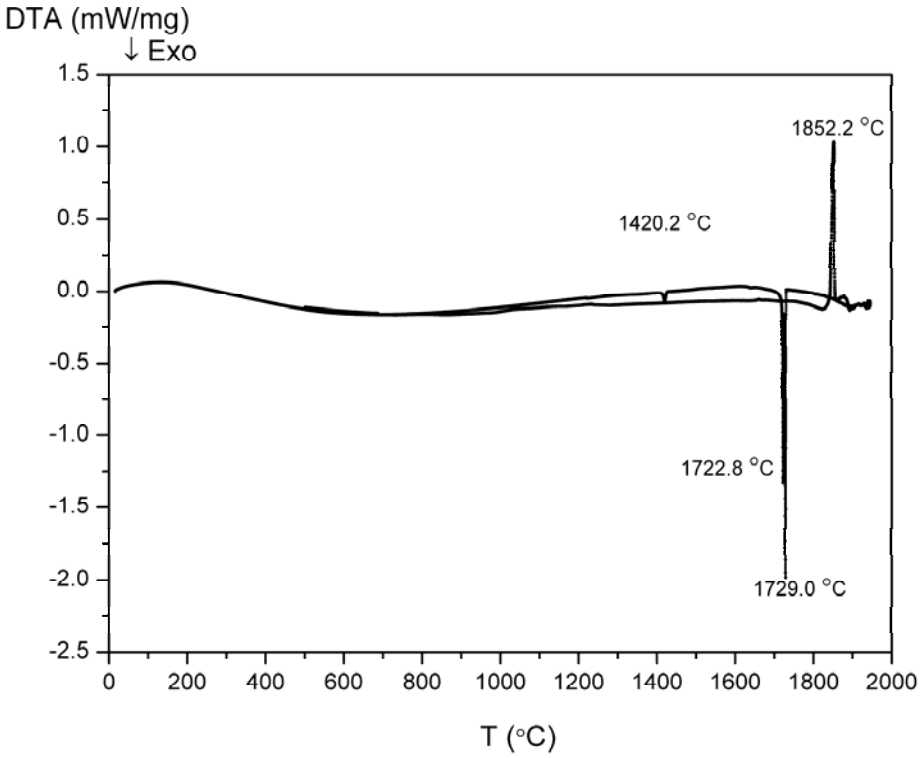

Figure 4.10 Differential thermal analysis result of TaNiSi.

4.6 Theoretical Calculations

The theoretical calculations were performed in collaboration with *Dr. Stefano Leoni* at MPI-CPfS Dresden. The electronic structure was obtained with a full-potential local orbital calculation scheme (FPLO). Total and partial densities of states are shown in Figure 4.11.

The Fermi level is located at zero energy. Whereas the valence band states originate mainly from Ta 5d and Ni 3d states, the conduction band is dominated by Ta 5d states. In this schema, the structure of TaNiSi can be interpreted as covalent, negative charged NiSi- framework with Ta cations sitting in the voids. The DOS calculation signifies the metallic behavior of the sample.

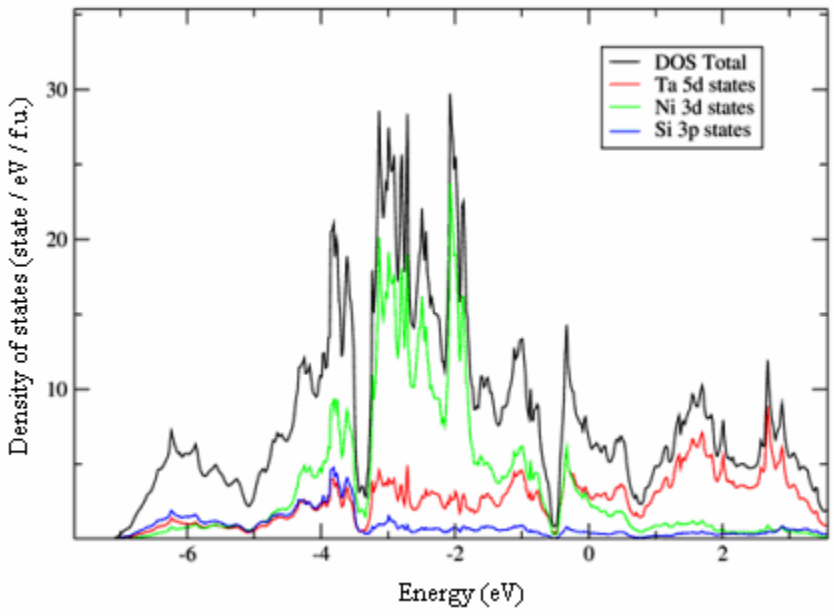

Figure 4.11 Total and partial density of states (DOS) at normal conditions**.**

Electron localization functions (ELF) analysis does not show any bond attractor between any atoms, but lone pairs at the Si anions (Figure 4.12). However, the structure of the valence shells points to the existence of a weak bond between Ni and Si. According the theoretical calculations the compound exists exactly at the border between an ionic compound and an intermetallic alloy, which is contradicting to a simple model that Ta cations are just suited in a covalent Ni-Si framework.

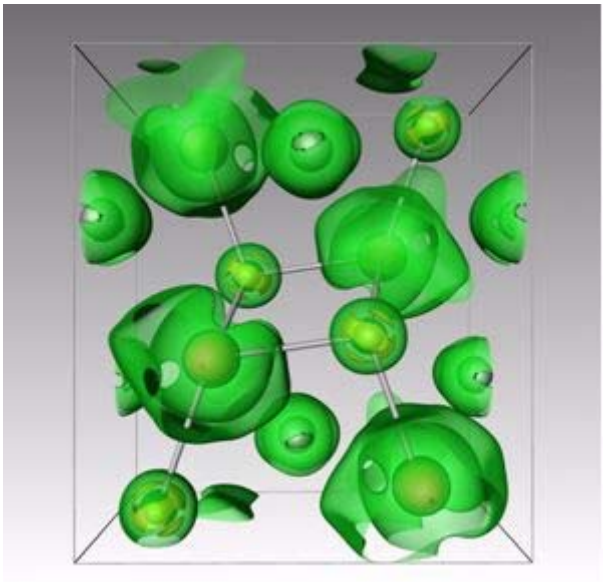

Figure 4.12 Electron localization function isosurfaces of TaNiSi.

4.7 Physical Properties

One of the main aims of the present study was to investigate the physical properties of the tantalum nickel silicide phase. In the following sections, the results of resistivity, magnetic susceptibility and specific heat measurements of this ternary compound are given.

4.7.1 Electrical Resistivity Measurements

For the resistivity measurements, the polycrystalline TaNiSi was ground with a tungsten carbide mortar and then the powder was pressed under 5 kPa/cm^2 pressure to a rectangle prism shape with well defined edges. The electrical resistivity has been measured as a function of temperature by standard four-point dc method with cryostat in an Ar filled

glove box. The contacts are made by copper-filled epoxy glue with using 50 μm in diameter Cu.

The investigation of the electrical resistivity of TaNiSi revealed that the compound behave as metallic conductor (Figure 4.13). The room temperature resistivity around 10^{-5} Ωm indicates a bad metallic conduction. The residual resistivity ratio is found to be RRR = ρ(300K) / $\rho_r \approx 4.68$ which is relatively low. This indicates that disorder scattering play a significant role in material. Additionally, high residual resistivity value of $\rho_r \approx 2.12 \times 10^{-6}$ Ωm indicates that grain boundaries effect on resistivity could be significant. Below around 13K, the resistivity becomes temperature independent.

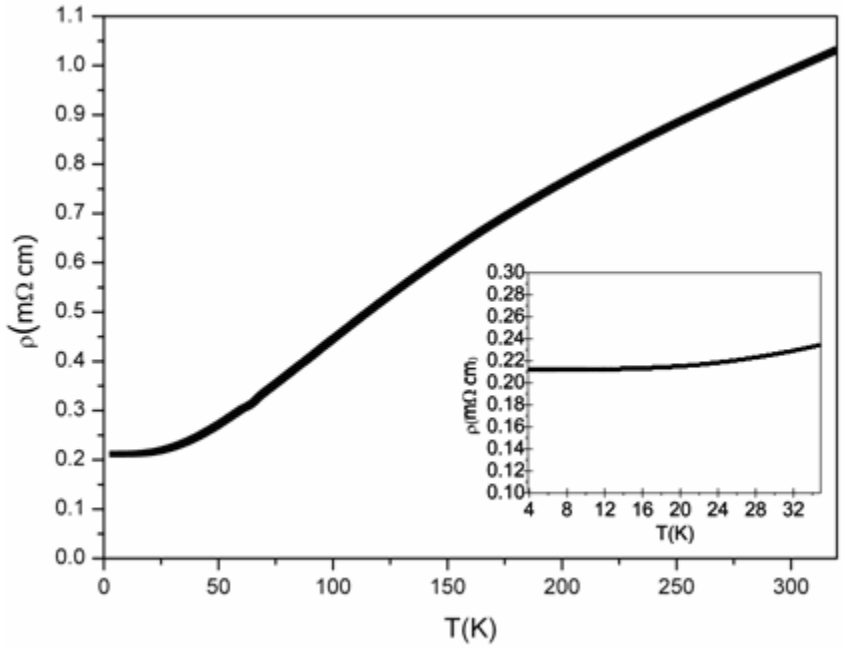

Figure 4.13 Temperature dependence of electrical resistivity ρ(T) of TaNiSi.

4.7.2 Specific Heat Capacity Measurement

The temperature dependence of the specific heat capacity of the TaNiSi is depicted in Figure 4.14.

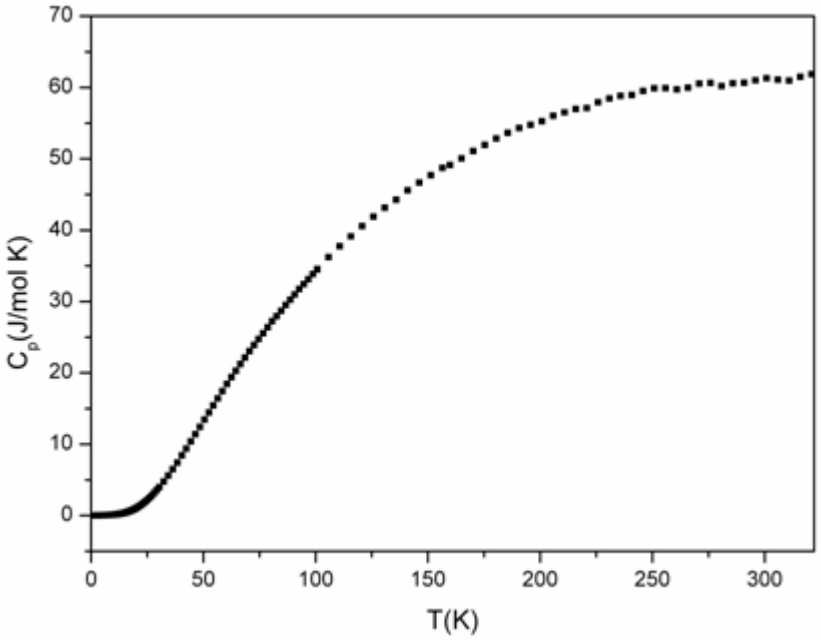

Figure 4.14 Specific heat Cp vs. temperature for TaNiSi.

As explained in section 2.4.5, for metallic-like conducting materials at low temperatures, *Cp* can be approximated by the well-known relationship,

$$Cp = \gamma T + \beta T^3 \tag{4.1}$$

where γ and β are the electronic Sommerfeld term and Debye T^3 lattice term (phononic term), respectively. A plot of Cp /T versus T^2 should yield a straight line with an intercept γ

and a slope of β. Such a plot yield a straight line as seen in Figure 4.15 with an intercept γ = 5.28(1) mj/mol K^2 and slope β = 7.14(3)*10^{-2} mj/mol K^4 in the 1.78 - 8.85 K temperature range. The measured value of Sommerfeld coefficient is in between the electronic terms in metallic elements Fe(4.98 mj/mol K^2) and Ta(5.9 mj/mol K^2)[114].

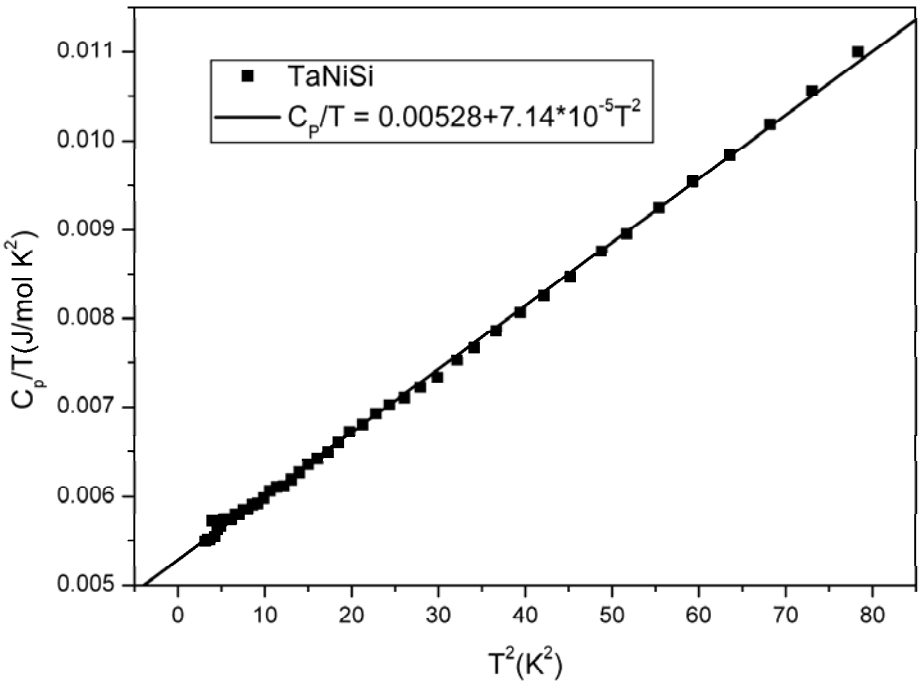

Figure 4.15 C_p / T vs. T^2 in the temperature regime 1.8 - 8.85 K.

The characteristic Debye temperature, θ_D , of a material in the limit of low temperature can be derived from its β value from the relation,

$$\theta_D=(N\frac{12}{5}\pi^4 R\beta^{-1})^{1\backslash 3} \tag{4.2}$$

where *N* and R are the number of atoms per formula unit and molar gas constant, respectively[115]. From the above equation, the characteristic Debye temperature is obtained as 433.88(1) K. The Debye temperature can be used as a measure of the stiffness of a solid [116]. The calculated value is considerably higher than for elemental Ta (240 K) and comparable with that of Fe(420 K)[117].

4.7.3 Magnetic Susceptibility Measurements

The magnetic susceptibility χ versus temperature plot of TaNiSi in different external magnetic fields is displayed in Figure 4.16. It can be deduced that there are some ferromagnetic impurities ordering at $T < 60$ K. It might be speculated that the ferromagnetism could be due to elemental nickel present at ppm level in the sample. Nearly temperature - independent magnetic susceptibility was observed above 60 K which is known as Pauli paramagnetism observed for metals.

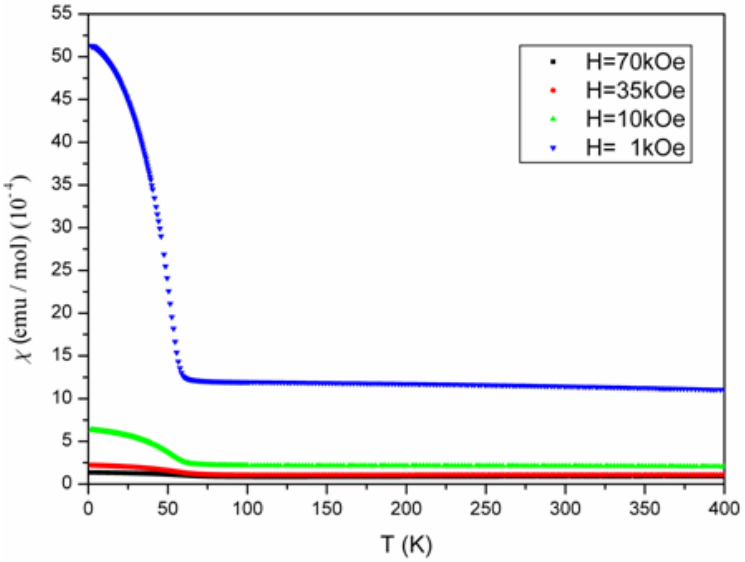

Figure 4.16 Magnetic susceptibilities χ(T) at different external magnetic fields for TaNiSi.

4.8 Coatings of Wires

Ta wires with 0.8 mm in diameter were coated with NiSi. For the coating process, binary NiSi was synthesized via arc melting. The product was then transferred into a carbon crucible and melted in the high frequency furnace (HF) (Figure 4.17(a)). Subsequently, the Ta wire was dipped in the melt and rotated with a constant speed by using a small electro motor depicted in Figure 4.17(b).

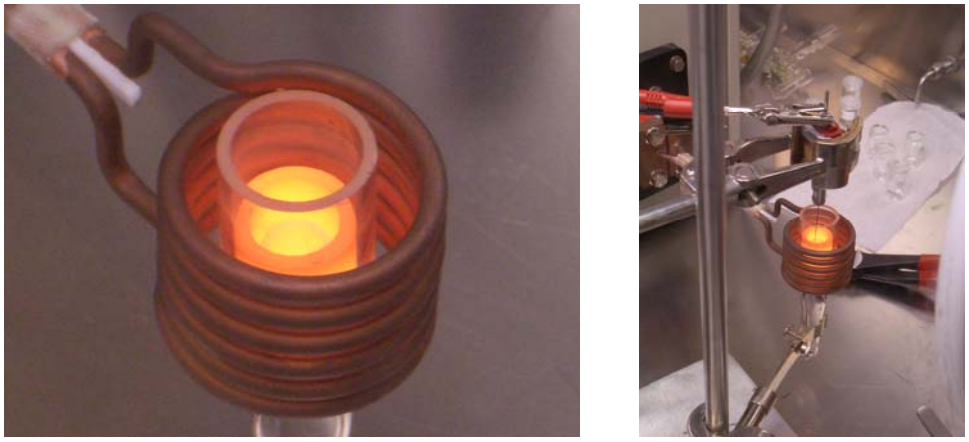

(a) **(b)**

Figure 4.17 (a) Melt NiSi in carbon crucible heated with high frequency furnace(HF). **(b)**Coating of Ta wires with melt NiSi in HF.

The rotation of the metal wire is essential to achieve a homogenous coating while the reaction time was varied between 10 seconds to 10 minutes. As soon as the wire gets in contact with molten NiSi, a reaction takes place in which the tantalum wire is dissolved and coated simultaneously (Figure 4.18).

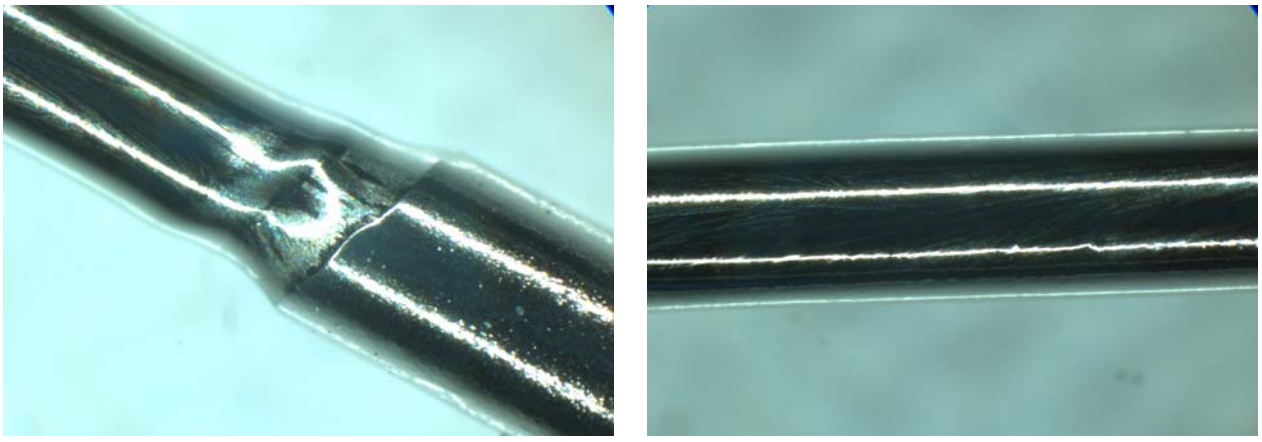

(a) **(b)**

Figure 4.18 Optical microscope images of Ta wire after 2 minute constant stirring **(a):** Upper left is coated wire and lower right is Ta wire, **(b):** The coated part.

EDXS analysis performed on a polished wire coated for 2 minutes reveals the presence of a homogenous single crystalline coated layer (Figures 4.19-4.20). The width of coating is ranging between 3.5 and 4.27µm. The coating of other wires like tungsten (W) was also successful for which the above described method was applied.

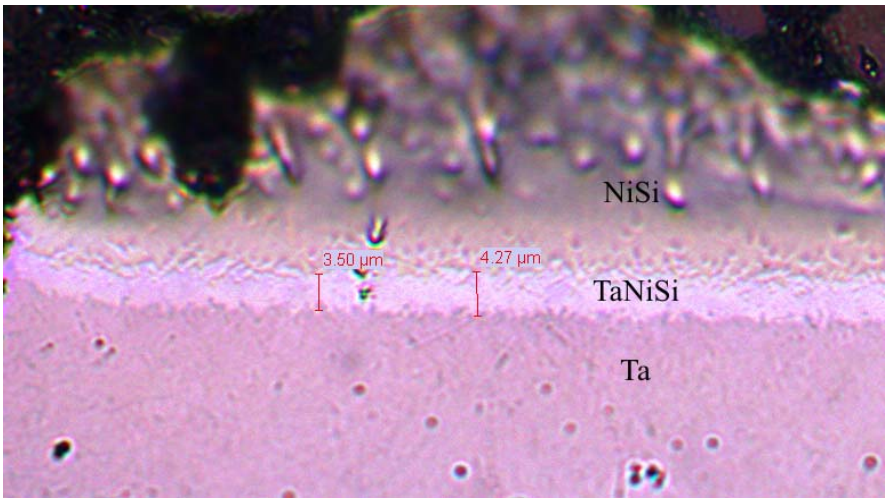

Figure 4.19 Bright-field optical microscope image of coated Ta wire.

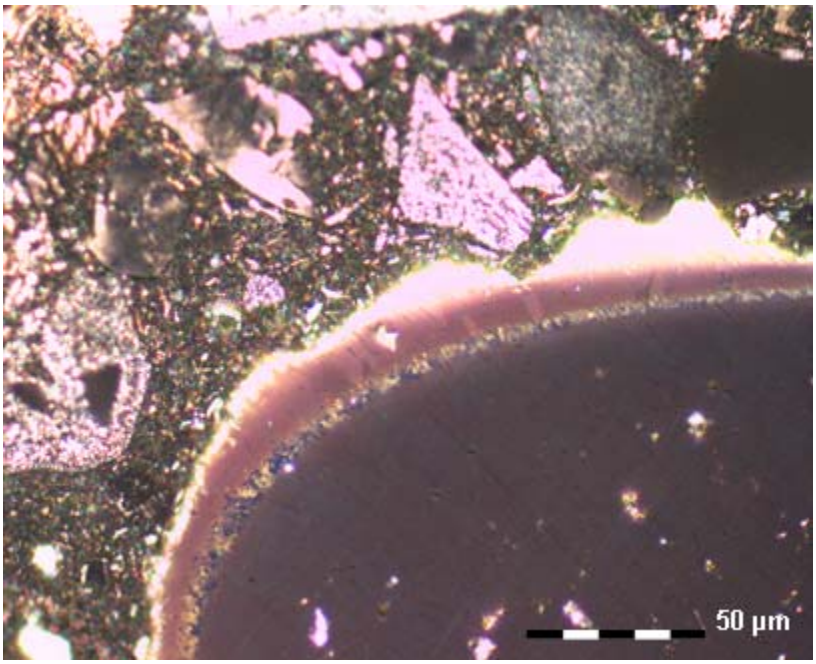

Figure 4.20 Polarized light optical microscope image of coated Ta wire.

As afore mentioned, the DTA and DTA/TG analyses show that the melting of TaNiSi does not occur until 1852 °C and it is stable in ambient conditions up until 800 °C. On the other hand metals like Ta are known to be oxidized already at moderate temperatures, when heated in air. In this sense the coating may prevent the surface oxidation of the Ta metal at higher temperatures. Since TaNiSi behaves as metallic conductor, its electrical conduction will not be affected any way. These findings suggest that the new method is quite suitable for high temperature materials application.

4.9 Conclusions and Outlook

Single phase TaNiSi was obtained via a new low temperature synthesis route. The chemical composition and the phase purity were confirmed by WDXS analysis. The crystal structure of the sample was determined by single crystal X-ray diffraction method. The compound crystallizes in the orthorhombic TiNiSi-type structure with the space group *Pnma* (No.62). The density of states calculation indicates a metallic behavior in accordance with the result of electronic transport property investigations revealing that TiNiSi sample behaves as a bad metallic conductor. A Debye temperature of 433.88 K was measured indicating that the stiffness of the material is higher than that of Ta and even Fe. Magnetic susceptibility results prove that TaNiSi is a Pauli paramagnet. A new method of single-crystalline coating on metal wires was developed and successfully employed on Ta which may be used in a high temperature materials application in future. At present, the related research activities are focused on investigation and understanding of the physical changes on the surface of Ta wire, as well as the chemical reactions taking place between Ta and NiSi melt during the coating process.

BIBLIOGRAPHY

[1] H. Davy, *Philos. Trans. R. Soc. London*, 1811. **101**: p. 155.

[2] M. Faraday, *Q. J. Sci.*, 1823. **15**: p. 71.

[3] M. von Stackelberg, O. Gotzen, J. Pietuchovsky, O. Witscher, H. Fruhbuss, and W. Meinhold, *Fortschr. Mineral.*, 1947. **26**: p. 122.

[4] C. Cros, M. Pouchard, and P. Hagenmuller, *Compt. Rend.*, 1965. **260**: p. 4764.

[5] J. S. Kasper, P. Hagenmuller, M. Pouchard, and C. Cros, *Science*, 1965. **150**: p. 1713.

[6] S. Bobev and S. C. Sevov, *Journal of Solid State Chemistry*, 2000. **153**: p. 92-105.

[7] J. Gallmeier, H. Schakfer, and A. Weiss, *Z. Naturforsch.*, 1969. **24b**: p. 665.

[8] I. Zerec, *Ph. D. Thesis*, in The Faculty of Mathematics and Natural Sciences. 2004, Technical University of Dresden: Dresden.

[9] W. Carrillo-Cabrera, J. Curda, H. G. von Schnering, S. Paschen, and Yu. Grin, *Zeitschrift für Kristallographie - New Crystal Structures*, 2000. **215**(4): p. 207-208.

[10] S. Kim, S. Hu, C. Uher, T. Hogan, B. Huang, J. D. Corbett, and M. G. Kanatzidis, *Journal of Solid State Chemistry*, 2000. **153**(2): p. 321-329.

[11] H. Fukuoka, K. Iwai, S. Yamanaka, H. Abe, K. Yoza and L. Haming, *Journal of Solid State Chemistry*, 2000. **151**: p. 117-121.

[12] H. Fukuoka, K. Ueno, and S. Yamanaka, *Journal of Organometallic Chemistry*, 2000. **611**: p. 543-546.

[13] A. Bentien, A. E. C. Palmqvist, J. D. Bryan, S. Latturner, G. D. Stucky, L. Furenlid, and B. B. Iversen, *Angewandte Chemie International Edition*, 2000. **39**(20): p. 3613-3616.

[14] B. C. Chakoumakos, B. C. Sales, D. G. Mandrus, and G. S. Nolas, *Journal of Alloys and Compounds*, 2000. **296**: p. 80-86.

[15] B. Eisenmann , H. Schäfer, and R. Zagler, *Journal of the Less Common Metals*, 1986. **118**(1): p. 43-55.

]16] G. S. Nolas, J. L. Cohn, G. A. Slack, and S. B. Schujman, *Applied Physics Letters*, 1998. **73**(2): p. 178-180.

[17] V. L. Kuznetsov, L. A. Kuznetsova, A. E. Kaliazin, and D. M. Rowe, *Journal of Applied Physics*, 2000. **87**(11): p. 7871-7875.

[18] G. S. Nolas, T. J. R. Weakley, J. L. Cohn, and R. Sharma, *Physical Review B*, 2000. **61**(6): p. 3845-3852.

[19] J. L. Cohn, G. S. Nolas, V. Fessatidis, T. H. Metcalf, and G. A. Slack, *Physical Review Letters*, 1999. **73**(4): p. 779-782.

[20] S. Paschen, W. Carrillo-Cabrera, A. Bentien, V. H. Tran, M. Baenitz, Yu. Grin, and F. Steglich, *Physical Review B*, 2001. **64**: p. 214404.

[21] Y. Mudryk, P. Rogl, C. Paul, S. Berger, E. Bauer, G. Hilscher, C. Godart, and H. Noël, *Journal of Physics: Condensed Matter*, 2002. **14**: p. 7991.

[22] J. D. Bryan, N. P. Blake, H. Metiu, G. D. Stucky, B. B. Iversen, D. R. Poulsen, and A. Bentien, *Journal of Applied Physics*, 2002. **92**(12): p. 7281.

[23] S. Latturner, X. Bu, N. Blake, H. Metiu, and G. Stucky, *Journal of Solid State Chemistry*, 2000. **151**: p. 61-64.

[24] H. Anno, M. Hokazono, M. Kawamura, J. Nagao, and K. Matsubara, *in Proc. of 21th Int. Conference on Thermoelectrics*, ed. IEEE. 2002: New York. p. 77-80.

[25] W. Carrillo-Cabrera, R. Cardoso Gil, V. H. Tran, and Yu. Grin, *Zeitschrift für Kristallographie - New Crystal Structures*, 2002. **217**: p. 181-182.

[26] A. Bentien, B. B. Iversen, J. D. Bryan, G. D. Stucky, A. E. J. Palmqvist, A.J. Schultz, and R. W. Henning, *Journal of Applied Physics*, 2002. **91**(9): p. 5694-5699.

[27] D. Nataraj, J. Nagao, M. Ferhat, and T. Ebinuma, *Journal of Applied Physics*, 2003. **93**(5): p. 2424-2428.

[28] A. Czybulka, B. Kuhl, H. Schuster, *Zeitschrift für Anorganische und Allgemeine Chemie*, 1991. **594**(1): p. 23-28.

[29] D. Huo, T. Sasakawa, Y. Muro, and T. Takabatake, *Applied Physics Letters*, 2003. **82**(16): p. 2640-2642.

[30] B. Kuhl, A. Czybulka, and H. Schuster, *Zeitschrift für Anorganische und Allgemeine Chemie*, 1995. **621**(1): p. 1-6.

[31] G. Cordier and P. Woll, *Journal of the Less Common Metals*, 1991. **169**(2): p. 291-302.

[32] F. W. Herrmann, K. Tanigaki, T. Kawaguchi, S. Kuroshima, and O. Zhou, *Physical Review B*, 1999. **60**(19): p. 13245-13248.

[33] S. Yamanaka, E. Enishi, H. Fukuoka, and M. Yasukawa, *Inorganic Chemistry*, 2000. **39**: p. 56-58.

[34] W. Carrillo-Cabrera, S. Budnyk, Y. Prots, and Yu. Grin, *Zeitschrift für Anorganische und Allgemeine Chemie*, 2004. **630**(13-14): p. 2267-2276.

[35] T. Kawaguchi, K. Tanigaki, and M. Yasukawa, *Applied Physics Letters*, 2000. **77**(21): p. 3438-3440.

[36] R. Kröner, K. Peters, H. G. von Schnering, and R. Nesper, *Zeitschrift für Kristallographie - New Crystal Structures*, 1998. **213**(4): p. 664.

[37] Y. Mudryk, P. Rogl, C. Paul, S. Berger, E. Bauer, G. Hilscher, C. Godart, H. Noel, A. Saccone, and R. Ferro, *Physica B*, 2003. **328**: p. 44–48.

[38] Y. Li, J. Chi, W. Gou, S. Khandekar, and Jr J. R. Ross, *Journal of Physics: Condensed Matter*, 2003. **15**: p. 5535–5542.

[39] Y. Li and Jr J. H. Ross, *in: Proceedings of the March Meeting 2005*. 2005. Los Angeles, USA.

[40] Y. Li and Jr J. H. Ross, *Proc. Mater. Res. Soc.*, 2004. **793**: p. S7.3.

[41] R. F. W. Herrmann, K. Tanigaki, S. Kuroshima, H. Suematsu, *Chemical Physics Letters*, 1998. **283**(1-2): p. 29-32.

[42] H. G.von Schnering, *Nova Acta Leopoldina*, 1985. **59**: p. 168.

[43] J. T. Zhao and J.D. Corbett, *Inorganic Chemistry*, 1994. **33**(25): p. 5721-5726.

[44] G. S. Nolas, B. C. Chakoumakos, B. Mahieu, G. J. Long, and T. J. R. Weakley, *Chemistry of Materials*, 2000. **12**(7): p. 1947-1953.

[45] G. S. Nolas, J. M. Ward, J. Gryko, L. Qiu, and M. A. White, *Physical Review B*, 2001. **64**: p. 153201.

[46] A. Bentien, M. Christensen, J. D. Bryan, A. Sanchez, S. Paschen, F. Steglich, G. D. Stucky, and B. B. Iversen, *Physical Review B*, 2004. **69**: p. 045107.

[47] N. Kamakura, T. Nakano, Y. Ikemoto, M. Usuda, H. Fukuoka, S. Yamanaka, S. Shin, and K. Kobayashi, *Physical Review B*, 2005. **72**: p. 14511.

[48] C.L. Condron, R. Porter, T. Guo, and S.M. Kauzlarich, *Inorganic Chemistry*, 2005. **44**: p. 9185-9191.

[49] L. Yang, Y. Wang, T. Liu, T. D. Hu, B. X. Li, K. Stahl, S. Y. Chen, M. Y. Li, P. Shen,G. L. Lu, Y. W. Wang, and J. Z. Jiang, *Journal of Solid State Chemistry*, 2005. **178**: p. 1773–1777.

[50] D. Connetable and X. Blase, *Applied Surface Science*, 2004. **226**: p. 289-297.

[51] H. Kawaji, H. Horie, S. Yamanaka, and M. Ishikawa, *Physical Review Letters*, 1995. **74**: p. 1427.

[52] H. Fukuoka, J. Kiyoto, and S. Yamanaka, *Inorganic Chemistry*, 2003. **42**: p. 2933-2937.

[53] H. Fukuoka, J. Kiyoto, and S. Yamanaka, *Journal of Physics and Chemistry of Solids*, 2004. **65**: p. 333-336.

[54] I. M. Gat, Y. Fudamoto, A. Kinkhabwala, M. I. Larkin, G. M. Luke, J. Merrin, B. Nachumi, Y. J. Uemura, K. M. Kojima, E. Eiji, and S. Yamanaka, *Physica B*, 2000. **289-290**: p. 285-388.

[55] K. Moriguchi, M. Yonemura, A. Shintani, and S. Yamanaka, *Physical Review B*, 2000. **61**(15): p. 9859-9862.

[56] G. Slack, *CRC Handbook of Thermoelectrics*. CRC, Boca Raton, ed. Rowe, D. M. 1995, FL. 407-440.

[57] T. M. Tritt, G. S. Nolas, G. D. Mahan, D. Mandrus, and M. G. Kanatzidis, *Thermoelectric materials 2000 : the next generation materials for small-scale refrigeration and power generation applications*. Vol. 626. 2000, San Francisco, California, U.S.A: Materials Research Society.

[58] G. Chen, M. S. Dresselhaus, G. Dresselhaus, J.-P. Fleurial, and T. Caillat, *International Materials Reviews*, 2003. **48**(1): p. 45-66.

[59] T. Matsui, J. Furukawa, K. Tsukamoto, H. Tsuda, and K. Morii, *Journal of Alloys and Compounds*, 2005. **391**: p. 284–287.

[60] J. F. Meng, S. N. V. Chandra, J. V. Badding, and G. S. Nolas, *Journal of Applied Physics*, 2001. **89**(3): p. 1730-1733.

[61] B. C. Sales, B. C. Chakoumakos , R. Jin , J. R. Thompson, and D. Mandrus, *Physical Review B*, 2001. **63**(24): p. 245113.

[62] G. B. Adams, M. O'Keeffe, A. A. Demkov, O. Sankey, and Y.-M. Huang, *Physical Review B*, 1994. **49**: p. 8048-8053.

[63] J. Zhao, A. Buldum, J. P. Lu, and C. Y. Fong, *Physical Review B*, 1999. **60**: p. 14177–14181.

[64] A. San-Miguel, P. Mélinon, D. Connétable, X. Blase, F. Tournus, E. Reny, S. Yamanaka, and J. P. Itié, *Physical Review B*, 2002. **65**: p. 054109.

[65] W. Jeitschko, A. G. Jordan, and P. A. Beck, *Transactions of the Metallurgical Society of Aime*, 1969. **245**: p. 335-339.

[66] W. Jeitschko, Acta Cryst., 1968. **B24**: p. 930-934.

[67] *Periodic Table of Elements*. 2002, WILEY - VCH Verlag GmbH.

[68] *Inorganics*. 2006, Chempur Feinchemikalien und Forschungsbedarf GmbH available at: http://www.chempur.de/.

[69] *MBRAUN Technical Guide*. 2005, MBRAUN available at: http://www.mbraun.de/technical-guide.htm.

[70] *Induction Heating*. 2005, Hüttinger Electronic available at: http://www.huettinger-electronics.com/.

[71] *Arc Melting*. 2003, Centorr Vacuum Industries available at: http://www.centorr.com/lab/arcmelt.html.

[72] Jr W. D. Callister, *Materials Science and Engineering : An Introduction*. 2003, New York: Wiley.

[73] W. Clegg, *Crystal Structure Determination*. 1998, Oxford: New York : Oxford University Press.

[74] R. A. Young and D. B. Wiles, *Journal of Applied Crystallography*, 1982. **15**: p. 430.

[75] K. D. M. Harris, M. Tremayne, and B. M. Kariuki, *Angewandte Chemie International Edition*, 2001. **40**: p. 1626-1651.

[76] *Inorganic Crystal Structure Database (ICSD)*. 2005, FIZ Karlsruhe: Germany.

[77] *Stoe WINXPOW 1.2*. 2000, Stoe & Cie GmbH: Darmstadt.

[78] P. Luger, *Modern X-ray Analysis on Single Crystals*. 1980, Berlin: New York : W. de Gruyter.

[79] L. J. Farrugia, *Journal of Applied Crystallography*, 1999. **32**: p. 837-838.

[80] R. V. Grieken, *Handbook of X-Ray Spectrometry: Second Edition, Revised and Expanded*. 2001, New York, NY, USA: Marcel Dekker Incorporated.

[81] L. L. R. Taylor, R. B. Papp, and B. D. Pollard, *Instrumental Methods for Determining Elements*. 1994: New York : VCH.

[82] L. Litynska, J. Wojewoda, P. Zieba, M. Faryna, W. Gust, and E. J. Mittemeijer, *Microchimica Acta*, 2004. **145**: p. 107-110.

[83] E. Lifshin, *X-ray Characterization of Materials*. 1999, Weinheim: Wiley-Vch.

[84] D. A. Skoog, *Principles of Instrumental Analysis*. 1992, Fort Worth: Saunders College Pub.

[85] S.-D. Clas, C. R. Dalton and B. C. Hancock, *Pharmaceutical Science & Technology Today*, 1999. **2**(8): p. 311-320.

[86] T. Hatakeyama and F.X. Quinn, *Thermal Analysis : Fundamentals and Applications to Polymer Science*. 1994, Chichester, England: New York : Wiley.

[87] *Thermal Analysis Products and Solutions*. 2005, NETZSCH-Gerätebau GmbH available at: http://www.netzsch-thermal-analysis.com/en/products/.

[88] D. R. Askeland and P. P. Phulé, *The Science and Engineering of Materials*. 2003, Pacific Grove, CA: Brooks/Cole-Thomson Learning.

[89] J. I. Gersten and F. W. Smith, *The Physics and Chemistry of Materials*. 2001, New York: Wiley.

[90] C. Kittel, *Introduction to Solid State Physics*. 1986, New York: Wiley.

[91] T. Tsutaokaa, Y. Nakamori, K. Koyama, and T. Tokunaga, *Journal of Magnetism and Magnetic Materials*, 2005. **293**: p. 768-773.

[92] D. Jiles, *Introduction to the Electronic Properties of Materials*. 1994, London: New York : Chapman and Hall.

[93] K. M. Drulis, A. Czopnik, H. Drulisa, and M. W. Barsoum, *Journal of Applied Physics*, 2003. **95**(1): p. 128-133.

[94] R. Turton, *The Physics of Solids*. 2000, Oxford: New York : Oxford University Press.

[95] H. P. Myers, *Introductory Solid State Physics*. 1997, London: Taylor and Francis.

[96] J. R. Hook, H. E. Hall, *Solid State Physics*. 1998, Chichester: New York : Wiley.

[97] N. A. Spaldin, *Magnetic Materials : Fundamentals and Device Applications*. 2003, Cambridge, U.K.: New York : Cambridge University Press.

[98] R. Morjan and S. Prasalovich, *Magnetic Hysterisis*. 2003, Chalmer University of Technology Göteborg University, available at: www.fy.chalmers.se/edu/lab/ labpm/em4_magnetic_hysteresis.pdf

[99] J. P. Jakubovics, *Magnetism and Magnetic Materials*. 1994, London ; Brookfield, VT, USA: Institute of Metals.

[100] M. McElfresh, *Fundamentals of Magnetism and Magnetic Measurements*. 1994, Purdue University, QUANTUM DESIGN, available at http://www.qdusa.com/resources/tdrequestsmain.html.

[101] B. C. Sales, B. C. Chakoumakos, and D. Mandrus, *Journal of Solid State Chemistry*, 1999. **146**: p. 528-532.

[102] H. Pfisterer, and K. Schubert, *Naturwissenschaften*, 1950. **37**: p. 112-113.

[103] K. Koepernik and H. Eschrig, *Physical Review B*, 1999. **59**(3): p. 1743-1757.

[104] O. K. Andersen, *Physical Review B*, 1975. **12**(8): p. 3060-3083.

[105] O. K. Andersen and O. Jepsen, *Explicit*, Physical Review Lettrers, 1984. **53**(27): p. 2571-2574.

[106] O. K. Andersen, *The Stuttgart TB-LMTO-ASA program Version 4.7*. 2000, Max-Planck-Institut fur Festkorperforschung Germany: Stuttgart.

[107] A. D. Becke and K. E. Edgecombe, *Journal of Chemical Physics*, 1990. **92**(9): p. 5397.

[108] A. Savin, O. Jepsen, J. Flad, O. K. Andersen, H. Preuss, and H. G. von Schnering, *Angewandte Chemie International Edition*, 1992. **31**: p. 187.

[109] Yu. Grin, M. Kohout, at al., *Electron Localization Function*. 2002, available at: http://www.cpfs.mpg.de/ELF.

[110] J. L. Cohn, G. S. Nolas, V. Fessatidis, T. H. Metcalf, and G. A. Slack, *Physical Review Letters*, 1999. **82**(4): p. 779-782.

[111] T. B. Massalski, *Binary Alloy Phase Diagrams Second Edition*. 1990, Materials Park, Ohio: ASM International.

[112] M. K. Rabadanov and M. B. Ataev, *Kristallografiya*, 2002. **47**(1): p. 33-45.

[113] H. Nowotny and E. Laube, *Zeitschrift fuer Metallkunde*, 1941. **33**: p. 378-381.

[114] D. D. Pollock, *Physical Properties of Materials for Engineers*. 1993, Florida: Boca Raton : CRC Press.

[115] J. C. Ho, H. H. Hamdeh, M. W. Barsoum, and T. El-Raghy, *Journal of Applied Physics*, 1999. **86**(7): p. 3609-3611.

[116] T. Tohei, A. Kuwabara, F. Oba, and I. Tanaka, *Physical Review B*, 2006. **73**: p. 064304.

[117] N. W. Ashcroft, N. D. Mermin, *Solid State Physics*. First Edition. 1976, New York: Brooks Cole.

VITA

Umut Aydemir was born in Erzincan, Turkey, in 1981. He received his B.S. degrees in Chemistry and Physics from Koç University, İstanbul, in 2004. The same year, he started his study in the Department of Materials Science and Engineering as a M.S. candidate. He will be pursuing his Ph.D. research at Max Planck Institute for Chemical Physics of Solids in Dresden, Germany. His research interests are electron density theory and applications and also investigations on chemical and physical properties of intermetallic compounds with E14 elements.